Stochastic Forward and Inverse Groundwater Flow and Solute Transport Modeling

Promotor: Prof. Dr. Ir. Sjoerd E.A.T.M. van der Zee
Hoogleraar Ecohydrologie, Wageningen Universiteit

Copromotor: Dr. Ir. Johan R. Valstar
Geohydroloog, Deltares/TNO

Samenstelling Promotiecommissie:

- Prof. Dr. Ir. T.N. Olsthoorn, Technische Universiteit Delft / Waternet
- Prof. Dr. Ir. R. Uijlenhoet, Wageningen Universiteit
- PD Dr.-Ing. O.A. Cirpka, Universität Tübingen (DE)
- Dr. Ir. H.J.W.M. Hendricks-Franssen, ETH Zürich (CH)

Dit onderzoek werd uitgevoerd binnen de onderzoeksschool SENSE (Socio-Economic and Natural Sciences of the Environment).

Stochastic Forward and Inverse Groundwater Flow and Solute Transport Modeling

Gijs M.C.M. Janssen

Proefschrift
ter verkrijging van de graad van doctor
op gezag van de rector magnificus
van Wageningen Universiteit
Prof. Dr. M.J. Kropff
in het openbaar te verdedigen
op woensdag 19 november 2008
des namiddags te half twee in de Aula

Janssen, G.M.C.M. 2008. Stochastic Forward and Inverse Groundwater Flow and Solute Transport Modeling

Ph.D. Thesis Wageningen University, Wageningen, the Netherlands – with references – with summaries in English and Dutch

ISBN: 978-90-8585-241-4

Abstract

Janssen, G. M. C. M. 2008. **Stochastic Forward and Inverse Groundwater Flow and Solute Transport Modeling.** Doctoral Thesis, Wageningen University, Wageningen, The Netherlands. 194 pages.

This thesis offers three new approaches that contribute to the ability of groundwater modelers to better account for heterogeneity in physically-based, fully distributed groundwater models. In both forward and inverse settings, this thesis tackles major issues with respect to handling heterogeneity and uncertainty in various situations, and thus extends the ability to correctly and/or effectively deal with heterogeneity to these particular situations.

The first method presented in the thesis uses the recently developed advective-dispersive streamtube approach in combination with a one-dimensional traveling wave solution for nonlinear bioreactive transport, to study the interplay between physical heterogeneity, local-scale dispersion and nonlinear biodegradation and gain insight in the long-term asymptotic behavior of solute fronts, in order to deduce (the validity of) upscaling equations. Using the method in synthetic small-scale numerical experiments, it is shown that asymptotic front shapes are neither Fickian nor constant, which raises questions about the current practice of upscaling bioreactive transport.

The second method presented in the thesis enhances the management of heterogeneity by extending inverse theory (specifically, the representer-based inverse method) to determinations of groundwater age/travel time. A first-order methodology is proposed to include groundwater age or tracer arrival time determinations in measurement network design. Using the method, it is shown that, in the applied synthetic numerical example, an age estimation network outperforms equally sized head measurement networks and conductivity measurement networks, even if the age estimations are highly uncertain. The study thus suggests a high potential of travel time/groundwater age data to constrain groundwater models.

Finally, the thesis extends the applicability of inverse methods to multimodal parameter distributions. Multimodal distributions arise when multiple statistical populations exist

within one parameter field, each having different means and/or variances of the parameter of concern. No inverse methods exist that can calibrate multimodal parameter distributions while preserving the geostatistical properties of the various statistical populations. The thesis proposes a method that resolves the difficulties existing inverse methods have with the multimodal distribution. The method is successfully applied to both synthetic and real-world cases.

Table of Contents

CHAPTER

1

General Introduction

1.1. Societal Context

The world's groundwater resources provide drinking water for over 2 billion people, enable the irrigation of 40% of the world's food production (numbers from *Morris et al.* [2003], provide base flow to rivers, deliver production and cooling water for industrial processes and, on top of that, sustain an enormous variety of groundwater-dependent ecosystems. It is therefore evident that these resources are crucial to the health and functioning of societies, as well as to the natural world these societies are part of, supported by, and depend on.

Few groundwater systems have escaped the consequences of the ever-expanding human influence on the natural environment. Globally, groundwater systems are pressured, the most important reasons[1] being *overexploitation*, *contamination*, and what is called here *straitjacketing*.

Overexploitation simply results in the disappearance of resources: in some areas the decline of groundwater levels is currently at a rate that is in the order of meters a year. The "production" of groundwater for irrigation, industrial processes, drinking water, etc., is not balanced by the natural recharge of the groundwater system. Declining groundwater levels can result in dramatic increases of groundwater production costs, and, if the situation is left unchanged, they can even lead to complete exhaustion of the groundwater system's productive capacity.

The second issue, groundwater *contamination*, can take many forms. It can be accidental (e.g. a calamity at a factory processing hazardous solutions that get spilled and leach to the groundwater), the result of neglect (leaking oil pipelines), it can be a more or less (politically) accepted side effect of socially and/or economically indispensable human activities (e.g. agriculture), with groundwater quality at the wrong end of the trade-off, and it can even have a completely natural cause: think about saltwater intrusion, for example, or fluoride-rich groundwater in India, or the problems with arsenic in groundwater in Bangladesh. Groundwater contamination is also known to

[1] The interested reader is referred to *Morris et al.* [2003], *Griffioen et al.* [2003], and *Younger* [2006] for more comprehensive overviews of threats to groundwater systems

involve a wide range of scales: it can take the form of a small contaminant plume as a result of a spill, but one can also speak of nationwide groundwater contamination issues, if one takes a look at the problems caused by fertilizer or pesticide applications in agriculture. It is clear that contaminated groundwater poses risks and, potentially, damage to all its dependants. Both mitigation and remediation typically are very costly.

The third cause for stress on groundwater systems, *straitjacketing*, refers to situations in which groundwater systems need to be adjusted to human needs and changes we made to the natural environment. Groundwater systems are forced into an unnatural state and need to be controlled continuously. Many examples of straitjacketing of groundwater can be found close to home in the Netherlands, where groundwater (level) control can be regarded as a vital part of polder and delta life.

For tackling the three issues mentioned above (overexploitation, contamination, and the need for groundwater control), as well as other serious threats to groundwater resources (a comprehensive overview is given by *Morris et al.* [2003]), knowledge of the groundwater system and how it responds to new influences is crucial. Only by understanding the properties and dynamics of the system, a sensible system management can be imposed that can bring the system to a desired state, prevent (further) deterioration of the system, or help mitigate risks posed by the system's current state.

Mathematical groundwater models are essential tools to formalize and administrate the existing knowledge of groundwater systems and utilize this knowledge to produce areally distributed state descriptions and predictions according to the best available information. Thus, it has almost become unthinkable not to exploit the power of mathematical modeling in groundwater management studies. It is clear that the more sound the description of processes and system properties, the more accurate the model outcome. Improving the accuracy of groundwater models can lead to tremendous cost savings in multiple ways, for example via reduced risk of unsuccessful groundwater management (resulting in, for example, damage to infrastructure and ecosystems, crop loss or yield reduction, exhaustion of resources, pumping of contaminated groundwater etc.), and reduced need to compensate for uncertainties in the model results (e.g. overdimensioning of remediation strategies, overdimensioning of protection zones, etc.).

It is therefore no surprise that methods for the improvement of groundwater models receive continuous attention in the scientific literature.

1.2. Problem Statement

In the previous Section, the importance of system knowledge for groundwater management, and the need to make this knowledge operational through models were expressed. “Knowing” or understanding the system is, however, greatly complicated by one particular natural aspect, the dealing with which has been a recognized major challenge, as well as a research frontier, for the past three decades: heterogeneity. Heterogeneity refers to the spatiotemporal variation of the groundwater system’s properties, including initial and boundary conditions. It is the cause of the fact that the groundwater system can never be “known” completely: no matter how extensive the measurement efforts, a certain degree of uncertainty will always remain, i.e. it is intrinsic. Dealing with heterogeneity therefore automatically involves dealing with uncertainty: deterministic modeling becomes stochastic modeling. Whereas this argument is focused here towards groundwater systems, in fact it holds for earth systems in general.

Heterogeneity not only complicates the physical description of the system (e.g. spatial variation of hydraulic properties), but also the description of processes. For example, heterogeneity can greatly affect the spreading of solutes through the medium, which in turn has implications for how the solutes interact with reactive components, both in the solid and the liquid phases, but also on the arrival time distributions at designated places (e.g. groundwater extraction well fields). These effects of heterogeneity have in some way to be accounted for in modeling, which is a far from trivial task.

Thus, heterogeneity poses a great challenge for geo-professionals to still satisfy the abovementioned need for accuracy in groundwater models. Methods are needed to allow modelers to accurately, fairly and efficiently account for all relevant heterogeneity. As will be explained below, this thesis contributes to fulfilling this need in several ways.

1.3. General research objective, scope and chapter coherence

Although the main chapters of the current thesis are quite diverse, they all share a common, ultimate purpose: improved flow and transport modeling in heterogeneous subsurface environments. Specifically, the current thesis' general objective is to address approaches and develop methods that improve coping with heterogeneity in physically based, fully distributed numerical groundwater models.

It is important to recognize that coping with heterogeneity consists of two distinct components:

- to account for it. The heterogeneity, and the uncertainties stemming from it, should, to the best available knowledge, be fully and fairly accounted for in the model. This means that the heterogeneity needs to be characterized and integrated correctly into the model. Failing to acknowledge important sources of uncertainty in the model can lead to false certitude, wreck model calibration, and decrease accuracy of model results. This may seem obvious, yet in this thesis, the reader will find several examples of common modeling practice in which heterogeneity is not fully recognized.
- to manage it. Once heterogeneity and uncertainty are acknowledged and fully accounted for in the model, the challenge is to minimize the increased uncertainty this caused. In other words, given heterogeneity, the modeler has to "make the best of it". There is only one way to do this: smartly collect and integrate data. This will be discussed further in the next Section.

Accounting for heterogeneity in fully distributed models affects both model parameters and model processes: the model parameters, because those exhibit the heterogeneity, and the model processes, because their descriptions might need adjustment to account for different regimes brought about by the heterogeneity. Managing heterogeneity, in the sense of minimizing uncertainties, is typically effectuated through the model parameters only, as, at the stage of a groundwater model study, there seems to be little a groundwater modeler can do to reduce the uncertainties stemming from the process descriptions.

As coping with heterogeneity affects both the formulations of processes and the parameterization of the system, improving stochastic groundwater flow and solute

transport modeling capabilities can be targeted at both forward and inverse modeling approaches. Forward modeling deals with the processes: given a system's parameters (conductivities, boundary conditions, dispersivities, reaction and distribution constants, etc.), how can the evolvement of the system's states (heads, fluxes, concentrations, temperatures, age distributions etc.) be mathematically described best? Inverse modeling, on the other hand, deals with the parameters: in an inverse model run, the system's parameters as used in the model are adjusted such that the model reproduces actual observations of the system's states. Simply put: a forward model estimates states based on parameters, whereas an inverse model estimates parameters based on states. In both forward and inverse settings, this thesis tackles major issues with respect to handling heterogeneity and uncertainty in different situations, and thus extends the ability to correctly and/or effectively deal with heterogeneity to these particular situations. This thesis offers three stochastic methods: one that is aimed at accounting for heterogeneity in process formulations (forward modeling, Chapter 2), one that increases possibilities with respect to managing uncertainty (by means of inverse modeling, Chapter 3), and one that enables a better accounting for heterogeneity in model parameters (inverse modeling, Chapter 4 and 5).
Figure 1 provides a schematic summary of the above. The next Section introduces the main chapters while explaining how they fit into the above-sketched background.

1.4. Outline of the Thesis

Chapter 2: accounting for heterogeneity in the model processes

Chapter 2 is a clear example of accounting for heterogeneity in process formulations. Here the process formulations describe nonlinear bioreactive transport in a bioremediation setting. The effect of heterogeneity of the medium's hydraulic properties on this process is that local-scale dispersion gets enhanced due to preferential transport of the contaminant plume, increasing the presence of large concentration gradients. Increased local-scale dispersion leads to increased mixing of reactants, which results in higher reaction rates. The process of local scale dispersion (and therefore its effects) cannot be directly incorporated in the advection-dispersion-reaction equations resolved

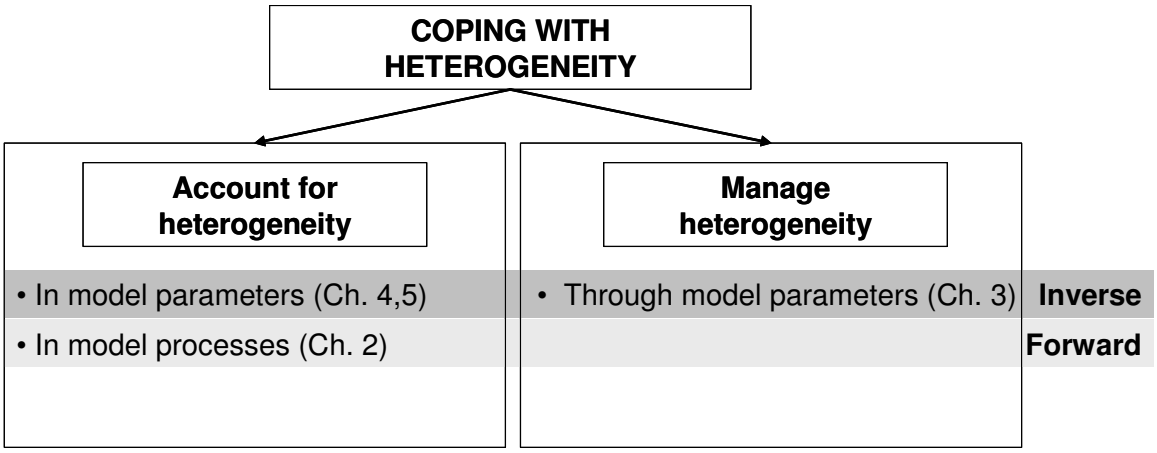

Figure 1. Scheme of the different aspects and model disciplines (forward and inverse) involved in coping with heterogeneity and uncertainty in groundwater flow and solute transport models. In the scheme it is indicated which Chapters in this thesis address what aspects and model disciplines.

on a typically-sized[2] numerical grid, as it depends on local scale concentration gradients, which are not known because concentrations are only calculated on the grid scale. Solving the advection-dispersion-reaction equation numerically while accounting for local scale dispersion would require very small grid cells, to obtain these local concentration distributions. Such grids are computationally too demanding, and therefore methods are needed to somehow upscale the influence of local scale processes to the scale of typically-sized model cells.

This calls for efforts to study the small-scale behavior of the transport process in detail, in order to establish whether and how the subscale transport processes have to be accounted for in the grid scale equations. In Chapter 2, an efficient computational method is proposed that enables this small-scale study, and the method is used to investigate long term behavior of the transport process. This long term (asymptotic) behavior provides information on the transport regime at larger scale, as a basis for establishing upscaling principles.

[2] Most groundwater remediation models operate on a grid with cell dimensions in the order of meters or tens of meters.

Chapter 3: managing heterogeneity

Chapter 3 is an example of management of heterogeneity by minimizing, through smart data collection and integration, the inevitable uncertainty in model results.

Measurement network design deals with the question where to perform what kind of data acquisition, in order to maximize the information it provides when integrated in the model. Chapter 3 presents a method that extends current capabilities of measurement network design to allow for the incorporation of an emerging class of system observations: travel time data. In Chapter 3, “optimal” refers to the information content of the network design with respect to the model predictions. In other words, observation type and location are chosen such that uncertainty reduction is focused on those parameters whose uncertainty causes most uncertainty of the model predictions.

Automated measurement network design basically requires two things:

1) that the effect of additional observations on the uncertainties in the model or model predictions can be calculated, before the observations are actually taken;
2) a search algorithm that effectively selects a winner among all candidate networks. The less candidate networks actually have to be evaluated before this winner is found, the more effective the search algorithm.

The first requirement effectively means that covariances between observations and model predictions have to be calculated. At first order (i.e.: under the presumption that integrating the new data into the model will not lead to large parameter adjustments), these covariances can be assumed valid for both the prior and the posterior model, which enables a priori calculation of the “worth” of a measurement campaign. In Chapter 3, an efficient way of calculating the required covariances is proposed, and the inverse theory that is necessary for this calculation is extended to be able to handle travel time data.

Chapter 4 and 5: accounting for heterogeneity in the model parameters

Chapter 4 extends the applicability of inverse methods to a challenging but ubiquitous type of parameter distributions: multimodal distributions. Multimodal distributions arise when within one parameter field multiple statistical populations exist, each having different means and/or variances of the parameter of concern. An example is a hydraulic

conductivity field of a sandy medium that contains clay lenses. Model cells belonging to the sandy background will (at least on average) have a higher conductivity assigned to them then the cells that belong to the clay lenses.

Multimodal distributions cannot be handled well by existing inverse algorithms, as will be explained in Chapter 4. In fact, no inverse algorithms are available that can calibrate multimodal parameter distributions, while preserving the geostatistical properties of the various statistical populations. Chapter 4 proposes a method that resolves the difficulties the multimodal distributions pose to the existing inverse algorithms, so that they can be used again. A major advantage of the method is that it allows the different statistical populations to change their positions during the calibration. This yields a more fair calibration approach, as these positions are, just like the actual parameter values within the populations, subject to uncertainty. This new capability thus benefits accounting for relevant heterogeneity in model parameters. It is clear, though, that by proposing a method for data integration, Chapter 4 also contributes to improved management of heterogeneity and uncertainty.

The method is illustrated on a synthetic case with known reference geostatistics, using the representer method as inverse algorithm. The emphasis is on the conservation and reproduction of the reference geostatistics.

Chapter 5 applies the method for calibration of multimodal parameter distributions, proposed in Chapter 4, to a real-world case. Here, the emphasis is on the difference between calibration results obtained with the proposed multimodal calibration method, and a conventional approach in which the different statistical populations are not allowed to change position. Moreover, the calibration of the multimodal parameter field is combined with co-calibration of other stochastic parameter fields.

References

Griffioen, J., J. Notenboom, G. Schraa, R.J. Schuurman, H. Runhaar, and G. van Wirdum (2003), Systeemgericht grondwaterbeheer, de natuurwetenschappelijke werking van grondwatersystemen in relatie tot ecosystemen en grondwaterbeheer, Wolters-Noordhoff, Groningen *(in Dutch)*.

Morris, B. L., A. R. L. Lawrence, P. J. C. Chilton, B. Adams, R. C. Calow, and B. A. Klinck (2003), Groundwater and its susceptibility to degradation: a global assessment of the problems and options for management. Early warning and assessment report series, RS. 03-3, United Nations Environment Programme, Nairobi, Kenya.

Younger, B. (2006), Groundwater in the environment, Blackwell Publishing, Boston, MA.

CHAPTER

2

Stochastic Analysis of Nonlinear Biodegradation in Regimes Controlled by both Chromatographic and Dispersive Mixing

Published in *Water Resources Research*, **2006**

[Janssen, G.M.C.M., O.A. Cirpka, and S.E.A.T.M. van der Zee (2006), Stochastic analysis of nonlinear biodegradation in regimes controlled by both chromatographic and dispersive mixing, *Water Resources Research*, 42, W01417, doi:10.1029/2005WR004042.]

Partly presented at *the International Workshop Saturated & Unsaturated Zone - Integration of process knowledge into effective models*, Rome, Italy, **2004**

[Van der Zee, S.E.A.T.M., R.C. Acharya, and G.M.C.M. Janssen (2004), Upscaling biogeochemically reactive chemical transport. In: Per Aagaard et al. (eds.), Proc. International Workshop Saturated & Unsaturated Zone - Integration of process knowledge into effective models, Rome, May 5-7, 2004, pp. 355-362.]

Partly presented at the *2nd International Workshop on Integrated Soil and Water Protection*, Prague, Czech Republic, **2004**

[Van der Zee, S.E.A.T.M., G.M.C.M. Janssen, and R.C. Acharya (2004), Upscaling biogeochemically reactive chemical transport in natural porous media. In: D. Halm and P. Grathwohl (eds.), Proc. 2nd Int. Workshop on Integrated Soil and Water Protection, Prague, June 28-29, 2004, pp. 62-66.]

2.1. Introduction

The performance of bioremediation strategies depends via complex relationships on both physical and chemical system parameters [e.g., *Oya and Valocchi*, 1997; *Keijzer et al.*, 1999]. In natural systems, these parameters generally exhibit considerable spatial variability, thus complicating the assessment of viability for bioremediation. In general, the probabilistic approach provides a systematic and natural framework for dealing with the uncertainties in flow and transport modeling caused by parameter variability [*Zhang*, 2002], and thus stochastic methods have proved their merits also in the modeling of bioremediation [*Ginn et al.*, 1995; *Miralles-Wilhelm et al.*, 1997; *Oya and Valocchi*, 1998; *Xin and Zhang*, 1998; *Kaluarachchi et al.*, 2000].

A convenient and practically relevant description of reactive transport in heterogeneous porous media is based on the analysis of solute arrival time, considering the statistical temporal moments of the contaminant mass flux through a control plane. A major conceptual and computational simplification is achieved by neglecting molecular diffusion and local dispersion. This allows conceptualizing reactive transport to occur in independent one-dimensional stream tubes, which are characterized by different travel times to the control plane. The breakthrough averaged over the entire control plane can then be calculated by averaging the one-dimensional transport solutions for all arrival times weighted by their respective arrival time probability density. This concept is referred to as the stochastic-convective stream tube approach, and is illustrated in Figure 1a. Note that the concentration gradients are very sharp, and that the largest fraction of the plume interface is parallel to the stream lines. *Ginn et al.* [1995], and later also *Xin and Zhang* [1998] and *Kaluarachchi et al.* [2000], used the approach in their stochastic analyses of nonlinear biodegradation.

Figure 1b, when compared with Figure 1a, illustrates the effect of pore-scale dispersion on the concentration distribution of an invading conservative solute. In the case of advective-dispersive transport (Figure 1b), the sharp concentration gradients from Figure 1a are smoothened, mainly by transverse dispersion. The double-headed arrows in Figure 1 highlight some locations in which plume fingers disappear due to exchange between stream tubes.

From Figure 1 it is clear that local scale dispersion induces mixing between the invading and receding solute. This mixing is essential for the process of bioremediation: for

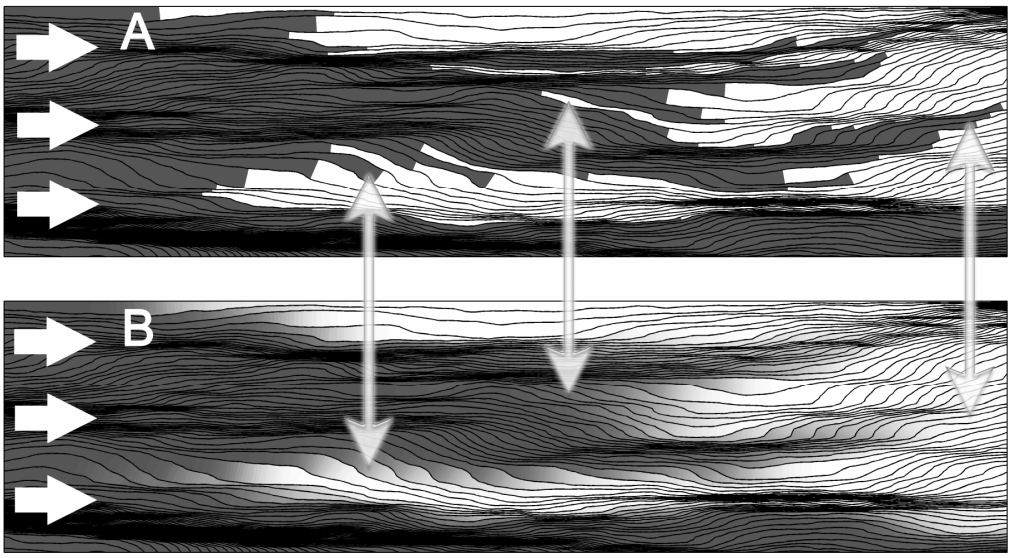

Figure 1. Effects of pore-scale dispersion on the concentration distribution for an invading solute. (A) Strictly advective transport. (B) Advective-dispersive transport. Single-headed arrows: direction of flow; double-headed arrows: regions of distinct differences.

microbial growth to occur, the electron acceptor and the contaminant have to be present at the same location at the same time.

Ginn [2001] extended the stochastic-convective approach to include longitudinal local scale dispersion. In heterogeneous media, however, transverse local scale dispersion is more important than the longitudinal counterpart because it leads to an exchange between fast and slow stream tubes, and the finger-like shape of the solute plume can dramatically increase the area over which transverse dispersion acts [*Cirpka et al.*, 1999a; *Cirpka*, 2002]. *Dagan and Fiori* [1997] and *Fiori and Dagan* [1999, 2000] reformulated the Lagrangian theory that is underlying the stream tube approaches to account also for transverse local-scale dispersion. Subsequently, *Fiori et al.* [2002] generalized the stochastic-convective stream tube approach accordingly, for the calculation of mass fluxes of conservative and linearly sorbing solutes. The strictly advective particle displacement and arrival time *pdf*'s that are used in the infinite Peclet number formulation of the Lagrangian framework are replaced by the joint displacement *pdf*'s and joint arrival time *pdf*'s for advective and dispersive movements. For conservative and linearly sorbing solutes this replacement works well, since their

concentrations only depend on travel time and are independent of the particular trajectory followed. However, in the case of nonlinear biodegradation, reaction rates depend on local concentrations (of contaminant, oxygen and microbial mass), which are all random. This means that the entire chemical concentration history of the trajectory has to be known to compute the net reaction that has occurred. Simply averaging over travel times is incorrect in this case.

Alternatively, *Cirpka and Kitanidis* [2000a] have developed the so-called advective-dispersive stream tube approach, in which they parameterize the effects of transverse dispersion as enhanced longitudinal dispersion, keeping the stream tubes independent of each other and directly affecting the reaction rates. The reasoning behind this approach is that the net effect of transverse dispersive mass transfer *between* stream tubes cannot be distinguished from that of longitudinal dispersion *within* the stream tubes. With equivalent parameters, both types of dispersion lead to the same amount of mixing between the invading and the receding solutions. The latter is observable in Figure 1b in which the smoothed concentration distribution could be obtained by either longitudinal or transverse local dispersion.

In this context, the central issue in including local scale dispersion is the choice of a dispersion coefficient that correctly describes the actual mixing process. It has been recognized in various studies [*Kapoor et al.*, 1997; *Kapoor and Kitanidis*, 1998; *Cirpka and Kitanidis*, 2000a] that standard macrodispersion coefficients overestimate dispersive mixing, since macrodispersion and dispersive mixing occur at different scales and the concentrations of the reactants are negatively correlated, partially as a result of the reaction itself. In fact, dispersive mixing should be regarded as one of two sub-processes of standard macrodispersion, the second one being advective spreading. To obtain correct reaction rates, these two sub-processes have to be separated.

In conservative transport, mixing of the invading and receding solutions leads to intermediate concentrations. Hence, *Cirpka and Kitanidis* [2000a,b] took the widths of local conservative breakthrough curves (observed at a single point), which they interpreted as if caused by longitudinal dispersion, as a measure of solute mixing, and applied the thus derived longitudinal dispersion coefficients to reactive transport simulations within non-interacting stream tubes. In a follow-up study, *Cirpka* [2002] reasoned that, in opposite time scales, effective dispersion is conceptually equivalent to

dispersive mixing, and therefore he proposed to use the effective dispersion coefficient as the longitudinal dispersion coefficient in the one-dimensional reactive transport calculations. The latter author showed that the overall rates of bimolecular reactions are well approximated by this approach. Using the stochastic-analytical derivations of the effective dispersion coefficient by *Dentz et al.* [2000] and *Fiori and Dagan* [2000], this method avoids time-consuming numerical evaluations of local breakthrough curves. *Vanderborght and Vereecken* [2002] derived the same quantity (now called equivalent dispersion coefficient) using a first-order Lagrangian approximation of the travel time statistics of local and integrated breakthrough curves, based on the work of *Dagan and Fiori* [1997] and *Fiori and Dagan* [1999, 2000].

Together with an appropriate description of the one-dimensional bioreactive transport process, the advective-dispersive stream tube model enables us to predict bioreactive transport not only in the regime controlled by chromatographic mixing, but also when local dispersion becomes relevant for mixing. Furthermore, it provides an excellent opportunity to evaluate the errors introduced by neglecting local scale dispersion in bioreactive transport modeling, without having to resort to time consuming, multi-dimensional numerical simulations. Such an assessment was called for by *Berglund and Cvetkovic* [1996], *Ginn* [1998], *Miralles-Wilhelm et al.* [1998] and *Kaluarachchi et al.* [2000]. So far, however, the advective-dispersive stream tube approach has not been tested for kinetic bioreactive transport, and this is the main purpose of the current study. In fact, this study is the first to incorporate local scale dispersion and the resulting time-dependent dispersive mixing in a stochastic-analytical description of (nonlinear and kinetic) bioreactive transport in heterogeneous porous media. The evaluation of the influence of local scale dispersion on the bioreactive transport process, and the implications for upscaling this process, is the second objective of this research.

For the description of the one-dimensional, Monod kinetic bioreactive reactive transport, we adopt the semi-analytical traveling wave solution of *Keijzer et al.* [2000]. Since this solution has never been implemented in a stream tube approach before, its applicability for this purpose will be validated separately by comparing analytical stochastic-convective calculations with numerical simulations, as a natural step towards the application of the solution in the more complex advective-dispersive approach. This validation counts as a third (intermediate) objective of the present study.

2.2. Mathematical Formulation of the Semi-Analytical Model

2.2.1. Heterogeneous Aquifer

Consider a three-dimensional aquifer with a spatially variable hydraulic conductivity field $K(\mathbf{x})$, assumed isotropic on the local scale, in which $\mathbf{x}(x_1,x_2,x_3)$ is the vector of Cartesian coordinates. We characterize the seemingly erratic spatial distribution $K(\mathbf{x})$, as observed in the field, in a geostatistical framework, assuming $K(\mathbf{x})$ to be a statistically stationary, anisotropic random space function. We adopt the common assumption that K is lognormally distributed [*Gelhar*, 1986; *Dagan*, 1989]. Thus, $K(\mathbf{x}) = K_G\exp(Y(\mathbf{x}))$, where K_G is the geometric mean of K and $Y(\mathbf{x})$ is a multi-Gaussian random space function with zero mean and variance σ_Y^2. We describe the spatial statistics of the log-conductivity fluctuation $Y(\mathbf{x})$ by an axisymmetric non-separable exponential covariance function [*Gelhar and Axness*, 1983]:

$$C_Y(r) = \sigma_Y^2\exp(-r) \tag{1}$$

where $r^2 = (r^2_1 + r^2_2)/I^2 + r^2_3/I^2_3$, and I and I_3 are the integral scales in the horizontal plane and the vertical direction, respectively. Throughout the study, we use an anisotropy ratio $e = I_3/I$ of 0.2.

We consider the variability of the porosity n negligible in comparison to the variability of K. We assume steady-state flow resulting from boundary conditions imposing a mean hydraulic gradient $\mathbf{J}$ oriented into the x_1 direction.

The groundwater velocity $\mathbf{v}(v_1,v_2,v_3)$ is related to K, n and $\mathbf{J}$ via Darcy's law, and since K is a random space function, so is $\mathbf{v}$. Since the porosity and the mean hydraulic gradient $\mathbf{J}$ are constant, the variations in $\mathbf{v}$ can be fully attributed to those in K. Furthermore, the mean velocity is given by $\langle\mathbf{v}\rangle = \mathbf{U} = (U, 0, 0)$ with $U = \langle v_1\rangle$.

2.2.2. Biodegradation Model

We aim at describing the mass flux of a biodegradable contaminant through a control plane, placed normal to the mean flow direction at $x_1 = b_1$. The contaminant undergoes instantaneous linear sorption and nonlinear degradation described by Monod kinetics. In the initial state, the contaminant is present everywhere in the flow domain with a

constant aqueous-phase concentration which is in equilibrium with the sorbed phase. Biodegradation is stimulated by continuous injection of water containing an electron acceptor through the injection plane which is placed normally to the mean flow at $x_1 = a_1 = 0$. The injection concentration of the electron acceptor is constant. The electron acceptor may undergo linear sorption at equilibrium. Water passing the injection plane is free of contaminant. We assume that the biomass is immobile and has a uniform initial concentration. The biomass can only grow if the electron acceptor and the mobile contaminant are simultaneously present at a particular position. Sorbed contaminant is assumed to be not bioavailable. Finally, we neglect biomass decay.

These assumptions lead to the following system of advection-dispersion-reaction equations [*Keijzer et al.*, 2000]:

$$R\frac{\partial g}{\partial t} = \nabla \cdot (\mathbf{D}\nabla g) - \mathbf{v} \cdot \nabla g - m_g \frac{\partial m}{\partial t}, \tag{2}$$

$$\frac{\partial c}{\partial t} = \nabla \cdot (\mathbf{D}\nabla c) - \mathbf{v} \cdot \nabla c - m_c \frac{\partial m}{\partial t}, \tag{3}$$

$$\frac{\partial m}{\partial t} = \mu_m \left(\frac{c}{k_c + c} \right) \left(\frac{g}{k_g + g} \right) m, \tag{4}$$

subject to

$c = 0$, $g = g_0$, $m = m_0$ for $x_1 \geq a_1$ at $t = 0$, (5a)

$c = c_0$, $g = 0$ for $t > 0$ at $x_1 = a_1$, (5b)

$\frac{\partial c}{\partial x_1} = 0$, $\frac{\partial g}{\partial x_1} = 0$ for $t > 0$ at $x_1 = b_1$, (5c)

in which c, g, and m are the dissolved electron acceptor, dissolved contaminant and biomass concentrations (mg/L), respectively, c_0, g_0 and m_0 are the inflow electron acceptor concentration (mg/L) and the initial contaminant and biomass concentrations (mg/L) in the domain, respectively, R is the ratio of the contaminant retardation factor over the electron acceptor retardation factor ($R > 1$ to guarantee chromatographic mixing), m_c and m_g (-) are the stoichiometric coefficients describing the ratios of

consumed electron acceptor and organic contaminant to assimilated biomass, μ_m (day^{-1}) is the maximum specific growth rate of biomass, k_c and k_g (mg/L) are the dissolved electron acceptor and contaminant half saturation constants, and t is time (in days).

Equations 2-5 fulfill the conditions for the development of a traveling wave in homogeneous media [*Dagan*, 1984; *van Duijn and Knabner*, 1992; *Bosma and van der Zee*, 1993]. A traveling wave exhibits a joint front of all concentrations propagating through the domain with constant speed and constant shape. The higher spatial moments (variance, skewness, and kurtosis) result from the balance that establishes between the front-spreading effect of local-scale dispersion and the front-sharpening effect of nonlinear biodegradation. *Keijzer et al.* [1999, 2000] derived a semi-analytical traveling wave solution (See Appendix A) for the model described by Eqs. 2-5. With numerical simulations, they showed that their solution describes the oxygen and contaminant fronts developing in homogeneous media rather accurately, at least after some relaxation time.

In the next Section, the homogeneous traveling wave solution is combined with a Lagrangian analysis of particle arrival time to model bioreactive transport in heterogeneous formations.

2.3. Stream Tube Approaches for Biodegradation

2.3.1. Stochastic-Convective Stream Tube Approach

Starting point of the stochastic-convective stream tube approach is the Lagrangian representation of transport by the position of a tagged solute particle of mass Δm by $\mathbf{X} = \mathbf{X}(t)$ [*Dagan*, 1984], where $\mathbf{X} = (X_1,X_2,X_3)$ describes the position of the particle in Cartesian coordinates, and $\mathbf{v}(t) = \mathbf{v}(\mathbf{X}(t))$ is the Lagrangian velocity. In the absence of molecular diffusion and pore scale dispersion, mass is conserved along the particle trajectory described by $\mathbf{X}(t)$, and transport essentially becomes one-dimensional.

We now consider a specific particle trajectory originating from a point $\mathbf{a}(0,a_2,a_3)$ in the injection plane which crosses the control plane in point $\mathbf{b}(b_1,b_2,b_3)$. Along this trajectory, the system of partial differential equations 2-4 becomes:

$$R\frac{\partial g}{\partial t} = -\frac{\partial g}{\partial \tau} - m_g \frac{\partial m}{\partial t}, \tag{6}$$

$$\frac{\partial c}{\partial t} = -\frac{\partial c}{\partial \tau} - m_c \frac{\partial m}{\partial t}, \tag{7}$$

$$\frac{\partial m}{\partial t} = \mu_m \left(\frac{c}{k_c + c} \right) \left(\frac{g}{k_g + g} \right) m, \tag{8}$$

subject to:

$$\begin{aligned} &c(\tau,0) = 0,\ g(\tau,0) = g_0,\ m(\tau,t) = m_0, \\ &c(0,t) = c_0,\ g(0,t) = 0, \\ &\frac{\partial c}{\partial t}\left(\frac{b_1}{U}, t\right) = 0, \qquad \frac{\partial g}{\partial \tau}\left(\frac{b_1}{U}, t\right) = 0 \end{aligned} \tag{9}$$

in which τ is the travel time:

$$\tau = \int_0^{b_1} \frac{1}{U + u_1(x_1)} dx_1, \tag{10}$$

where u_1 is the random deviation of the longitudinal velocity from its mean U [*Dagan and Cvetkovic*, 1996]. In the stochastic-convective framework (neglecting local scale dispersion), the expected contaminant mass flux through the control plane is now given by (see Appendix B for derivation):

$$\langle Q(t) \rangle = nUA^{IP} \int_\tau g(\tau, t)\, p(\tau; \mathrm{b}_1)\, \mathrm{d}\tau \tag{11}$$

where A_{ip} is the area of the injection plane. For the functional form of the arrival time probability density function (*pdf*) $p(\tau;b_1)$ we used the inverse Gaussian distribution [*Rao et al.*, 1981]. This distribution was also used in the following application of the advective-dispersive stream tube approach. For the stochastic-convective approach, $p(\tau;b_1)$ was parameterized using linear standard macrodispersion theory [*Gelhar and Axness*, 1983].

2.3.2. Advective-Dispersive Stream Tube Approach

Effectively, the advective-dispersive stream tube approach follows the same averaging equations as the stochastic-convective approach, but with different parameterization. As stated in the introduction, for a correct approximation of the reaction rates in the presence of local dispersion, the macrodispersion process has to be accurately separated in a mixing component and a strictly advective component.

In the advective-dispersive stream tube approach, transverse dispersion (the mixing component) is modeled as enhanced longitudinal dispersion. Like *Cirpka* [2002], we used the longitudinal effective dispersion coefficient D_l^e of a solute plume originating from a point-like injection to parameterize this enhanced dispersion. D_l^e was calculated using the stochastic-analytical derivations of *Dentz et al.* [2000] and *Fiori and Dagan* [2000].

Thus, the amount of effective dispersion a solute particle has undergone at time τ, can be approximated by the time-averaged value of D_l^e, $\overline{D}_l^e(\tau)$. The accurate reaction rates are now obtained by incorporating $\overline{D}_l^e$ into Eqs. 6 and 7:

$$R\frac{\partial g}{\partial t} = \overline{D}_l^e \frac{\partial^2 g}{\partial \tau^2} - \frac{\partial g}{\partial \tau} - m_g \frac{\partial m}{\partial t}, \tag{12}$$

$$\frac{\partial c}{\partial t} = \overline{D}_l^e \frac{\partial^2 c}{\partial \tau^2} - \frac{\partial c}{\partial \tau} - m_c \frac{\partial m}{\partial t} \tag{13}$$

The quantity D_l^e is conceptually equivalent to the longitudinal apparent dispersion coefficient of mixing D_a as defined in *Cirpka and Kitanidis* [2000a], where it was calculated by means of the numerical evaluation of local breakthrough curves (see introduction).

The correct amount of spreading (the strictly advective component) is achieved by parameterizing $p(\tau;b_1)$ in Eq. 11 with the expected arrival time (b_1/U) and the strictly advective variance of arrival times σ_{m1}^2, which can be approximated by the difference between the second central moment of the integrated breakthrough curve m_{2c}^* and the expected second central moment of breakthrough curves that is obtained locally ($\langle m_{2c} \rangle$) [*Cirpka and Kitanidis*, 2000a; *Cirpka*, 2002]:

$$\sigma_{m1}^2(\tau) = m_{2c}^*(\tau) - \langle m_{2c} \rangle(\tau) = \frac{X_{11}(\tau) - Z_{11}(\tau)}{U^2} = \frac{2}{U^2}\int_0^\tau \left(D_l^*(t) - D_l^e(t)\right)dt\,, \qquad (14)$$

where X_{11} and Z_{11} are the longitudinal one and two particle variance of displacements, respectively, and D_l^* is the longitudinal macrodispersion coefficient, which we evaluated using its first-order approximation as restated in *Cirpka* [2002].

In the calculations with both stream tube approaches, the ergodic hypothesis is assumed to be valid (A^{IP} is sufficiently large relative to the transverse integral scale I_3).

2.4. Numerical Simulations

To validate our analytical models, we performed two-dimensional numerical simulations. Since rectangular finite element grids are known to overestimate transverse dispersion by numerical diffusion and consequently also overestimate transverse mixing and biodegradation rates [*Cirpka et al.*, 1999a], we used stream line-oriented grids, generated as described in *Cirpka et al.* [1999b]. It was claimed by *Cirpka et al.* [1999a] that the only transverse transport mechanism in these grids is the transverse dispersion imposed by the modeler and therefore numerical dispersion is restricted to the longitudinal direction. Our numerical method is identical to that used by *Cirpka and Kitanidis* [2000a,b], to which we refer for details.

The grids represented 100m × 8m domains and were discretized into 1000 × 200 elements, resulting in average element dimensions of 0.1m × 0.04m, or 0.1I × 0.2I_3. By defining constant heads at the left and right boundaries of the domain, a mean hydraulic gradient **J** = (0.2,0,0) was imposed. A mean flow velocity U = 0.1 m/day was imposed by taking K_G = 0.2 m/day.

Simulations were performed for three degrees of heterogeneity: σ_Y^2 = 0, σ_Y^2 = 0.1, and σ_Y^2 =1.0. The latter case represents a reasonable upper limit estimation for σ_Y^2 for which the applied linear theory can still be assumed valid. This limit, however, has not been fully explored here or in previous work.

Since ergodic conditions are not met within a single realization of the domain, we performed Monte Carlo analyses, averaging breakthrough curves over 5 realizations for σ_Y^2 = 0.1 and 25 realizations for σ_Y^2 =1.0. These numbers of realizations appeared to be

Table 1. Parameter values for the base case. SC = stochastic-convective transport, AD = advective-dispersive transport

Biodegradation parameters		**Flow and transport parameters**	
μ_m	0.05 day^{-1}	J_1	0.2 m/m
m_c	1.0 mg/mg	U	0.1 m/day
m_g	5.0 mg/mg	R	3.0
k_c	1.0 mg/L	$\alpha_L = \alpha_T$ (SC)	0.0 m
k_g	2.0 mg/L	$\alpha_L = \alpha_T$ (AD)	$5 \cdot 10^{-2}$, $5 \cdot 10^{-3}$ or $5 \cdot 10^{-4}$ m
Initial concentrations		**Soil parameters**	
c_0	10.0 mg/L	n	0.4
g_0	5.0 mg/L	K_G	0.2 m/day
m_0	0.427 mg/L	I	1.0 m
		I_3	0.2 m

sufficient to achieve convergence of the results. This series of calculations was performed two times: once for the purely convective case, setting the isotropic dispersivity ($\alpha_L = \alpha_T$) at 0m, and once for the advective-dispersive case, setting $\alpha_L = \alpha_T = 5 \cdot 10^{-3}$ m. In all simulations, the parameter values of the base case (Table 1) were used. Additionally, the numerical calculations with $\sigma_Y^2 = 0.1$ were repeated for a more distant control plane (at 300 m, the numerical grids were extended accordingly using the same discretization as described above) and for three different values of the isotropic dispersivity ($\alpha_L = \alpha_T = 5 \cdot 10^{-2}$ m, $5 \cdot 10^{-3}$ m, and $5 \cdot 10^{-4}$ m).

2.5. Results and Discussion

2.5.1. Introduction

We avoid a discussion on effective hydraulic conductivities as we normalize the time axes of the numerical breakthrough curves with the ratio of the theoretical average conservative breakthrough time (b_1/U) over the observed average breakthrough time from numerical tracer experiments $<BT_{num}>$. Furthermore, to facilitate comparisons

between the semi-analytical model and numerical simulation, we scale the time axes to a dimensionless quantity with the relative celerity α of the traveling wave in comparison to the mean seepage velocity U and the integral scale I:

$$t' = \frac{(b_1/U)}{\langle \mathrm{BT}_{\mathrm{num}} \rangle} \times \frac{t\alpha U}{I} = t \frac{b_1 \alpha}{\langle \mathrm{BT}_{\mathrm{num}} \rangle I}, \tag{15}$$

in which the relative celerity α of the traveling wave is given by *Keijzer et al.* [2000]:

$$\alpha = \frac{1 + (m_c g_0)/(m_g c_0)}{1 + R(m_c g_0)/(m_g c_0)} \tag{16}$$

For analytical breakthrough curves, naturally, the normalization term $(b_1/U)/\langle \mathrm{BT}_{\mathrm{num}} \rangle$ occurring in Eq. 15 is omitted. For conservative breakthrough curves, the normalization term α is omitted.

The expected mass fluxes are also scaled to a dimensionless form, using

$$\langle Q' \rangle = \frac{\langle Q \rangle}{\langle Q_0 \rangle g_0} \tag{17}$$

where $\langle Q_0 \rangle = nUA^{\mathrm{IP}}$ is the mean fluid discharge through the injection plane.

The first moment M_1, second central moment M_2^c, skewness γ and kurtosis κ of the breakthrough curves are calculated as follows:

$$M_1 = -\frac{1}{g_0} \int_0^\infty \frac{\partial g}{\partial t} dt \,, M_2^c = -\frac{1}{g_0} \int_0^\infty (t - M_1)^2 \frac{\partial g}{\partial t} dt \tag{18}$$

$$\gamma = \frac{-\int_0^\infty (t - M_1)^3 \frac{\partial g}{\partial t} dt}{g_0 \sqrt{(M_2^c)^3}} \,, \kappa = \frac{-\int_0^\infty (t - M_1)^4 \frac{\partial g}{\partial t} dt}{g_0 (M_2^c)^2} \tag{19}$$

For comparison, it may be noted that the second central moment M_2^c, skewness γ, and kurtosis κ of the traveling wave solution for a homogeneous aquifer are constant because the wave does not change its shape when traveling through the domain. By contrast, the temporal moments for one-dimensional, Fickian, conservative transport are:

$$M_2^c = \frac{2Dx}{v^3},\ \gamma = 3\sqrt{\frac{2D}{vx}},\ \kappa = 3 + \frac{30D}{vx} \tag{20}$$

2.5.2. Coupled Effects of Nonlinear Biodegradation and Heterogeneity

Strictly speaking, the semi-analytical expression of *Keijzer et al.* [2000] does not apply for conditions with zero local scale dispersion. Figure 2, however, shows that the simulated breakthrough curve of the contaminant in a homogeneous system is insensitive to a further decrease of the longitudinal dispersivity α_L if the value is smaller than 0.005m. In this regime, there is still a balance between front spreading and sharpening, but the front shape is almost completely determined by nonlinear biodegradation. Therefore, we evaluate the one-dimensional semi-analytical solution for $g(\tau,t)$ of *Keijzer et al.* [2000] with α_L = 0.005m and consider it as an approximate solution of Eqs. 6-9 for zero local scale dispersion.

Figure 3a shows a comparison of dimensionless breakthrough curves of the

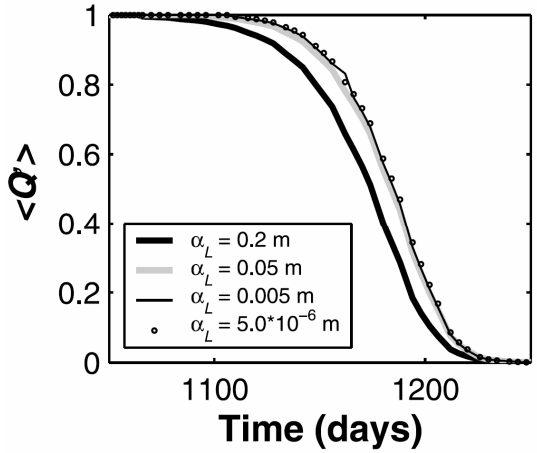

Figure 2. Homogeneous breakthrough curves for different values of α_L, calculated with the analytical traveling-wave solution of Eqs. 2-5 using the base-case parameters.

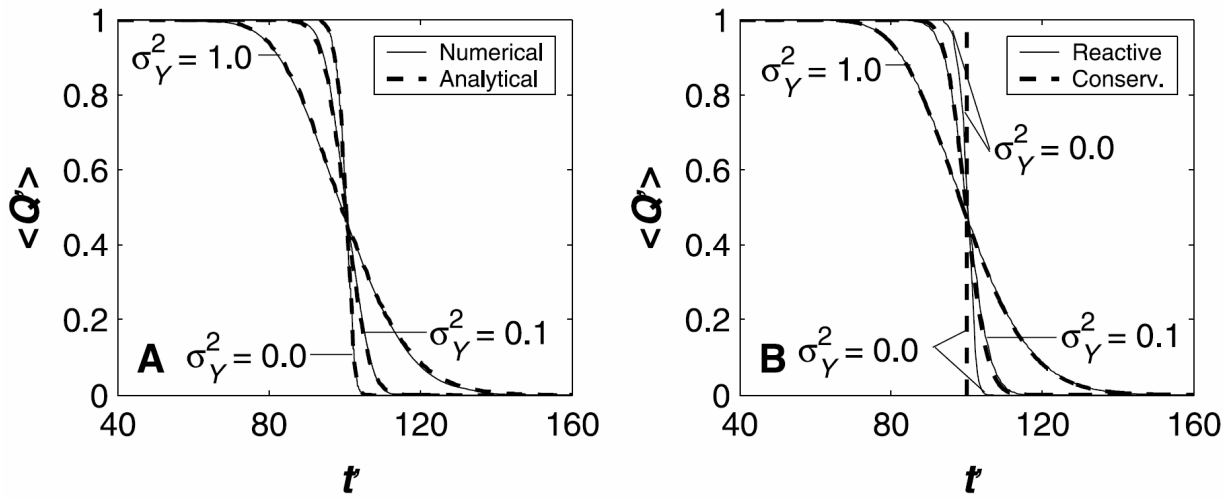

Figure 3. (a) Comparison of results from the analytical stochastic-convective model with results from numerical simulations using the base case parameters. (b) Comparison of reactive breakthrough curves with conservative breakthrough curves, both calculated analytically.

contaminant based on the analytical stochastic-convective model and on numerical simulations with zero dispersion ($\alpha_L = \alpha_T = 0$m). Evidently, the analytical model grasps the controlling transport processes embedded in Eqs. 6-9 excellently, since the match between analytical and numerical results is almost perfect. This justifies using our analytical model for stochastic-convective analyses.

In Figure 3b, the reactive breakthrough curves are compared to the breakthrough curves of a conservative solute. This figure translates results previously obtained for nonlinear sorption (e.g. *Berglund and Cvetkovic* [1996]) to the present context of nonlinear biodegradation. In particular, the result for $\sigma_Y^2 = 0$ reveals that the bioreactive breakthrough curve is more spread than the conservative curve, which shows plug flow behavior. Moreover, the reactive breakthrough curve increasingly resembles the conservative breakthrough curve for increasing degree of heterogeneity. This implies that, as heterogeneity increases, the *pdf* of arrival time starts to dictate the contaminant mass arrival rather than the actual shape of the traveling wave front, which is determined by nonlinear biodegradation.

2.5.3. Effect of Local scale Dispersion

2.5.3.1. Validation of the Advective-Dispersive Stream Tube Approach

Figure 4a shows the contaminant breakthrough curves, obtained both analytically (with the advective-dispersive stream tube approach) and numerically, for the base case incorporating local-scale dispersion ($\alpha_L = \alpha_T = 0.005$m). Figure 4b gives the development

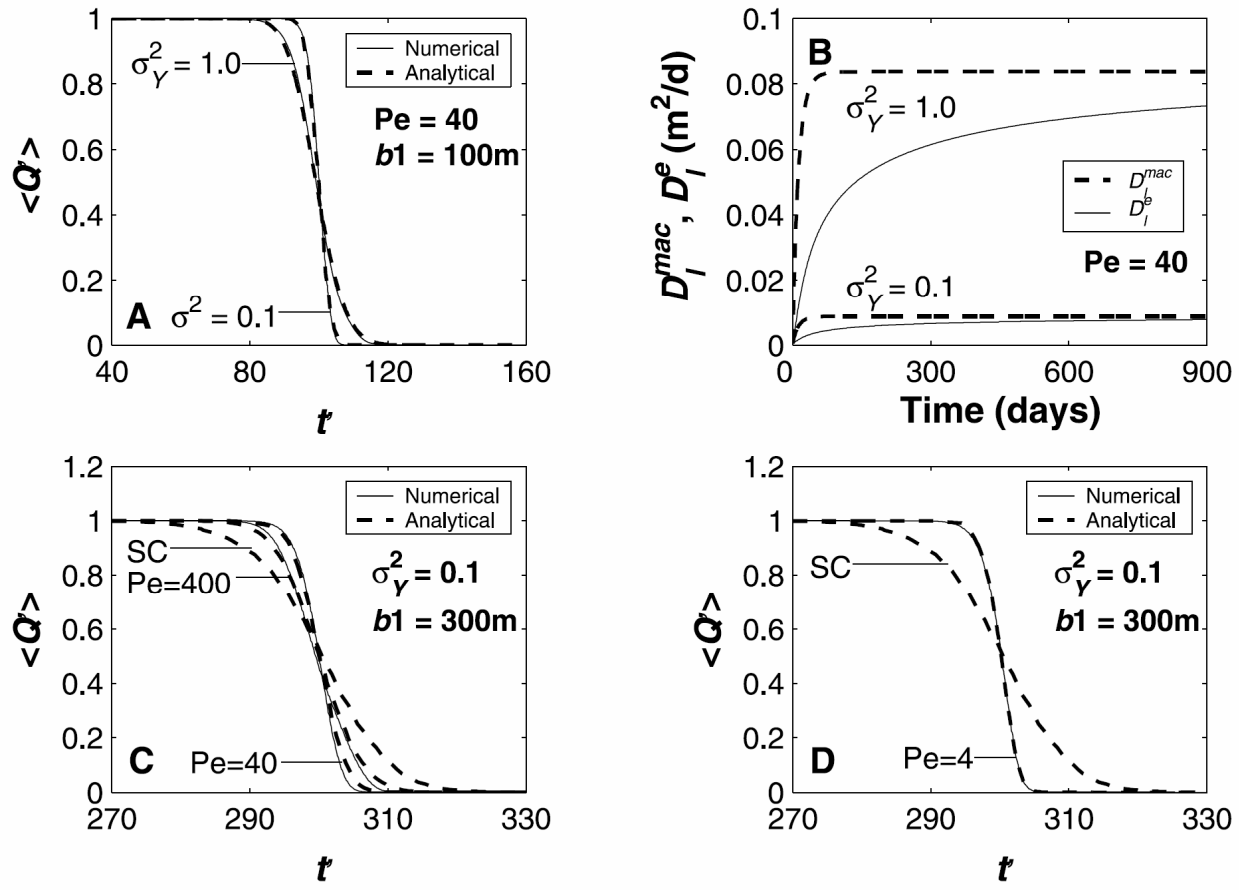

Figure 4. (a) Comparison of results from the analytical advective-dispersive model with results from numerical simulations using the base case parameters. (b) Development of the macrodispersion coefficient (D_l^{mac}) and the effective dispersion coefficient (D_l^e) for a conservative solute when transported from the injection plane to the control plane, calculated using the base case parameters (where applicable). (c and d) Comparison of analytical results with numerical results ($\sigma_Y^2 = 0.1$) for a more distant control plane (300 m) and for three different Pe values. For completeness, the stochastic-convective result (SC) is also shown.

of the macro- and effective dispersion coefficient as a function of time, and shows that in the base case the control plane is located far enough from the injection plane for local dispersive mixing to become important. In fact, by the time needed for a conservative solute to reach the control plane, the time-averaged effective dispersivity has reached 76% of the time-averaged macrodispersivity for both the σ_Y^2 = 0.1 as the σ_Y^2 = 1.0 case. From Figure 4a it is clear that, in the displayed examples, the analytical model correctly incorporates the influence of this mixing on the transport process.

Figures 4c and 4d gives additional comparisons between numerical and analytical results, now for a more distant control plane (300 m) and for three different values of the inverse dimensionless transverse dispersivity (= Pe = l_3/α_T = 4, 40 and 400) (these calculations were carried out only for the σ_Y^2 = 0.1 case, because the time needed to perform a sufficient number of numerical Monte Carlo runs for the σ_Y^2 = 1.0 case is excessive). Again we observe a good agreement between the numerical and analytical results, and the comparisons constitute additional confirmation that the advective-dispersive stream tube model is applicable to bioreactive transport. Using the analytical model to analyze the effect of local scale dispersion in more detail is therefore justified.

2.5.3.2. Nonlinear bioreactive transport versus conservative and linear sorptive transport

Berglund [1997], *Dagan and Fiori* [1997], *Andricevic and Cvetkovic* [1998], *Fiori and Dagan* [2000] and *Fiori et al.* [2002] have proved or stated that, for conservative and linear sorptive transport, transverse local scale dispersion only has a limited influence on the expected value of concentrations and fluxes, and primarily affects the concentration variance and the flux variance. Indeed, Figure 5b, showing for σ_Y^2 = 0.1 and for three different Pe values (Pe = 4, 40 and 400) the development of the cross-sectional integrated second central moment of the breakthrough curves as a function of the distance between injection and control plane for the conservative equivalent of our base case scenario, illustrates that even for Pe = 40 (which is relatively low as Pe is generally assumed to be larger than 100 in practical groundwater applications), transverse dispersion hardly affects the expected breakthrough. In practical applications, disregarding pore scale dispersion altogether for nonreactive or linear sorptive transport is therefore usually justified when the focus is on expected values [*Fiori and Dagan*,

2000]. However, from Figure 5a, showing the development of the second central moment of the reactive breakthrough curves, it is clear that in our bioreactive context transverse dispersion significantly affects the expected breakthrough even for the largest value of Pe we investigated (Pe = 400). We can understand the different behavior of nonlinearly biodegradable contaminants compared with conservative or linearly sorbing

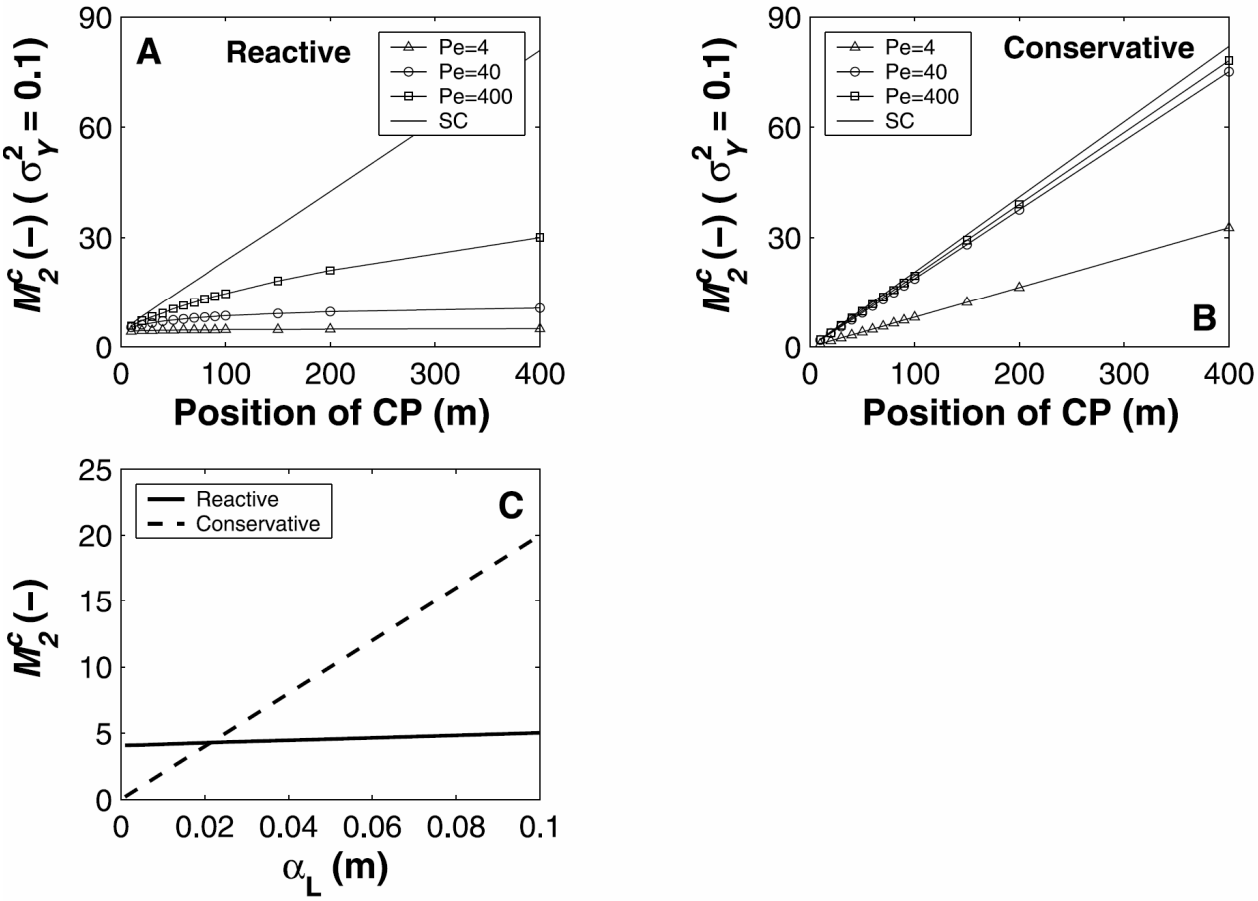

Figure 5. Development of the bioreactive (a) and conservative (b) second central moment of the expected contaminant breakthrough curves in the stochastic-convective (SC, no dispersion!) and the advective-dispersive stream tube (finite Pe numbers) model as a function of the distance between injection and observation plane. (c) Comparison of the effect of increasing longitudinal dispersion on the bioreactive and conservative second central moments of the homogeneous (σ_Y^2 = 0.0) breakthrough curves (CP at 100 m). The conservative moments were calculated using Eq. 20. The value of the non-zero reactive second central moment for α_L = 0 depends on the biochemical parameters used [*Oya and Valocchi*, 1997; *Keijzer et al.*, 1999].

solutes by considering again Figure 4b. The (conservative) macrodispersion coefficient quickly reaches its asymptotic level, which results in a linear increase with distance (or time) of the second central moment of the integrated breakthrough curve (m_{2c}^{*}) of a conservative solute. We observed this behavior in Figure 5b. The effective dispersion coefficient, however, only gradually catches up with the macrodispersion coefficient (and, as we will see later, never completely reaches it). This causes the second central moments of the conservative local breakthrough curves ($\langle m_{2c} \rangle$) to increase exponentially with distance (or time) throughout the simulation. Since $m_{2c}^{*} - \langle m_{2c} \rangle = \sigma_{m1}^{2}$ [*Cirpka and Kitanidis*, 2000a], strictly advective spreading slows down with distance. In fact, in 2-D, the large-distance value of σ_{m1}^{2}, scales with the square-root of *x* [*Dentz et al.*, 2000; *Fiori and Dagan*, 2000]. In case of conservative or linear sorptive transport, the retarded advective spreading is almost completely compensated by the accelerated spreading of the local (intra-stream tube) fronts for realistic Peclet values. In our case of nonlinear biodegradation, however, the spreading of the intra-stream tube fronts is counterbalanced by the (front-sharpening) reaction. Indeed, Figure 5c, comparing the one-dimensional second central moments of reactive and conservative breakthrough curves for a range of longitudinal dispersivity values, illustrates that the reactive intra-stream tube breakthrough curves are relatively insensitive to enhanced longitudinal dispersion when compared with the conservative case. Thus, the retarded advective spreading is only partially compensated, resulting in a concave development of the second central moments of the reactive breakthrough curves (see Figure 5a).

The concave shape of the reactive breakthrough curves observed for all finite Pe numbers causes the error in predicting the breakthrough by neglecting transverse dispersion to increases with time. Thus, although reaction rates will be dominated by chromatographic effects in the large-time domain [*Oya and Valocchi*, 1998; *Cirpka et al.*, 1999a], enlarging the domain does not attenuate the difference between the advective-dispersive and stochastic-convective results, as was hypothesized in earlier publications (e.g. *Cirpka et al.* [1999a] and *Cirpka and Kitanidis* [2000a]).

2.5.3.3. Nonlinear bioreactive asymptotic behavior versus Fickian and traveling wave behavior

A closer look at Figure 5a reveals that the second central moment does not reach a constant value in any case, which means that, as opposed to the homogeneous case, no traveling waves develop in the heterogeneous case. We can understand this by analyzing Eq. 11, which states that the flux-averaged concentration is a convolution of the traveling wave solution with the *pdf* of advective arrival times $p(\tau;b_1)$. The second and higher central moments of a convolution integral, such as the one in Eq. 11, equals the sum of the central moments of the convoluted functions. Hence, the second central moment of the substrate-breakthrough curve, equals the constant value of the traveling wave plus the value of σ_{m1}^2, which is used to parameterize $p(\tau;b_1)$. As stated before, σ_{m1}^2 does not approach an asymptotic value, but its large-distance value scales with the square-root of *x*. This implies that assuming the difference between the macro- and effective dispersion coefficient (a measure of advective spreading) to become irrelevant at large time [*Kapoor et al.*, 1997; *Kapoor and Kitanidis*, 1998; *Miralles-Wilhelm et al.*, 1998] is not justified for our case. Biodegradation models that are based on this assumption [*Miralles-Wilhelm et al.*, 1997; *Oya and Valocchi*, 1998]) may therefore not apply either: only in extreme (and unrealistic) cases (for example, for Pe = 4 the second central moment can be argued to reach a practically constant value), they may be a valid approximation, applicable in breakthrough predictions.

Just like it is erroneous to assume that nonlinear effects will start to dominate in the large time regime (leading to traveling wave behavior), it is also incorrect to assume that the heterogeneity effects will control the transport process, as is shown in Figure 6. In this figure, the development of the higher order moments (skewness and kurtosis) of the bioreactive breakthrough curve are compared with the moments of breakthrough curves assuming Fickian behavior (indicated by grey lines). In Section 2.5.2 it was shown that if the nonlinear effects of biodegradation can be neglected (which leads to Fickian behavior), dimensionless reactive breakthrough curves equal dimensionless conservative breakthrough curves. Therefore, dimensionless reactive Fickian behavior follows Eq. 20, taking for *D* the time-averaged macrodispersion coefficient. This Fickian behavior was calculated for the extreme cases of extensive mixing (Pe = 4) and no mixing (SC). Again it shows that the moments of the nonlinear bioreactive breakthrough

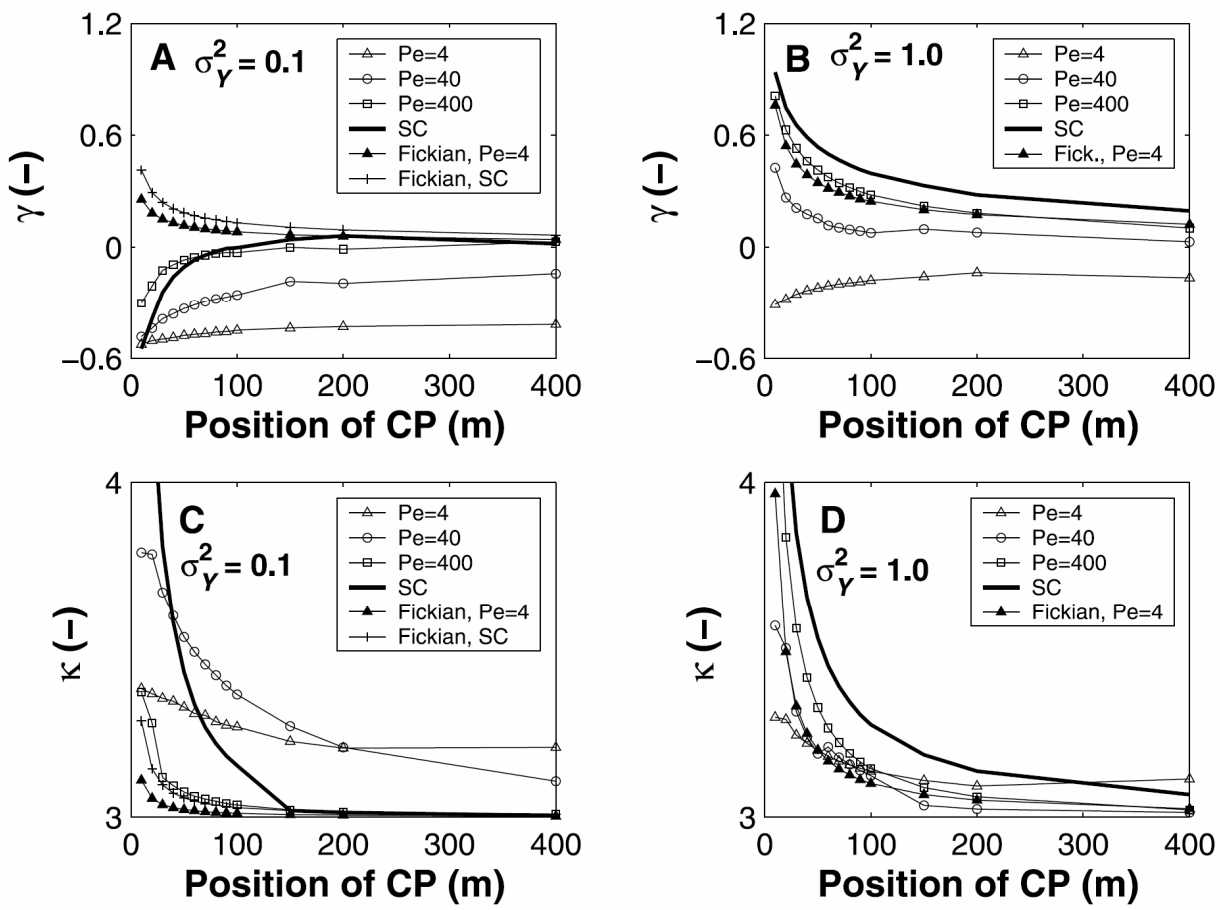

Figure 6. Development of skewness (a and b, for the σ_Y^2 = 0.1 and 1.0 case, respectively) and kurtosis (c and d, for the σ_Y^2 = 0.1 and 1.0 case, respectively) of the expected contaminant breakthrough curves in the stochastic-convective (SC), advective-dispersive stream tube (finite Pe numbers) and Fickian model as a function of the distance between injection and observation plane. In (a) and (c), the curves for Fickian, Pe = 40 and 400, coincide approximately with the "Fickian, SC" curve and were therefore omitted to keep the figures clear. In (b) and (d), the curves for Fickian, SC, Pe = 40 and Pe = 400 all coincide approximately with the "SC" curve and were therefore omitted also.

curves are much more affected by mixing than the Fickian breakthrough curves. Moreover, comparison of the Fickian behavior with our advective-dispersive results reveals that none of the advective-dispersive cases approximate Fickian behavior within

relevant distances, which means that all cases are significantly influenced by the nonlinear effects.

2.5.3.4. The role of the relative retardation factor

It has been hypothesized in the literature (e.g. *Oya and Valocchi* [1998] and *Cirpka and Kitanidis* [2000a]) that, if the retardation difference between the reacting species is large enough, the stochastic-convective model is applicable, because chromatographic mixing would dominate over dispersive mixing in determining the reaction rates [*Oya and Valocchi*, 1998]. In Figure 7, we investigate this hypothesis in more detail. We consider a travel distance of 100m, and compute the second central moments of the integrated breakthrough curves (M_2^c) for increasing values of the retardation factor R, while keeping the total amount of the contaminant in the system constant by decreasing g_0 with the same factor R is increased with. We will call this simultaneous variation of R and g_0 a variation in R^*. In Figs. 7a and 7b, σ_Y^2 is 0.01, whereas in Figs. 7c and 7d, it is 1.0. Figs. 7a and 7c show dimensionless M_2^c (scaled with $(IU\alpha)^2$) as a function of R^*, whereas Figs. 7b and 7d show dimensional M_2^c.

In the low variance case (Fig. 7a), front shapes are dominated by the shape of the one-dimensional traveling wave, which shows a dramatic and monotonic increase with R^* (see the grey line in Fig. 7a) that can be explained by the decreasing contaminant concentration in the aqueous phase (g_0), inducing a smaller microbial growth rate. In fact, the influence of g_0 on the traveling wave's M_2^c is so large that even in the high variance case (Fig. 7c), R^* still affects the shape of the integrated breakthrough curve. In the low variance case, effects of local scale dispersion are small because of limited plume fingering. Therefore, the (constant) difference between the dimensionless stochastic-convective and advective-dispersive results is small and, by virtue of the increasing value of M_2^c with R^*, even becomes insignificant for larger R^*. To calculate the dimensional error induced by neglecting local scale dispersion, this constant difference has to be divided by $(IU\alpha)^2$ (Fig. 7b). It should be noted that increasing R^* yields an asymptotic minimum for α (see Eq. 16) and therefore an asymptotic maximum for the dimensional error. So, also in the dimensional setting the error becomes relatively insignificant with increasing R^*.

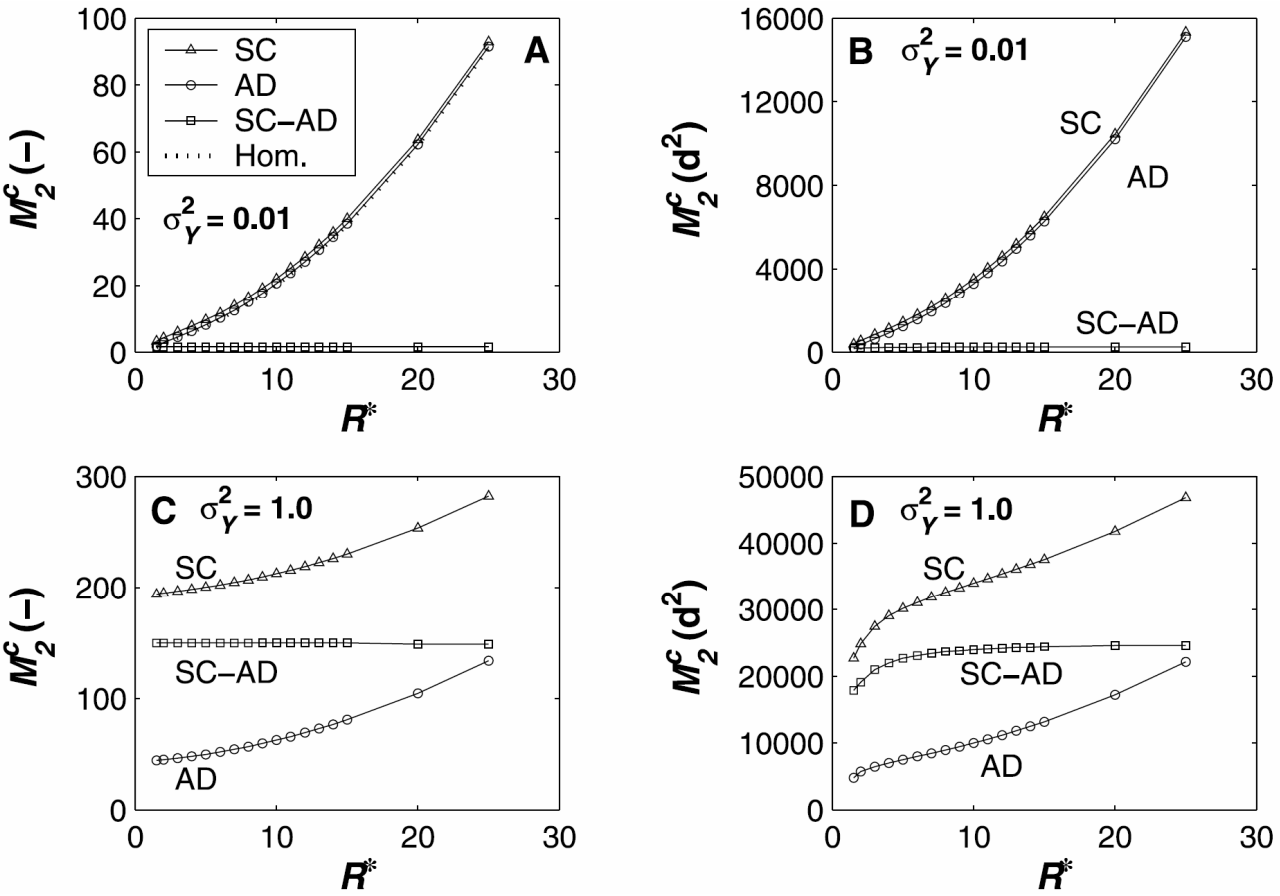

Figure 7. Dimensionless and dimensional (d = days) second central moments of the breakthrough curves as a function of R^*, as calculated with the stochastic-convective model (SC) and the advective-dispersive model (AD), for three degrees of heterogeneity: $\sigma_Y^2 = 0.0$ (see (a), curve "Homogeneous"), $\sigma_Y^2 = 0.01$ (see (a) for dimensionless and (b) for dimensional BTC's) and $\sigma_Y^2 = 1.0$ (see (c) for dimensionless and (d) for dimensional BTC's). The difference between the second central moments as calculated by SC and AD is also shown (SC-AD).

In the high variance case and in a dimensionless setting (Fig. 7c), the difference between the stochastic-convective and the advective-dispersive formulation is almost fully determined by the different $p(\tau;b_1)$ used in both approaches (see the discussion of Figure 5). In contrast to the low variance case, the difference (the error) is now considerable, and in the dimensional setting (Fig. 7d) the asymptotic value of the error

remains to be significant compared to the absolute value of the correct second central moments (as given by the "AD" curve).

Fig. 7 was calculated for a relatively low Peclet value (Pe= 40), and the effects of local scale dispersion displayed in this figure are therefore magnified. Figure 4a, however, already showed that also for Pe = 400 the effect of local scale dispersion on the mean contaminant flux is considerable, especially in the large-time, large-displacement regime. Having learned from Figure 7 that the absolute error induced by neglecting local scale dispersion hardly changes with increasing R^*, we can conclude that even for a range of realistic Peclet values, the intensified chromatographic mixing that results from increasing R^* still does not allow neglecting the contribution of dispersive mixing to the total mixing process, and application of the stochastic-convective stream tube approach is not warranted.

2.6. Conclusions

The semi-analytical one-dimensional traveling wave solution for nonlinear biodegradation of *Keijzer et al.* [2000] provides an accurate and efficient way for the calculation of the concentration profiles along the stream tubes in the stochastic-convective and advective-dispersive stream tube approaches.

We showed that the advective-dispersive stream tube approach developed by *Cirpka and Kitanidis* [2000a] is applicable to bioreactive transport. The analyses conducted with this model revealed that for nonlinear bioreactive transport, in contrast to conservative and linearly sorbing solutes, the shape of the integrated breakthrough curves are significantly affected by local scale dispersion, even for realistic Peclet values. The error induced by neglecting local scale dispersion (as is done in the stochastic-convective approach) was shown to increase with increasing time. Also, even for very high retardation differences between contaminant and electron acceptor, significant discrepancies were observed between results obtained with the stochastic-convective and the advective-dispersive model. Both observations indicate that, although reaction rates may be dominated by chromatographic mixing for larger time and larger R, the dispersive mixing process remains important for the prediction of contaminant transport in heterogeneous porous media. So, the advective-dispersive transport process can

generally not be approximated with a stochastic-convective stream tube approach, even in large-time, large-domain problems or in cases with large retardation differences between the reactants.

The results of the stochastic analysis with the advective-dispersive stream tube model also revealed that in the typical parameter range of σ_Y^2 and α_T, and at typical travel distances, the macroscopic displacement behavior neither may be parameterized by an equivalent homogeneous medium (in which a traveling wave would develop), nor is it Fickian. In theory, this Chapter revealed that traveling wave behavior (dominated by local nonlinearity) and Fickian behavior (dominated by heterogeneity) are limiting cases for nonlinear transport. This implies that describing macroscopic transport with a convection-dispersion equation that is adjusted with nonlinear interaction terms (as is done in many scientific and commercial codes) might be erroneous. For parameter ranges in the transition between nonlinear and heterogeneity dominance cases, it is not obvious how the macroscopic governing equations should read instead.

Notation

a	vector of Cartesian coordinates at the injection plane
a_i	x_i coordinate at the injection plane
A^{IP}	area of the injection plane
b	vector of Cartesian coordinates at the control plane
b_i	x_i coordinate at the control plane
BT_{num}	observed breakthrough time from numerical experiments
c	dissolved electron acceptor concentration
c_0	inflow electron acceptor concentration
C_Y	spatial covariance of Y
D	dispersion tensor
D	dispersion coefficient
D_l^*	longitudinal macrodispersion coefficient
D_l^e	longitudinal effective dispersion coefficient
$\overline{D}_l^e$	time-averaged effective dispersion coefficient
e	anisotropy ratio (= I_3/I)

g	dissolved contaminant concentration
g_0	initial dissolved contaminant concentration
I, I_3	integral scale in the horizontal and vertical direction, respectively
J	hydraulic gradient tensor
k_c	dissolved electron acceptor half saturation constant
k_g	dissolved contaminant half saturation constant
K	hydraulic conductivity
K_G	geometric mean of K
m	biomass concentration
m_c	ratio of electron acceptor consumption to biomass assimilation
m_g	ratio of contaminant consumption to biomass assimilation
m_0	initial biomass concentration
m_{2c}	second central moment of a local breakthrough curve (conservative)
m^*_{2c}	second central moment of the integrated breakthrough curve (conservative)
M_1	first moment of the contaminant breakthrough curve
M^c_2	second central moment of the contaminant breakthrough curve
n	porosity
p	arrival time probability density function
Pe	Peclet number (= I_3/α_T)
Q	contaminant mass flux through the control plane
Q'	scaled contaminant mass flux through the control plane
$\langle Q_0 \rangle$	mean fluid discharge through the injection plane
R	relative retardation factor
r	lag distance
R^*	indicates that R is varied with the total amount of contaminant kept constant
t	time
t'	dimensionless time
U	mean groundwater velocity vector
U	mean velocity in the horizontal direction (= $<v_1>$)
v	groundwater velocity tensor

v_i	groundwater velocity in the direction i
x	vector of Cartesian coordinates
x_i	spatial coordinate along the direction i
X	position of a solute particle
X_{11}	longitudinal one particle variance of displacement
Y	natural logarithm of K
Z_{11}	longitudinal two particles variance of displacement
α	relative celerity of the traveling wave
α_L	longitudinal dispersivity
α_T	transversal dispersivity
γ	skewness of the contaminant breakthrough curve
κ	kurtosis of the contaminant breakthrough curve
μ_m	maximum specific growth rate of biomass
σ^2_{m1}	strictly advective variance of arrival times
σ^2_Y	variance of Y
τ	travel time

Appendix A Semi-analytical Traveling Wave Solution

Keijzer et al. [2000] derived semi-analytical solutions that describe the distribution of the contaminant and electron acceptor concentration and the microbial mass. To determine these distributions, they transformed the system of equations (2-4) subject to Eq. 5 into a nonlinear second order ordinary differential equation (ODE) system, using two newly defined functions of c, i.e. u and w:

$$u(c) = -\frac{\partial c}{\partial \tau}, \quad w(c) = \frac{\partial g}{\partial \tau}. \tag{A1}$$

The nonlinear second order ODE system is solved using an iterative procedure. In each iteration step, u and w are determined by Newton's method. After the iteration, the function u is integrated numerically from a reference point with a designated chosen c.

Therefore, the solutions are unique up to a constant translate which is determined by mass balance considerations.

Appendix B Stochastic-Convective Stream Tube Approach

For ease of reference, the stochastic-convective stream tube formulation that leads to Eq. 11 is repeated here. Consider again a specific particle trajectory originating from a point **a**$(0,a_2,a_3)$ in the injection plane which crosses the control plane in point **b**(b_1,b_2,b_3). The mass-flux density $q_{sl}(t,b_1)$ through the control plane at this specific stream line is given by:

$$q_{sl}(\tau,t,b_1) = n(U+u_1(b_1))g(\tau,t) \qquad \text{(B1)}$$

where n is the effective porosity. It follows that the contaminant mass flux q_{st} in a stream tube originating from an elementary area dA^{IP} (= da_2da_3) in the injection plane and crossing the control plane through an elementary area dA^{CP} (= db_2db_3), is:

$$q_{st}(\tau,t) = n\int_{dA^{CP}}(U+u_1(b_1))g(\tau,t)d\mathbf{b} = n\int_{dA^{IP}}(U+u_1(a_1))g(\tau,t)d\mathbf{a} \qquad \text{(B2)}$$

in which the second equality follows from the Eulerian fluid continuity equation [*Dagan and Cvetkovic*, 1996]. For the contaminant mass flux $Q(t)$, integrated over the entire control plane, we arrive at:

$$Q(\tau,t) = n\int_{A^{IP}}(U+u_1(a_1))g(\tau,t)d\mathbf{a}\,, \qquad \text{(B3)}$$

in which A^{IP} is the area of the injection plane. In Eq. B3, both u_1 and τ are random variables, implying that for the calculation of the expected contaminant mass flux $<Q(t)>$ their joint probability density function $f(\tau,U+u_1;b_1)$ is required:

$$\left\langle Q(t;\mathrm{b}_1)\right\rangle = nA^{IP}\int_{\tau}\int_{u_1}(U+u_1(\mathrm{a}_1))g(\tau,t)f(\tau,U+u_1;\mathrm{b}_1)\mathrm{d}u_1\mathrm{d}\tau \qquad \text{(B4)}$$

In Eq. B4, the dependency on **a** is dropped since in a statistically stationary velocity field with mean flow normal to the injection and control planes, the travel time distribution only depends on the distance b_1-a_1 = b_1 [*Dagan et al.*, 1992]. Further simplification can be achieved by assuming that *g* is independent of u_1, which allows us to replace the joint *pdf* by the velocity-weighted marginal *pdf* or travel time $p(\tau;b_1)$ [*Dagan and Cvetkovic*, 1996; *Berglund*, 1997]:

$$\left\langle Q(t;\mathrm{b}_1)\right\rangle = nUA^{IP}\int_{\tau} g(\tau,t)p(\tau;\mathrm{b}_1)\mathrm{d}\tau \qquad \text{(B5)}$$

References

Andricevic, R., and V. D. Cvetkovic (1998), Relative dispersion for solute flux in aquifers, *J. Fluid Mech.*, 361, 145-174.

Berglund, S. (1997), Groundwater Contamination: Significance of Hydrochemical Processes for Remediation and Impact Evaluation, Ph.D. thesis, Royal Institute of Technology, Sweden, Stockholm.

Berglund, S., and V. D. Cvetkovic (1996), Contaminant displacement in aquifers: Coupled effects of flow heterogeneity and nonlinear sorption, *Water Resour. Res.*, 32, 23-32.

Bosma, W. J. P., and S. E. A. T. M. van der Zee (1993), Analytical approximation for nonlinear adsorbing solute transport and first-order degradation, *Transp. Porous Media*, 11, 33-43.

Cirpka, O. A. (2002), Choice of dispersion coefficients in reactive transport calculations on smoothed fields, *J. Contam. Hydrol.*, 58, 261-282.

Cirpka, O. A., E. O. Frind, and R. Helmig (1999a), Numerical simulation of biodegradation controlled by transverse mixing, *J. Contam. Hydrol.*, 40, 159-182.

Cirpka, O. A., E. O. Frind, and R. Helmig (1999b), Streamline-oriented grid generation for transport modelling in two-dimensional domains including wells, *Adv. Water Resour.*, 22, 697-710.

Cirpka, O. A., and P. K. Kitanidis (2000a), An advective-dispersive stream tube approach for the transfer of conservative-tracer data to reactive transport, *Water Resour. Res.*, 36, 1209-1220.

Cirpka, O. A., and P. K. Kitanidis (2000b), Characterization of mixing and dilution in heterogeneous aquifers by means of local temporal moments, *Water Resour. Res.*, 36, 1121-1236.

Dagan, G. (1984), Solute transport in heterogeneous formations, *J. Fluid Mech.*, 145, 151-177.

Dagan, G. (1989), *Flow and transport in porous media*, Springer-Verlag, Berlin.

Dagan, G., and V. D. Cvetkovic (1996), Reactive transport and immiscible flow in geological media. I. General theory, *Proc. R. Soc. Lond. A*, 452, 285-301.

Dagan, G., V. D. Cvetkovic, and A. M. Shapiro (1992), A solute flux approach to transport in heterogeneous formations 1. The general framework, *Water Resour. Res.*, 28, 1369-1376.

Dagan, G., and A. Fiori (1997), The influence of pore-scale dispersion on concentration statistical moments in transport through heterogeneous aquifers, *Water Resour. Res.*, 33, 1595-1605.

Dentz, M., H. Kinzelbach, S. Attinger, and M. Kinzelbach (2000), Temporal behavior of a solute cloud in a heterogeneous porous medium 1. Point-like injection, *Water Resour. Res.*, 36, 3591-3604.

Fiori, A., S. Berglund, V. D. Cvetkovic, and G. Dagan (2002), A first-order analysis of solute flux statistics in aquifers: the combined effect of pore-scale dispersion, sampling, and linear sorption statistics, *Water Resour. Res.*, 38, doi:10.1029/2001WR000678.

Fiori, A., and G. Dagan (1999), Concentration fluctuations in transport by groundwater: comparison between theory and field experiments, *Water Resour. Res.*, 35, 105-112.

Fiori, A., and G. Dagan (2000), Concentration fluctuations in aquifer transport: a rigorous first-order solution and applications, *J. Contam. Hydrol.*, 45, 139-163.

Gelhar, L. W. (1986), Stochastic subsurface hydrology from theory to applications, *Water Resour. Res.*, 22, 135S-145S.

Gelhar, L. W., and C. L. Axness (1983), Three-dimensional stochastic analysis of macrodispersion in aquifers, *Water Resour. Res.*, 19, 161-180.

Ginn, T. R. (1998), Comment on "Stochastic analysis of oxygen-limited biodegradation in three-dimensionally heterogeneous aquifers" by F. Miralles-Wilhelm et al., *Water Resour. Res.*, 34, 2423-2426.

Ginn, T. R. (2001), Stochastic-convective transport with nonlinear reactions and mixing: finite streamtube ensemble formulation for multicomponent reaction systems with intra-streamtube dispersion, *J. Contam. Hydrol.*, 47, 1-28.

Ginn, T. R., C. S. Simmons, and B. D. Wood (1995), Stochastic-convective transport with nonlinear reaction: Biodegradation with microbial growth, *Water Resour. Res.*, 31, 2689-2700.

Kaluarachchi, J. J., V. D. Cvetkovic, and S. Berglund (2000), Stochastic analysis of oxygen- and nitrate-based biodegradation of hydrocarbons in aquifers, *J. Contam. Hydrol.*, 41, 335-365.

Kapoor, V., L. W. Gelhar, and F. Miralles-Wilhelm (1997), Bimolecular second-order reactions in spatially varying flows: Segregation induced scale-dependent transformation rates, *Water Resour. Res.*, 33, 527-536.

Kapoor, V., and P. K. Kitanidis (1998), Concentration fluctuations and dilution in aquifers, *Water Resour. Res.*, 30, 1181-1193.

Keijzer, H., R. J. Schotting, and S. E. A. T. M. van der Zee (2000), Semi-analytical traveling wave solution of one-dimensional aquifer bioremediation, *Communications on Applied Nonlinear Analysis*, 7, 1-20.

Keijzer, H., M. I. J. van Dijke, and S. E. A. T. M. van der Zee (1999), Analytical approximation to characterize the performance of in-situ aquifer bioremediation, *Adv. Water Resour.*, 23, 217-228.

Miralles-Wilhelm, F., L. W. Gelhar, and V. Kapoor (1997), Stochastic analysis of oxygen-limited biodegradation in three-dimensionally heterogeneous aquifers, *Water Resour. Res.*, 33, 1251-1263.

Miralles-Wilhelm, F., L. W. Gelhar, and V. Kapoor (1998), Reply, *Water Resour. Res.*, 34, 2427-2429.

Oya, S., and A. J. Valocchi (1997), Characterization of traveling waves and analytical estimation of pollutant removal in one-dimensional subsurface bioremediation modeling, *Water Resour. Res.*, 33, 1117-1127.

Oya, S., and A. J. Valocchi (1998), Transport and biodegradation of solutes in stratified aquifers under enhanced in situ bioremediation conditions, *Water Resour. Res.*, 34, 3323-3334.

Rao, P. V., K. M. Portier, and P. S. C. Rao (1981), A stochastic approach for describing convective-dispersive solute transport in saturated porous media, *Water Resour. Res.*, 17, 963-968.

van Duijn, C. J., and P. Knabner (1992), Travelling Waves in the Transport of Reactive Solutes through Porous Media: Adsorption and Ion Exchange - Part 1, *Transp. Porous Media*, 8, 167-194.

Vanderborght, J., and H. Vereecken (2002), Estimation of local scale dispersion from local breakthrough curves during a tracer test in a heterogeneous aquifer: the Lagrangian approach, *J. Contam. Hydrol.*, 54, 141-171.

Xin, J., and D. Zhang (1998), Stochastic analysis of biodegradation fronts in one-dimensional heterogeneous porous media, *Adv. Water Resour.*, 22, 103-116.

Zhang, D. (2002), *Stochastic methods for flow in porous media: coping with uncertainties*, Academic Press, San Diego.

CHAPTER

3

Measurement network design including travel time determinations to minimize model prediction uncertainty

Published in *Water Resources Research*, **2008**

[Janssen, G.M.C.M., J.R. Valstar, and S.E.A.T.M. van der Zee (2008), Measurement network design including travel time determinations to minimize model prediction uncertainty, *Water Resour. Res.*, *44*, W02405, doi:10.1029/2006WR005462.]

Presented at the *XVI International Conference on Computational Methods in Water Resources*, Copenhagen, Denmark, **2006**

[Janssen, G.M.C.M., J.R. Valstar, and S.E.A.T.M. van der Zee (2008), Measurement network design including groundwater age observations. In: Proceedings of XVI International Conference on Computational Methods in Water Resources, Copenhagen, June 19-22, 2006.]

3.1. Introduction

Measurement network design or data worth analysis, whether done manually or using more or less sophisticated mathematical guidelines, is an inherent part of any soil and groundwater investigation, as it naturally evolves from the measurement campaign's purpose: obtaining the necessary information given the limited resources. Accordingly, this field of research receives constant attention in the literature. Nowadays, the literature offers a wide range of design strategies for a large number of applications, which roughly can be divided into five categories: 1) maximizing the likelihood of plume detection [*Massman and Freeze*, 1987a, b; *Meyer and Brill*, 1988; *Meyer et al.*, 1994; *Storck et al.*, 1997]; 2) minimizing the uncertainty in groundwater quality [*Loaiciga*, 1989; *Herrera et al.*, 2000; *Nunes et al.*, 2004; *Wu et al.*, 2005]; 3) model calibration for minimizing the uncertainty in model predictions [*McKinney and Loucks*, 1992; *Wagner*, 1995; *Tiedeman et al.*, 2003; *Tiedeman et al.*, 2004]; 4) optimizing groundwater and remediation management [*James and Gorelick*, 1994; *Wagner*, 1999; *Feyen and Gorelick*, 2005]; 5) model calibration for minimizing model parameter uncertainty [*Hughes and Lettenmaier*, 1981; *Bogardi et al.*, 1985; *Knopman and Voss*, 1989; *Knopman et al.*, 1991; *Sumner et al.*, 1997; *Pardo-Iguzquiza*, 1998; *Chang et al.*, 2005]. The last application hardly ever is a purpose on its own but is usually conducted in order to improve model prediction reliability, which in turn can potentially lead to the design of groundwater and remediation management strategies that are more cost-effective [*James and Gorelick*, 1994; *Wagner*, 1999; *Feyen and Gorelick*, 2005].

The design strategies reported in the literature generally seek the optimal placement and/or sampling times for measurements of heads, concentrations, parameters, or a combination of these three. In the past two decades, however, travel time determinations have found increasing application as another type of information with which flow models can be constrained. By travel time determinations we mean both groundwater age estimations and tracer arrival time measurements. Groundwater ages can be derived from concentrations of environmental tracers, such as $^{3}H/^{3}He$ (e.g. *Smethie Jr et al.* [1992]), ^{85}Kr (e.g. *Solomon et al.* [1992]), chlorofluorocarbons (e.g. [*Dunkle et al.*, 1993]), or a combination of them (e.g. *Ekwurzel et al.* [1994], *Reilly et al.* [1994] and *Szabo et al.* [1996]). By tracer arrival times we mean the advective (mean) arrival times that are obtained in field experiments using conservative tracers (e.g.

Anderman and Hill [2001]). When accurate, travel time determinations can be more informative than head and conductivity measurements, as the sensitivity of heads to parameters is usually limited and the spatial correlation range between travel time and conductivity is often larger than the correlation range of the conductivity itself [*Harvey and Gorelick*, 1995; *Sheets et al.*, 1998; *Stute and Schlosser*, 2000].

Manual calibration of flow models using tracer derived groundwater ages has been performed by, for example, *Reilly et al.* [1994], *Sheets et al.*, [1998] and *Izbicki et al.* [2004]. Systematic, mathematical approaches to parameter inference from age data or data on tracer arrival time are given by *Harvey and Gorelick* [1995], *Portniaguine and Solomon* [1998], *Woodbury and Rubin*, [2000], *Cirpka and Kitanidis* [2001], and *Feyen et al.* [2003]. However, travel time determinations have never been incorporated in the design of optimal measurement strategies. The purpose of the present study is therefore to propose an algorithm that optimally configures measurement networks including age or tracer arrival time determinations.

We will focus our network design on minimizing contaminant breakthrough prediction uncertainty, thus making a contribution to the 3rd network design application category mentioned above. Aiming a measurement campaign at reducing prediction uncertainty makes sense, as "*it is rarely feasible to improve the representation of all aspects of a simulated system. Thus it is of interest to identify the particular attributes of a flow system that are most important to the relevant predictions, and to focus field characterization on these attributes*" [*Tiedeman et al.*, 2003]. Yet, this category has received little attention in the literature. If we narrow down our search further to those studies that take correlations between measurements into account, then the state-of-the-art is typified by the contributions of *Wagner* [1995], *Tiedeman et al.* [2003], *Tiedeman et al.* [2004] and *Hendricks-Franssen and Stauffer* [2005]. The first three of these contributions all used the first-order linear statistical inference method [*Dettinger and Wilson*, 1981] to infer the prediction covariance matrix from sensitivity matrices and the posterior parameter covariance matrix. They recalculated the posterior parameter covariance matrix in every network evaluation that is performed, which in their approaches requires repeated inversion of a squared estimation Jacobian, i.e. the matrix of state measurement sensitivities. This can become computationally demanding if the number of unknown parameters is large, for example in case of a highly discretized

hydraulic conductivity field. *Hendricks Franssen and Stauffer* [2005] circumvented the recalculation of the parameter covariance matrix for every design by explicitly calculating the (cross-)covariances between parameters and states using a Monte Carlo approach and solving a cokriging system to determine the variance reduction for every candidate network.

Here, we will use an adjusted version of the representer-based inverse method [*Valstar*, 2001; *Valstar et al.*, 2004], a Bayesian algorithm which can efficiently calculate the linearized covariances between measurements and predictions, and between the measurements themselves. This circumvents time-consuming Monte Carlo analyses. On the basis of the thus approximated covariances, the posterior covariances of the states and predictions can be estimated for every possible measurement set, without having to recalculate the posterior parameter covariance matrix.

The purpose of the proposed method is to provide insight in where in the flow field travel time information would be most valuable for the reduction of prediction uncertainty. A presupposition of the proposed method is that the travel times can be derived with a reasonable and quantifiable reliability from field measurements. As will be discussed in Section 3.5, for groundwater age this is a very challenging issue in itself, but how to do that is out of the scope of this chapter.

In the next Section, we will discuss the concepts and the mathematical development of our first-order design method. The method will be illustrated with a numerical, synthetic example, the details and results of which are given in Section 3.3 and 3.4, respectively. Conclusions and a discussion on some aspects of the method follow in Section 3.5.

3.2. Theory

As we feel that the method is better explained by focusing it directly on a tangible illustrative example, first a hypothetical problem statement is introduced. Subsequently, an outline of the first-order design method is given, followed by a presentation on how we arrive at the necessary prior and posterior covariances in the applied Bayesian framework.

3.2.1. Problem Statement

The illustrative example with which the design method will be explained is schematized in Figure 1. It represents a two-dimensional cross-section of a confining layer (y_2-y_3) that protects Aquifer 2 (y_3-y_4) from a conservative contaminant released out of a source zone (x_7-x_8) at the top of Aquifer 1 (y_1-y_2). The control plane at which breakthrough is evaluated is located at y_3 along the bottom of the area of interest (x_6-x_9, y_2-y_3).

All parameters and dimensions in the example problem are assumed constant and known, except for the hydraulic conductivity (K) in the shaded center part (x_5-x_{10},y_2-y_3) of the confining layer, the natural logarithm of which is assumed to be Gaussian distributed with known mean and variogram functions. A full description of the system's quantitative properties will follow in Section 3.3 where the system visualized in Figure 1 is used in the example calculations.

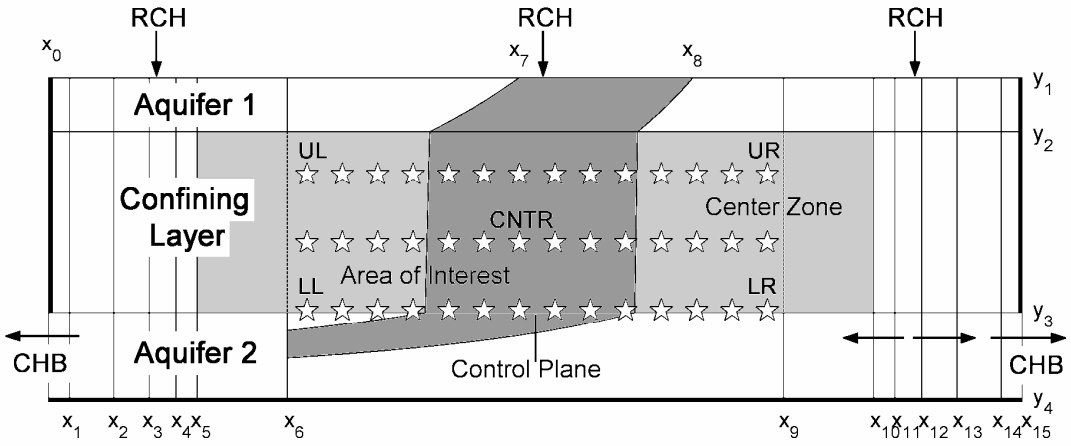

Figure 1. Schematic overview of the numerical grid used in the calculations, showing the prior contaminant flow (in dark grey). RCH = recharge. CHB = constant head boundary. x_0 = 0m, x_1 = 2.0m, x_2 = 2502.0m, x_3 = 2752.0m, x_4 = 2777.0m, x_5 = 2779.5m, x_6 = 2879.5m, x_7 = 3009.5m, x_8 = 3109.5m, x_9 = 3159.5m, x_{10} = 3259.5m, x_{11} = 3262.0m, x_{12} = 3287.0m, x_{13} = 3537.0m, x_{14} = 6037.0m, x_{15} = 6039.0m. y_1 = 0m, y_2 = -2.0m, y_3 = -22.0m, y_4 = -32.0m. Bold lines indicate no-flow boundaries. Potential measurement locations labeled UR, UL, LR, LL and CNTR are the locations where the head variances are evaluated in Figure 4. Arrows indicate flow directions.

A steady-state head distribution is obtained by assigning recharge on top of Aquifer 1 and by imposing constant head boundaries in Aquifer 2. Except for the upper boundary and the left and right boundaries of Aquifer 2, all boundaries are closed. For illustration, Figure 1 also shows the contaminant plume that spreads from the contaminant source zone when the confining layer is modeled as a homogeneous medium with K set to its geometric mean (see Section 3.3) and the boundary conditions are imposed as in the computational examples (Section 3.3).

The question underlying the theoretical development given in the remainder of this Section is how to optimally choose between age, head and conductivity measurements and how to optimally distribute them over the potential sampling locations, indicated by the stars in Figure 1.

3.2.2. Outline of the first-order design method

If the control plane over which the breakthrough is predicted receives a significant inflow that does not originate from the contaminant source zone, as is the case in Figure 1, the contaminant breakthrough time probability distribution $p(\tau_{BT})$ is a function of the travel time probability of the entire inflow and the contaminant breakthrough location probability:

$$p(\tau_{BT}) = p(t_0 + \tau) = \int_{x^{CP}=A}^{x^{CP}=B} p(\tau; x^{CP}) p(x^{CP} \in \chi) dx^{CP} \tag{1}$$

or in discretized form:

$$p(\tau_{BT}) \approx \sum_{x^{CP}=A}^{x^{CP}=B} \frac{1}{2} \left[p(\tau; x^{CP}) p(x^{CP} \in \chi) + p(\tau; x^{CP} + \Delta x^{CP}) p(x^{CP} + \Delta x^{CP} \in \chi) \right] \Delta x^{CP} \tag{2}$$

In equations (1-2), τ_{BT} is the contaminant breakthrough time evaluated at the control plane, t_0 is the starting time of the contamination, τ is arrival time (or groundwater age at the control plane), $p(\tau;x^{CP})$ is the marginal arrival time probability evaluated at x^{CP}, x^{CP} is a location at the control plane, $p(x^{CP} \in \chi)$ is the probability that x^{CP} belongs to the

contaminant breakthrough zone χ (χ is the collection of all breakthrough locations χ), and *A* and *B* are the spatial x limits of the control plane (x_6 and x_9 in Figure 1). Δx^{CP} is the discretization interval along the control plane.

Assuming that τ and χ are Gaussian distributed, we have

$$p\left(\tau; x^{CP}\right) \approx N\left(\tau; \sigma^2_{\tau\left(x^{CP}\right)}, \mu_{\tau\left(x^{CP}\right)}\right) \tag{3}$$

$$p\left(x^{CP} \in \chi\right) \approx \sum_{x^{SZ}=C}^{x^{SZ}=D} \frac{1}{2}\left[N\left(x^{CP}; \sigma^2_{\chi\left(x^{SZ}\right)}, \mu_{\chi\left(x^{SZ}\right)}\right) + N\left(x^{CP}; \sigma^2_{\chi\left(x^{SZ}+\Delta x^{SZ}\right)}, \mu_{\chi\left(x^{SZ}+\Delta x^{SZ}\right)}\right)\right]\Delta x^{SZ}, \tag{4}$$

where $N(p_1;p_2,p_3)$ represents the probability density of p_1 according to the normal distribution, parameterized with variance p_2 and mean p_3, $\tau(x^{CP})$ is the arrival time of a particle arriving at the control plane at location x^{CP}, $\sigma^2_{\tau\left(x^{CP}\right)}$ is the arrival time (or age) variance at x^{CP}, and $\mu_{\tau\left(x^{CP}\right)}$ is the mean arrival time (or age) at x^{CP}. $\chi\left(x^{SZ}\right)$ is the breakthrough location of a particle that originated from x^{SZ}, where x^{SZ} is a location in the contaminant source zone. $\sigma^2_{\chi\left(x^{SZ}\right)}$ and $\mu_{\chi\left(x^{SZ}\right)}$ are the breakthrough location variance and mean (along the x-axis) of a particle originating from x^{SZ}, respectively, Δx^{SZ} is the discretization interval along the contaminant source zone, and *C* and *D* are the spatial x limits of the contaminant source zone (x_7 and x_8 in Figure 1).

Finally, the variance of the breakthrough time $\sigma^2_{\tau_{BT}}$ can be calculated as:

$$\sigma^2_{\tau_{BT}} = \frac{\int_{\tau_{BT}=0}^{\infty} \left(\tau_{BT} - E\left(\tau_{BT}\right)\right)^2 p\left(\tau_{BT}\right) dt}{\int_{\tau_{BT}=0}^{\infty} p\left(\tau_{BT}\right) dt} \quad \text{with} \quad E\left(\tau_{BT}\right) = \frac{\int_{\tau_{BT}=0}^{\infty} \tau_{BT}\, p\left(\tau_{BT}\right) dt}{\int_{\tau_{BT}=0}^{\infty} p\left(\tau_{BT}\right) dt}, \tag{5}$$

where $E\left(\tau_{BT}\right)$ is the expected contaminant breakthrough time. Equation (5) is the objective function to be minimized in the search for an optimal network design.

From equations (1-5) it follows that to evaluate the performance of different measurement network designs, the influences of the observable variables at their potential sampling locations on the prediction of the breakthrough time $\tau\left(x^{CP}\right)$ and the

breakthrough locations $\chi(x^{SZ})$ have to be known. This makes $\tau(x^{CP})$ and $\chi(x^{SZ})$ our goal variables and they will be called as such throughout the remainder of this chapter.

The recently proposed representer-based inverse method [*Valstar et al.*, 2004] provides an efficient way to calculate these influences. The representers calculated in this method are equivalent to the linearized covariances between the observable variable at the potential sampling location and the variables for which the representers are defined. As such, they provide a first-order estimation of the prior covariances of the observable variables and the goal variables $\tau(x^{CP})$ and $\chi(x^{SZ})$. These covariances can subsequently be used to approximate the posterior covariances of the goal variables, and therefore the posterior breakthrough time uncertainty, before the measurements are actually taken.

Thus, the presented algorithm can efficiently calculate, at first order, the expected posterior breakthrough time variance $\sigma^2_{\tau_{BT}}$ (equation (5)) of the contaminant for every candidate measurement network design. A Genetic Algorithm was used to efficiently search for a near-optimal design that minimizes $\sigma^2_{\tau_{BT}}$. For clarification, a flow chart of the design method is given in Figure 2.

3.2.3. Bayesian Framework: derivation of Ln(breakthrough time) and breakthrough location representers

The covariances between the breakthrough location $\chi(x^{SZ})$ and any observation are given at first order by breakthrough location representers. The covariances between the breakthrough times $\tau(x^{CP})$ and any observation, as well as the covariance between groundwater ages and any other measurement, are given at first order by travel time representers. In this work, the derivation of the travel time representers will be carried out for lognormally distributed travel times, because unless the travel time is evaluated in the large displacement regime[3], the travel time probability density function will, in general, show a significant skewness. In the literature, therefore, skewed distributions are often adopted for the travel time, such as the lognormal (e.g. [*Simmons*, 1982; *Cvetkovic et al.*, 1992; *Kovar et al.*, 2005] or the inverse-Gaussian (e.g. [*Cirpka and*

[3] By virtue of the Central Limit Theorem (e.g. [*Zhang*, 2002], p. 61), after many correlation distances the Gaussian assumption might be valid.

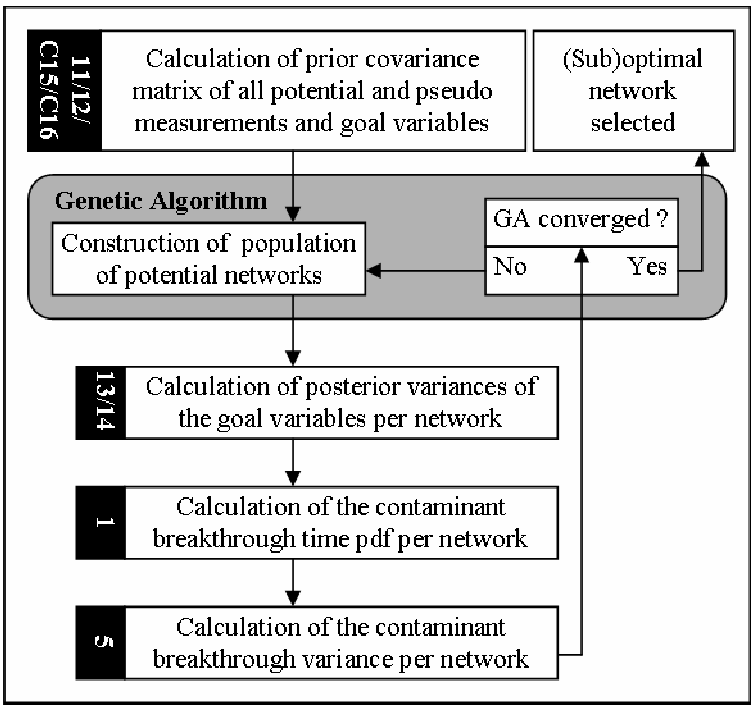

Figure 2. Flow chart of the proposed network design algorithm. The numbers in the black boxes refer to the equations using which the actions described in the text boxes attached to them are performed. GA = Genetic Algorithm.

Kitanidis, 2000]) distribution. Here, because of the analytical simplicity of logarithmic transformations, we will treat the travel time as a lognormally distributed variable, transform travel time estimations to the Gaussian distribution by taking their natural logarithm to make them comply with the Bayesian framework of the representer-based inverse algorithm, and derive Ln(travel time) representers accordingly.

Consider the flow, the particle travel time, and the particle location equations:

$$\phi_1 = A_{fg}(\alpha)h_g - q_f = 0 \tag{6}$$

$$\phi^s_{2_i} = 0 = t^s_i - t^{s-1}_i - \Delta t^s_i\left(\alpha, h, x^s_i, x^{s-1}_i, y^s_i, y^{s-1}_i\right) \tag{7}$$

$$\phi^s_{3_i} = 0 = \begin{cases} x^s_i - x^{s-1}_i - \Delta x^s_i\left(\alpha, h, y^s_i, y^{s-1}_i\right) & \text{for } x^s_i \neq x_{cell\ boundary} \\ x^s_i - x_{cell\ boundary} & \text{for } x^s_i = x_{cell\ boundary} \end{cases} \tag{8}$$

$$\phi^s_{4_i} = 0 = \begin{cases} y^s_i - y^{s-1}_i - \Delta y^s_i\left(\alpha, h, x^s_i, x^{s-1}_i\right) & \text{for } y^s_i \neq y_{cell\ boundary} \\ y^s_i - y_{cell\ boundary} & \text{for } y^s_i = y_{cell\ boundary} \end{cases} \tag{9}$$

Table 1. Ranges of indicators and indices

Index	**ranges from 1 to the number of:**
i	tracked particles, which equals the number of potential age determinations plus the number of pseudo breakthrough time and pseudo breakthrough location measurements.
f,g	head state variables.
k,l	uncertain parameters.
n,p,q	measurements.

In these and following equations, subscripted indices show vector and matrix dimensions and how, where applicable, matrix-vector multiplications should be performed. Products of terms containing the same index twice should be summed over that index. The ranges of all indices used are given in Table 1. Furthermore, in equations (6-9), *h* is the vector of nodal heads, *q* is the vector of driving forces, and $A(\alpha)$ is the system matrix depending on the unknown parameters α (=Ln(*K*)), t_i is the travel time of particle *i*, Δt_i^s is the duration of travel step *s*, x_i and y_i are the locations along respectively the x- and y-axis of particle *i*, and Δx_i^s and Δy_i^s are the distances traveled along respectively the x- and y-axis by particle *i* during travel step *s*. For this study we applied a numerical particle tracking scheme in which travel step sizes are limited by reaching cell boundaries rather than by reaching set time step sizes. In this case, Δt_i^s and Δy_i^s depend on x_i^s and x_i^{s-1} if travel step *s* is limited by reaching an x-boundary of a cell. Furthermore, Δt_i^s and Δx_i^s depend on y_i^s and y_i^{s-1} if travel step *s* is limited by reaching a y-boundary of a cell.

The representer-based inverse method searches for the maximum a posteriori estimates of the parameters, given the measurements. In this chapter, the measurements that are taken into account are head (*h*), conductivity (*K*), groundwater age (*t*), and particle breakthrough location (χ) measurements. As will be explained in Section 3.4, χ measurements will be incorporated in the algorithm as pseudo observations only, to enable the calculation of cross covariances between the goal variable $\chi\left(x^{SZ}\right)$ and the other measurement types.

For a steady-state system, if all parameters α and measurement errors v are assumed to be multivariate Gaussian distributed with known covariances and they are not cross-correlated, the maximum a posteriori estimates of the parameters can be found by minimizing the following objective function:

$$J = [\alpha - \bar{\alpha}]^T \left[P_\alpha^{-1}\right][\alpha - \bar{\alpha}] + [z - M(h, \alpha, \mathrm{Ln}(t), \chi)]^T \left[P_v^{-1}\right][z - M(h, \alpha, \mathrm{Ln}(t), \chi)], \quad (10)$$

where J is the objective function value, z is the vector of measurement values, $M(\ )$ is a linear function that interpolates the vector of model predictions at the nodal points to the locations of the measurements, $\bar{\alpha}$ is the prior mean of the parameters, P_v is the covariance matrix of the measurement errors v, and P_α is the prior covariance matrix of the parameters. By the Lagrange Method, we expand the objective function as:

$$J^* = J + 2\lambda_h[\phi_1 - q_f] + \sum_i^{N_i}\sum_s^{N_{s_i}}\left[2\lambda_{t_i}^s(\phi_{2_i}^s)\right] + \sum_i^{N_i}\sum_s^{N_{s_i}}\left[2\lambda_{x_i}^s(\phi_{3_i}^s)\right] + \sum_i^{N_i}\sum_s^{N_{s_i}}\left[2\lambda_{y_i}^s(\phi_{4_i}^s)\right], \quad (11)$$

where N_i is the number of tracked particles, N_{s_i} is the total number of steps traveled by particle i, λ_h is the head adjoint vector, λ_t is the travel time adjoint vector, and λ_x and λ_y are the x and y location adjoint vector, respectively. In the minimum of objective function J^*, the variation of J^* is zero for any variation of α, h, x, y, t, λ_h, λ_x, λ_y and λ_t. Forcing this condition on equation (11) yields a system of 9 coupled Euler-Lagrange equations (see Appendix A). The solution of the system of Euler-Lagrange equations gives the set of parameters at which the derivatives of the extended objective function (equation (11)) with respect to the parameters are zero. Assuming that equation (11) has only 1 global minimum and no local minima, this is the set of parameters that optimally obeys the observations given the prior information.

The nonlinear system of Euler-Lagrange equations is solved by first linearizing its individual equations. Then, the unknowns are expanded into a finite number of representer terms, each of which represents the influence of one particular measurement on the unknown, see Appendix B. Subsequently, the representer expressions and the unknowns are updated iteratively. The representer expansions enable the decoupling of the Euler-Lagrange equations into a set of expressions for the

representers and their coefficients that can be sequentially solved (see Appendix C). In our first-order network design approach, the inverse algorithm is terminated in the first iteration after the Ln(τ) representers and the breakthrough location representers have been obtained. Updating the unknowns in preparation for the second iteration and further requires measurement information, which is assumed to be unavailable at this stage of the network design.

From Appendices C9 and C7 it follows that after the first iteration the Ln(τ) representer (Θ^*) for a particle *i* is given by:

$$\Theta_i^{*N_{si}} = \frac{1}{t_i^{N_{si}}}\left[\sum_{s=N_{si}}^{1}\frac{\partial \Delta t_i^s}{\partial \alpha_l}\Psi_l + \sum_{s=N_{si}}^{1}\frac{\partial \Delta t_i^s}{\partial h_g}\Xi_g + \sum_{s=N_{si}}^{1}\frac{\partial \Delta t_i^s}{\partial x_i^s}\mathrm{X}_i^s + \sum_{s=N_{si}}^{1}\frac{\partial \Delta t_i^s}{\partial x_i^{s+1}}\mathrm{X}_i^{s+1} + \sum_{s=N_{si}}^{1}\frac{\partial \Delta t_i^s}{\partial y_i^s}\mathrm{Y}_i^s + \sum_{s=N_{si}}^{1}\frac{\partial \Delta t_i^s}{\partial y_i^{s+1}}\mathrm{Y}_i^{s+1}\right], \quad (12)$$

with terminal conditions $\mathrm{X}_i^{N_s+1}=0$ and $\mathrm{Y}_i^{N_s+1}=0$, and the breakthrough location representer is given by:

$$\mathrm{X}_i^{N_{si}} = \sum_{s=1}^{N_{si}}\frac{\partial \Delta x_i^s}{\partial \alpha_l}\Psi_l + \sum_{s=1}^{N_{si}}\frac{\partial \Delta x_i^s}{\partial h_g}\Xi_g + \sum_{s=1}^{N_{si}}\frac{\partial \Delta x_i^s}{\partial y_i^s}\mathrm{Y}_i^s + \sum_{s=1}^{N_{si}}\frac{\partial \Delta x_i^s}{\partial y_i^{s-1}}\mathrm{Y}_i^{s-1}, \quad (13)$$

with boundary conditions $\mathrm{Y}_i^0=0$. In equations (12) and (13), Ψ is the parameter representer (see Appendices B and C5), Ξ is the head representer (see Appendix B and C6), and $t_i^{N_{si}}$ is the breakthrough time of particle *i*. Equation (12) is in backward notation, because particles defined to calculate breakthrough time representers are tracked backward from the locations at the control plane where breakthrough time uncertainty information is desired.

3.2.4. Computation of posterior breakthrough time probability

The first-order posterior variances of the goal variables can now be calculated as:

$$P_{\mathrm{Ln}(\tau_i)}^{posterior} = P_{\mathrm{Ln}(\tau_i)}^{prior} - \Theta_{ip}^{*N_{si}} \left(\left(M\left(\Xi, \Psi, \Theta^*, \mathrm{X}\right) + P_v \right)^{-1} \right)_{pq} \Theta_{qi}^{*N_{si}} \quad (14)$$

$$P_{\chi_i}^{posterior} = P_{\chi_i}^{prior} - \mathrm{X}_{ip}^{N_{si}} \left(\left(M\left(\Xi, \Psi, \Theta^*, \mathrm{X}\right) + P_v \right)^{-1} \right)_{pq} \mathrm{X}_{qi}^{N_{si}} , \quad (15)$$

where $M\left(\Xi, \Psi, \Theta^*, \mathrm{X}\right)_{pq}$ is a $p \times q$ representer matrix that contains the prior cross covariances between all observations, $P_{\mathrm{Ln}(\tau_i)}^{prior}$ is calculated by defining a pseudo measurement of τ_i and calculating the Ln(τ) representer for this measurement, and $P_{\chi_i}^{prior}$ is calculated by defining a pseudo measurement for χ_i and calculating the breakthrough location representer for this measurement.

$P_{\mathrm{Ln}(\tau_i)}^{posterior}$ and $P_{\chi_i}^{posterior}$ can subsequently be filled in for $\sigma^2_{\tau(x^{CP})}$ and $\sigma^2_{\chi(x^{SZ})}$ in equations (3) and (4), respectively (note that τ in equations (1-3) is replaced by its natural logarithm). $\mu_{\tau(x^{CP})}$ and $\mu_{\chi(x^{SZ})}$ in equations (3) and (4) are approximated by their first guess estimates, Ln($\tau_F(x^{CP})$) and $\chi_F(x^{SZ})$ (see also Appendix B), obtained by running a simulation with α = $\overline{\alpha}$. Now all necessary information is available to compute $p(\tau_{BT})$ according to equation (2) and subsequently the variance of the breakthrough time $\sigma^2_{\tau_{BT}}$ according to equation (5).

Note that although many network evaluations are performed in the Genetic Algorithm, this repeated evaluation requires calculating the representer matrix $M\left(\Xi, \Psi, \Theta^*, \mathrm{X}\right)$ (for all potential measurements and pseudo measurements) only once. With $M\left(\Xi, \Psi, \Theta^*, \mathrm{X}\right)$ known, $P_{\mathrm{Ln}(\tau_i)}^{posterior}$ and $P_{\chi_i}^{posterior}$ can be calculated for every candidate network by selecting the relevant variances and covariances from this matrix and performing the necessary operations with them according to equations (14-15).

3.3. Numerical Application to a Synthetic Test Case

We will now demonstrate the design methodology by numerically filling in the problem that was introduced in Section 3.2.1 and Figure 1 and performing example calculations with the thus created test case.

Additional to the discretization of the flow model as shown in Figure 1, the area between x_5 and x_{10} is discretized into 240 equally sized (Δx = 2.0 m) columns, and additionally the confining layer (y_2-y_3) is discretized into 40 equally sized rows (Δy = 0.5 m). The purpose

of all areas outside the area of interest is solely to reduce the impact of boundary conditions on the flow in the area of interest.

The porosity is 0.4 everywhere, and Aquifer 1 and Aquifer 2 have a hydraulic conductivity (K) of 3.0 and 0.6 m/d, respectively. The Gaussian distribution of Ln(K) (= Y) in the center part of the confining layer (9,600 cells) has a geometric mean Ln(K_G) of -3.0 Ln(m/d), a variance σ_Y^2 of 2.0 unless stated otherwise, and an exponential variogram model with horizontal and vertical correlation ranges of 75 m and 25 m, respectively. Outside the shaded center part (x_0-x_5 and x_{10}-x_{13}) the confining layer is modeled as a homogeneous deposit with K equal to the K_G assigned to the center part. A steady-state head distribution is obtained by assigning recharge (250 mm/year) to the top of all cells of Aquifer 1 and by imposing a constant head of 0.0 m and 15.0 m in the utmost left and utmost right cell of Aquifer 2, respectively. This resulted in a flow divide between x_{13} and x_{14}, as indicated by the arrows in Figure 1.

The stars in the area of interest indicate 42 potential measurement locations. All h and K measurements were assumed to be virtually error free with Gaussian distributed error variances of 0.0001 m^2 and 0.001 $(m/d)^2$, respectively. This in no way implies compromised generality of the method, as larger error variances could have been chosen just as well. The reason for the choice for small error variances will become clear later.

For t determinations, the estimation error standard deviation is taken as a percentage of the expected (untransformed) age (t_F) at the sampled location in the prior realization of the confining layer, in which all stochastic parameters are set at their prior means ($\alpha = \mathrm{Ln}(K) = \overline{\alpha}$ = -3.0 Ln(m/d)). This percentage varies between different examples.

At the control plane, in every column one pseudo age determination was defined to enable the calculation of the covariances between the goal variable Ln($\tau(x^{CP})$) and the measurements in a design. The sensitivity terms in equation (12) (the Ln(τ) representer equation) were computed by backward tracking of particles traveling from the pseudo measurement locations at the control plane to the inflow zone (y = y_1) and calculating the time step sensitivities of every travel step using the ADV2 package of MODFLOW 2000 [*Anderman and Hill*, 2001].

Likewise, in the contaminant source zone, one pseudo location measurement was defined in every column, to enable the calculation of the covariances between the goal

variable $\chi(x^{SZ})$ and the measurements in a design. The terms in the breakthrough location (χ) representer equation (13) were computed by forward tracking of particles traveling from the pseudo measurement location in the contaminant source zone to the control plane and evaluating the displacement sensitivities of every travel step, again using the ADV2 package of MODFLOW 2000.

In the example calculations, the desired number of measurements in the resulting designs was always fixed, although during the optimization it was allowed to vary. This was achieved by adding an extra term to the objective function (equation (5)) in the Genetic Algorithm. This term consisted of a multiplication of the absolute value of the squared difference between the required number of measurements and the actual number of measurements in the design under consideration, and a multiplication coefficient. This multiplication coefficient was chosen differently in every design optimization, as it affects the convergence of the Genetic Algorithm.

3.4. Results

In this Section, we will first investigate the validity of the first-order Bayesian methodology by checking the normality of Ln(t), and by comparing linearized variance predictions as given by the representer method with Monte Carlo results for increasing parameter variability. The Monte Carlo simulations were performed using MODFLOW [*McDonald and Harbaugh*, 1984] in combination with the particle-tracking software MODPATH [*Pollock*, 1994]. The number of Monte Carlo runs was 10000 for every calculation.

Subsequently, we will take a look at the correlations between the observable variables and the goal variables. Knowing and understanding these correlations is useful to explain the observation networks as designed by the first-order method. The details of the procedure followed for the calculation of the correlations will be given in Section 3.4.2. In Section 3.4.3, three examples of near-optimal network designs will be given and explained on the basis of the calculated correlations.

Finally, in Section 3.4.4, we will compare the performance of networks consisting solely of age determinations with the performance of networks consisting solely of head and solely of conductivity measurements.

3.4.1. Validity of the first-order design method

As our inverse method is defined in a Bayesian framework, it is important that all unknown parameters and dependent variables are (at least approximately) Gaussian distributed. It is well known that if Y is Gaussian distributed, at first order so are the hydraulic head and the particle displacement [*Dagan*, 1989]. Particle travel times, however, can be significantly skewed if the traveled number of correlation scales is limited (see Section 3.2.3). Fortunately, in our example, the natural logarithm of arrival time is approximately Gaussian if σ_Y^2 is not too large. This is shown in Figure 3, which gives the histogram of breakthrough times for a particle starting from the middle of the contaminant source zone. Also indicated in this figure is the Gaussian probability density function (pdf) parameterized with the mean and variance of breakthrough times calculated from the Monte Carlo results. The good correspondence of the Monte Carlo-derived Ln(τ) histogram with the Gaussian distribution will deteriorate as σ_Y^2 gets larger and the untransformed travel times become more skewed. However, for the range of σ_Y^2 values for which the linear theory applied here can be assumed valid (see below) the natural logarithm of the travel time can be considered as a sufficiently Gaussian distributed variable.

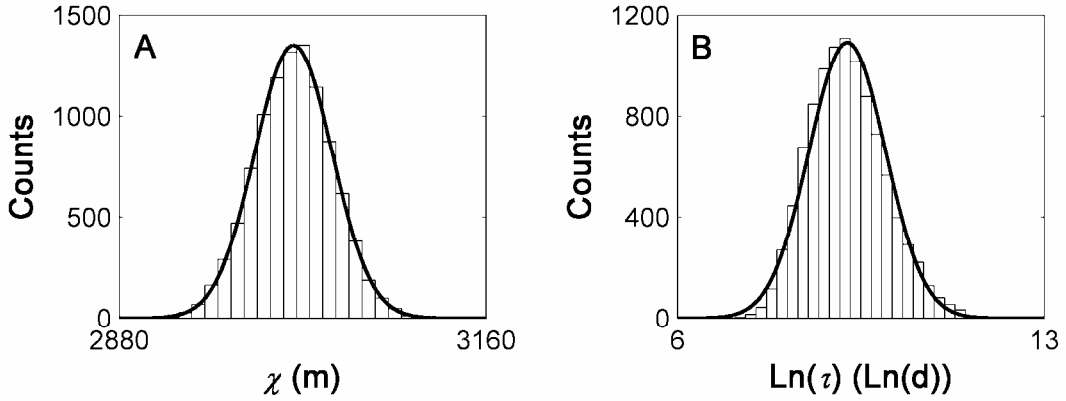

Figure 3. Histograms of the distribution of breakthrough locations (A) and breakthrough times (B) for the Monte Carlo simulation of a particle starting from the center of the contaminant source zone, compared with the theoretical normal probability density function using the Monte Carlo derived means and variances (black lines). $\sigma_Y^2 = 2.0$.

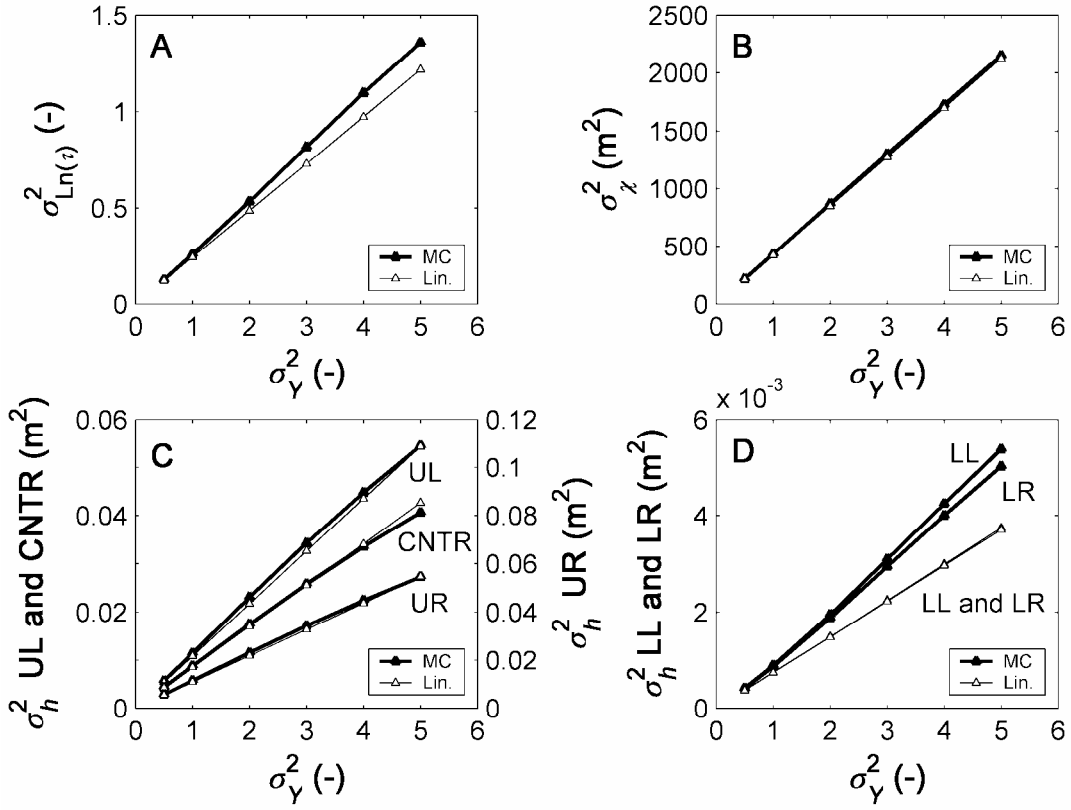

Figure 4. Linearized Ln(τ) (A), χ (B) and h (C and D) variance predictions as given by the representer approach compared with variances obtained from a Monte Carlo series, as function of σ_Y^2. In (C) and (D), the labels UL, LL, UR, LR and CNTR correspond with the labels in Figure 1 and identify the locations in the domain at which the variances were evaluated.

Figure 4 addresses the question regarding the applicability of the linear theory for larger σ_Y^2. Figure 4 compares the variances of the state variables as calculated by the representer approach with the variances of these variables computed with a Monte Carlo approach. Figure 4a shows the results for Ln(τ) of a particle originating from the center of the contaminant source zone. It should be noted here that the observed underestimation of the variances by the first-order method is caused by two distinct factors: increasing non-linearity of the flow equation and increasing non-normality of Ln(τ) as σ_Y^2 increases. Still, up to σ_Y^2 = 3.0 the difference between linearization and Monte Carlo results is less than 10%.

Figure 4b compares Monte Carlo variances with linearized variances of the particle breakthrough location χ. The correspondence is excellent for the entire range investigated. The same holds for the head variance in the upper part of the domain (Figure 4c). Only for the head variance in the lower part, the correspondence between the first-order results and the Monte Carlo results deteriorates rather quickly as σ_Y^2 increases. It is conceivable that the larger influence of the constant head boundaries in this part of the domain increases the nonlinearity of the flow equation. Nevertheless, considering the small absolute value of the underestimation of the head variance (note the factor 10 difference between the y-axes of Figures 4c and 4d), the error made is not expected to significantly influence contaminant breakthrough time uncertainty predictions.

Based on the results given in Figure 4, for our synthetic example the outcome of our first-order design strategy as outlined in Section 3.2 is considered reliable up to a variance of Y of 3.0.

3.4.2. Correlations between observed variables and goal variables

Figure 5 shows plots of the spatial distribution of the correlations between the observable variables (h, Ln(K) and Ln(t)) and respectively the natural logarithm of the groundwater age at Q (Ln(τ_Q), see Figures 5a-5c, in which Q is the center of the a priori expected contaminant breakthrough zone) and the breakthrough location χ_Q of the particle a priori expected to break through at Q (Figures 5d-f). The particle that a priori is expected to break through at Q enters the confining layer at Z (see Figures 5d-f).

Figure 5a gives the correlation between the conductivity everywhere in the domain and the groundwater age at Q. These correlations were computed by defining a pseudo age determination at Q and calculating the parameter representer of this measurement throughout the domain. The representer values were subsequently divided by the square root of the product of the prior parameter variance and the age variance at Q, to yield the correlations. The age variance at Q was calculated by computing the value of the Ln(τ) representer at location Q.

Figures 5b, d and e were produced in a similar manner. For Figures 5b and e, however, the prior σ_h^2 field, which in contrast to the parameter variance is not known beforehand,

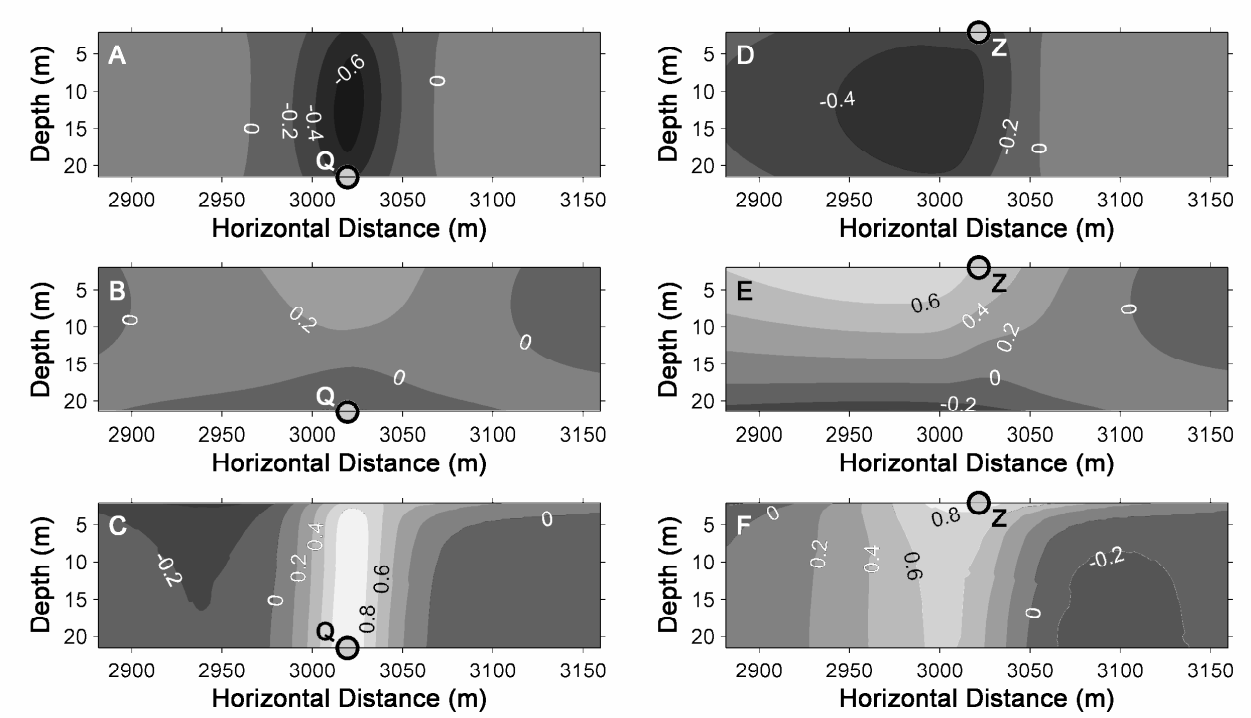

Figure 5. (A,B,C) The correlation between the groundwater age at or the travel time to Q and the log conductivity (A), the head (B) and the groundwater age (C) in every grid block of the centre area. (D,E,F) The correlation between the breakthrough location of the particle a priori expected to break through at Q (this particle enters the confining layer at Z) and the natural logarithm of the conductivity (D), the head (E) and the groundwater age (F) in every grid block of the centre area.

was inter- and extrapolated from prior head variances calculated at the potential measurement locations. Inter- and extrapolation of these values is justified, as the head variance field is smooth.

Figure 5c was constructed by defining in every grid cell a pseudo travel time measurement and calculating their Ln(t) representers for Ln(t) at the location of the pseudo measurement itself (yielding the prior $\sigma^2_{\mathrm{Ln}(t)}$ field) and for Ln(τ_Q) (yielding the cross covariances). Figure 5f was produced in a similar manner, with the distinction that now for every pseudo travel time measurement the location representer was calculated for the particle that a priori is expected to break through in Q.

From Figure 5 it appears that Ln(τ_Q) is particularly strongly correlated (correlation coefficient $\rho > 0.6$), in a narrow zone above Q, with Ln(K) and Ln(t). Whereas the Ln(t)-

Ln(τ_Q) correlation (Figure 5c) obviously is the strongest at Q (here ρ = 1), the Ln(K)-Ln(τ_Q) (Figure 5a) correlation is strongest around the center of the domain. This is because here Ln(K) maximally affects (via its covariance function) the conductivity of the area in which the particle moving towards Q is expected to travel, and therefore maximally affects Ln(τ_Q). A similar correlation pattern was found by *Harvey and Gorelick* [1995] (their Figure 6b).

Figure 5b shows that the head is only very weakly correlated with Ln(t). This is due to the small sensitivity of heads to the parameters.

The curvature of the positive Ln(t)-Ln(τ_Q) correlation zone in Figure 5c is caused by the fact that the particle arriving in Q has traveled a certain horizontal distance downgradient in Aquifer 1 before entering the confining layer (see also Figure 1). Travel times in the upper right part of the domain are correlated with the residence times of the corresponding particles in Aquifer 1, which are in turn correlated with the residence time in Aquifer 1 of the particle arriving in Q.

Whereas Ln(τ_Q) shows particularly strong correlations with Ln(K) and Ln(t), χ_Q is especially strongly correlated with h and Ln(t) (Figures 5e and 5f, respectively). The large h- χ_Q correlations found in the upper part of the domain (Figure 5e) are related to the particle transport through Aquifer 1: because of the relatively large expected horizontal distance traveled in Aquifer 1 (see also Figure 1), χ_Q is determined for an important part by the hydraulic gradient in Aquifer 1, which in turn is correlated with the heads in the upper part of the confining layer.

χ_Q-Ln(K) correlations (Figure 5d) are relatively weak, due to the limited vertical correlation of Ln(K) values. Figure 5f reveals that χ_Q shows strong correlations with Ln(t), particularly around Z. This makes sense, again because the horizontal distance traveled within the confining layer is expected to be very small and χ_Q is strongly determined by the distance travelled in Aquifer 1, which in turn is correlated with the vertical flow velocity in Aquifer 1. This vertical flow velocity is strongly correlated with the groundwater age near Z.

3.4.3 Examples of network designs

Figures 6 shows examples of near-optimal 10-measurement network designs, in the search of which the Genetic Algorithm was allowed to choose among *h*, *K* and *t* measurements. The age estimation error standard deviation was set at 10% of the untransformed a priori expected value.

In Figure 6a, the purpose of the observation network design was to minimize the groundwater age uncertainty at the control plane. The optimal design solely consists of age determinations, which is not surprising as they are strongly correlated with the groundwater age at the control plane. The horizontal correlation of travel time is not strong enough for all determinations to be placed next to each other at the control plane, which would be a logical configuration as then they directly sample the goal variables. Instead, the upper right part of the domain is also sampled, for reasons explained in the discussion of Figure 5c.

For the design shown Figure 6b, the sampling objective was to minimize the contaminant arrival location variance. *K*, *h* and *t* measurements are located in those areas where, based on Figures 5d-f, strong correlations with the breakthrough location collection χ are expected.

For Figure 6c, the objective was to minimize $\sigma^2_{\tau_{BT}}$, which is a combination of the objectives used in Figure 6a and 6b (see equation 1). The head measurement in the upper left-hand part of the confining layer primarily serves to constrain arrival location (see Figs. 5e and 5b). The fact that the age determinations are placed at the control plane (as in Figure 6a), rather than in the upper part of the confining layer (as in Figure 6b), indicates that they are primarily important to obtain information on $\tau(x^{CP})$, rather than on $\chi(x^{SZ})$. Apart from one head measurement, no measurements are chosen that are specifically aimed at reducing $p\left(x^{CP} \in \chi\right)$. The age determinations sample a narrower area than in Figure 6a, because their placement is now focused at obtaining information on the travel time towards the expected contaminant breakthrough zone, rather than towards the entire control plane. The focus of the design in Figure 6c on the reduction of arrival time uncertainty is probably due to the relatively wide contaminant source zone, which limits the reduction of the contaminant breakthrough location variance that can be achieved.

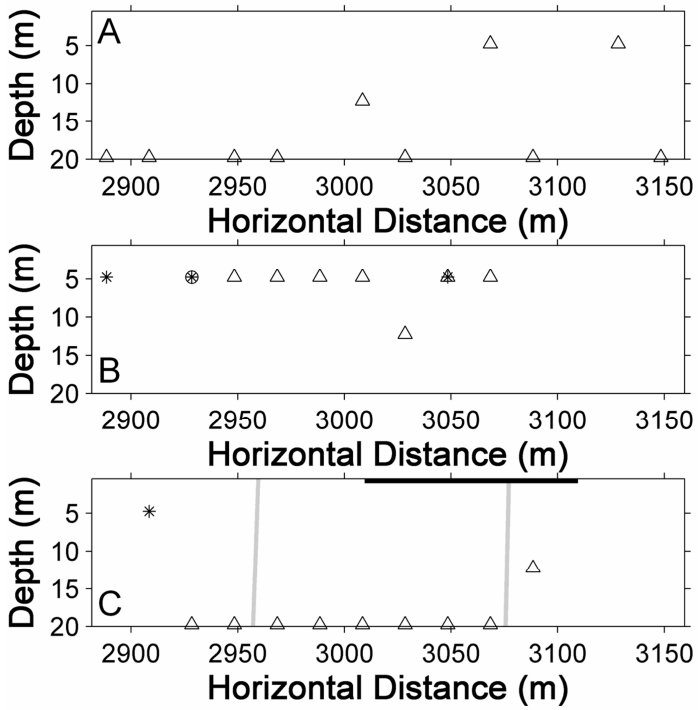

Figure 6. Near-optimal designs for minimizing the groundwater age uncertainty at the control plane (A), for minimizing the contaminant arrival location uncertainty (B), and for minimizing the contaminant breakthrough time uncertainty (C). The domains shown in this figure represent the confining unit in the area of interest (see Figure 1). The black bold line in (C) represents a projection of the contaminant source zone on the top of the confining layer. Grey bold lines delineate the (a priori) expected contaminant flow through the confining layer. Δ = *t* measurement, * = *h* measurement, ○ = *K* measurement.

3.4.4 Performance of age estimation networks compared with *K* and *h* networks

Figure 7 shows the posterior breakthrough variance of (near-)optimal designs as a function of network size, for observation networks containing only one measurement type. The figure shows that, if the travel time estimations are of a reasonable reliability, the uncertainty reduction that can be realized using travel time determinations is larger than can be achieved with the other measurement types (with reasonable network sizes). After having studied Figure 5 this is not surprising anymore: heads are only very

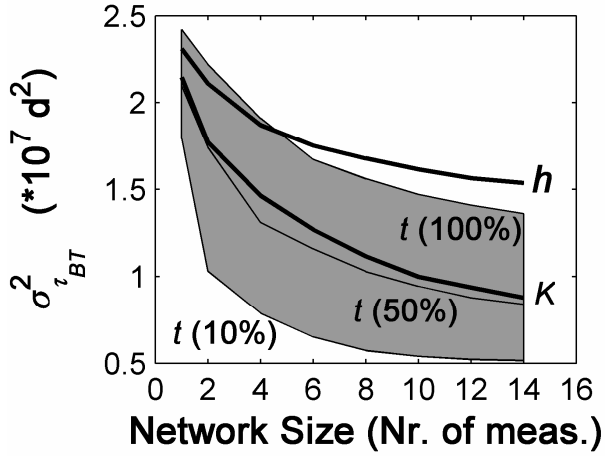

Figure 7. First-order estimation of the posterior breakthrough time uncertainty for networks consisting of only one observation type (h = pressure head, K = conductivity, t = groundwater age), as a function of network size. The given percentages refer to different levels of the age estimation error standard deviation. The prior breakthrough time uncertainty (no measurements) for this example was $4.85*10^7$ d^2.

weakly correlated with travel time, and conductivity is weakly correlated with arrival location. Groundwater age is the only variable that is strongly correlated with both arrival time and arrival location. Furthermore, groundwater age is more strongly correlated with arrival time than K is, and also more strongly correlated with arrival location than the head is. According to Figure 7, in our synthetic example an age determination network outperforms a K and an h network if the age estimation error standard deviation is less than 50% of the expected age, even though the error variances of the K and h measurements were chosen unrealistically small. So, if travel time estimations of a reasonable accuracy are available, more information can be obtained with fewer measurements than with the other two measurement types.

3.5. Conclusions and Discussion

A methodology was proposed that incorporates travel time determinations into measurement network design. The methodology was focused on minimizing model prediction uncertainty (specifically, contaminant breakthrough time uncertainty) and is

one of very few that take correlations between observations into account when doing so. Moreover, by directly calculating the covariances between observations and predictions, instead of evaluating the influence of the observations on the predictions via the posterior parameter covariance matrix, a major computational advantage is accomplished compared to previously reported network design algorithms aimed at prediction uncertainty minimization.

As the Gaussian assumption often is not valid for travel times, they were transformed to comply with the Bayesian framework applied here. The natural logarithm of travel time was shown to be approximately Gaussian distributed for systems of low to medium heterogeneity.

Based on this result, we derived expressions for the linearized covariances between the measurable variables and the natural logarithm of travel time (equation (C24)) and breakthrough time (equation (12)). The latter, together with the cross covariances between the observable variables and particle breakthrough locations, given by equation (13), are necessary for the calculation of posterior breakthrough time uncertainty given a certain set of measurements. In a synthetic example of contaminant breakthrough in a confining layer, the discrepancy between the linearized approximation of the prior variance of the natural logarithm of travel time and Monte Carlo results was less then 10% for variances of the natural logarithm of the conductivity up to 3.0.

Age estimations, if of a reasonable quality, were shown to be more valuable for the reduction of breakthrough time uncertainty than head and conductivity measurements. In our numerical example, even if the age estimation error standard deviation was taken as large as 50% of the expected value and head and conductivity measurements error variances were assumed to be very small, (near-)optimal age estimation networks still outperformed equally sized (near-)optimal networks of head or conductivity measurements.

Far sake of conciseness, we chose not to involve other considerations, like for example cost minimization, into the network design, other than restricting the designs to a certain number of measurements. However, such considerations can be accommodated very easily in the Genetic Algorithm by expanding the objective function with additional terms. An example of a Genetic Algorithm application involving both prediction uncertainty minimization and budget constraints is given by *Wagner* [1995].

In our calculations we assumed Gaussian distributed measurement errors for the log-transformed groundwater age estimations. It should be noted, however, that there are many factors contributing in different ways to the uncertainties involved in the translation of tracer concentrations to groundwater age, and the resultant of these factors might not always warrant the use of a Gaussian or even symmetric uncertainty structure. The most important sources of uncertainty are (note that not all uncertainty sources apply to all age dating techniques): pore-scale dispersion and macrodispersion resulting in mixed-age samples [*Maloszewski and Zuber*, 1982; *Bethke and Johnson*, 2002; *Weissmann et al.*, 2002; *Castro and Goblet*, 2005; *Manning et al.*, 2005], analytical error [*Solomon et al.*, 1992; *Ekwurzel et al.*, 1994], influence of uncertain recharge temperature affecting tracer concentrations at time of recharge [*Dunkle et al.*, 1993], nonconservative behavior of the tracer [*Dunkle et al.*, 1993], contamination [*Dunkle et al.*, 1993], water table fluctuations, and incomplete confinement of reactive decay products (e.g. ^{3}He [*Solomon et al.*, 1992]). It is yet unclear how reliable uncertainty estimates for age determinations can be obtained and whether corrections and transformations to the determinations can be formulated that can effectively make the uncertainty structure Gaussian. For arrival times in a conservative tracer test, on the other hand, these issues are far less problematic, considering the fact that the injection and detection times are relatively easy to determine and that the structure of the uncertainties involved in extracting the advective arrival time is likely to be either near-Gaussian or transformable to near-Gaussian.

In the present study, reactive-dispersive behavior of the *tracers*, and the influence of instationarity on this behavior, are accounted for only indirectly by treating them as sources of uncertainty to the travel time estimations that are themselves used in a strictly advective, conservative and stationary inverse computational framework. As such, the approach is suitable for situations in which reaction, dispersion and instationarity are thought to be of secondary importance for the tracer.

To keep the presentation simple, transport of the *contaminant* in the numerical example was assumed to be strictly advective and conservative as well. Although we recognize that reactive-dispersive behavior of the contaminant might be even a bigger source of uncertainty than the residence time of the groundwater within the transport volume, the considered measurement types, as treated in this Chapter, can only provide information

on the latter factor. Therefore, reactive-dispersive behavior of the contaminant is beyond the scope of the presented methodology.

The method is applicable to real world cases as long as using the Bayesian framework and the linear theory is warranted, which respectively places demands on data availability (e.g. parameter statistics and uncertainties, measurement errors, etc.) and puts restrictions on parameter variability. With regard to the computational demand of the method we can mention that the computation of the prior covariance matrix $M(\Xi,\Psi,\Theta^*,\mathrm{X})$ constitutes most of the computational burden. For the examples presented in Section 3.4.3, this took about 45 minutes on a Dell personal computer with a Pentium 4 2.6 GHz processor and 2.5 GB RAM. This computer time increases with the number of potential and pseudo measurements: for every potential or pseudo head measurement a groundwater model run is performed twice and a particle tracking run is performed, for every potential and pseudo conductivity measurement a groundwater model and a particle tracking run are performed once, and for every potential and pseudo travel time and location measurement two groundwater model runs and two particle-tracking runs are performed. Finally, for every potential and pseudo measurement a convolution with the parameter covariance matrix is required, so the number of unknown parameters (9,600 in this Chapter) also greatly influences computation times.

Appendix A Derivation of the Euler-Lagrange Equations

Forcing the conditions for a minimum in equation (11) yields a system of 9 coupled Euler-Lagrange equations. Besides the flow equation (6), the particle travel time equation (7) and the particle location equations (8 and 9), this system consists of an adjoint travel time adjoint equation, two particle location adjoint equations, a head adjoint equation, and a parameter equation, all of which are derived below.

A1. *X* Location Adjoint Equation

The conditions for a minimum in the extended objective function (equation (11)) prescribe the variation of (11) with respect to the *x* location of tracked particles to be zero. This yields:

$$\frac{\partial J}{\partial x_i^s}+\frac{2\lambda_h A(\alpha)h}{\partial x_i^s}+\frac{\partial\sum_i^{N_i}\sum_s^{N_{s_i}}2\lambda_{t_i}^s\left(\phi_{2_i}^s\right)}{\partial x_i^s}+\frac{\partial\sum_i^{N_i}\sum_s^{N_{s_i}}2\lambda_{x_i}^s\left(\phi_{3_i}^s\right)}{\partial x_i^s}+\frac{\partial\sum_i^{N_i}\sum_s^{N_{s_i}}2\lambda_{y_i}^s\left(\phi_{4_i}^s\right)}{\partial x_i^s}=0 \qquad \text{(A1)}$$

The derivatives in the third, fourth and the fifth term should only be taken for those travel steps *s* where x^s is really variable (i.e. not fixed by reaching an x-boundary of a cell in that travel step). Taking this into account, filling in equations (6-9) into (A1), working out the derivatives and dividing by 2 yields:

$$\begin{aligned}&-\frac{\partial M_p(h,\alpha,\mathrm{Ln}(t),\chi)}{\partial x_i^s}\left[P_v^{-1}\right]_{pn}\left[z_n-M_n(h,\alpha,\mathrm{Ln}(t),\chi)\right]-\lambda_{t_i}^s\frac{\partial\Delta t_i^s(\alpha,h,x_i^s,x_i^{s-1},y_i^s,y_i^{s-1})}{\partial x_i^s}\\&-\lambda_{t_i}^{s+1}\frac{\partial\Delta t_i^{s+1}(\alpha,h_i^{s+1},x_i^s,y_i^{s+1},y_i^s)}{\partial x_i^s}+(\lambda_{x_i}^s-\lambda_{x_i}^{s+1})-\lambda_{y_i}^s\frac{\partial\Delta y_i^s(\alpha,h_i^s,x_i^{s-1})}{\partial x_i^s}\\&-\lambda_{y_i}^{s+1}\frac{\partial\Delta y_i^{s+1}(\alpha,h,x_i^{s+1},x_i^s)}{\partial x_i^s}=0 \qquad \text{for } x_i^s\neq x_{cell\ boundary} \qquad \text{(A2)}\end{aligned}$$

and

$$-\frac{\partial M_p(h,\alpha,\mathrm{Ln}(t),\chi)}{\partial x_i^s}\left[P_v^{-1}\right]_{pn}\left[z_n-M_n(h,\alpha,\mathrm{Ln}(t),\chi)\right]+\lambda_{x_i}^s=0 \qquad \text{for } x_i^s=x_{cell\ boundary} \qquad \text{(A3)}$$

Note that the second and the fifth term of equation (A2) are always zero because Δt_i^s and Δy_i^s only depend on the *x* coordinates of travel step *s* if the step size is limited by reaching the x-boundary of a cell, in which case equation (A3) applies. Taking this into account and rearranging yields the *x* location adjoint equation:

$$\begin{aligned}\lambda_{x_i}^s=\lambda_{x_i}^{s+1}&+\frac{\partial M_p(h,\alpha,\mathrm{Ln}(t),\chi)}{\partial x_i^s}\left[P_v^{-1}\right]_{pn}\left[z_n-M_n(h,\alpha,\mathrm{Ln}(t),\chi)\right]+\lambda_{t_i}^{s+1}\frac{\partial\Delta t_i^{s+1}(\alpha_i^{s+1},x_i^s,y_i^{s+1},y_i^s)}{\partial x_i^s}\\&+\lambda_{y_i}^{s+1}\frac{\partial\Delta y_i^{s+1}(\alpha,h,x_i^{s+1},x_i^s)}{\partial x_i^s} \qquad \text{for } x_i^s\neq x_{cell\ boundary} \qquad \text{(A4)}\end{aligned}$$

$$\lambda_{x_i}^s=\frac{\partial M_p(h,\alpha,\mathrm{Ln}(t),\chi)}{\partial x_i^s}\left[P_v^{-1}\right]_{pn}\left[z_n-M_n(h,\alpha,\mathrm{Ln}(t),\chi)\right]=0 \qquad \text{for } x_i^s=x_{cell\ boundary} \qquad \text{(A5)}$$

with boundary condition $\lambda_{x_i}^{N_{s_i+1}} = 0$.

A2. *Y* Location Adjoint Equation

Following the same reasoning as in the derivation of the *x* location adjoint equation, the *y* location adjoint equation is given by:

$$\lambda_{y_i}^s = \lambda_{y_i}^{s+1} + \frac{\partial M_p(h,\alpha,\mathrm{Ln}(t),\chi)}{\partial y_i^s}\left[P_v^{-1}\right]_{pn}\left[z_n - M_n(h,\alpha,\mathrm{Ln}(t),\chi)\right] + \lambda_{t_i}^{s+1}\frac{\partial \Delta t_i^{s+1}(\alpha,h,x_i^{s+1},x_i^s,y_i^{s+1},y_i^s)}{\partial y_i^s}$$

$$+ \lambda_{x_i}^{s+1}\frac{\partial \Delta x_i^{s+1}(\alpha,h,y_i^{s+1},y_i^s)}{\partial y_i^s} \qquad \text{for } y_i^s \neq y_{cell\ boundary} \qquad \text{(A6)}$$

$$\lambda_{y_i}^s = \frac{\partial M_p(h,\alpha,\mathrm{Ln}(t),\chi)}{\partial y_i^s}\left[P_v^{-1}\right]_{pn}\left[z_n - M_n(h,\alpha,\mathrm{Ln}(t),\chi)\right] = 0 \qquad \text{for } y_i^s = y_{cell\ boundary} \qquad \text{(A7)}$$

with boundary condition $\lambda_{y_i}^{N_{s_i+1}} = 0$.

A3. Travel Time Adjoint Equation

The conditions for a minimum in the extended objective function (equation (11)) prescribe the variation of (11) with respect to the travel time to be zero. This yields:

$$\frac{\partial J}{\partial t_i^s} + \frac{2\lambda_h A(\alpha)h}{\partial t_i^s} + \frac{\partial \sum_i^{N_i}\sum_s^{N_{si}} 2\lambda_{t_i}^s\left(\phi_{2_i}^s\right)}{\partial t_i^s} + \frac{\partial \sum_i^{N_i}\sum_s^{N_{si}} 2\lambda_{x_i}^s\left(\phi_{3_i}^s\right)}{\partial t_i^s} + \frac{\partial \sum_i^{N_i}\sum_s^{N_{si}} 2\lambda_{y_i}^s\left(\phi_{4_i}^s\right)}{\partial t_i^s} = 0 \qquad \text{(A8)}$$

The second, fourth and fifth term of equation (A8) are zero. Working out the other terms and dividing by 2 directly yields the travel time adjoint equation:

$$\lambda_{t_i}^s = \lambda_{t_i}^{s+1} + \frac{\partial M_p(h,\alpha,\mathrm{Ln}(t),\chi)}{\partial t_i^s}\left[P_v^{-1}\right]_{pn}\left[z_n - M_n(h,\alpha,\mathrm{Ln}(t),\chi)\right] \qquad \text{(A9)}$$

with boundary condition $\lambda_{t_i}^{N_{s_i+1}} = 0$.

A4. Head Adjoint Equation

The conditions for a minimum in the extended objective function (equation (11)) prescribe the variation of (11) with respect to the heads to be zero. This yields:

$$\frac{\partial J}{\partial h}+\frac{2\lambda_h A(\alpha)h}{\partial h}+\frac{\partial\sum_i^{N_i}\sum_s^{N_{si}}2\lambda_{t_i}^s\left(\phi_{2_i}^s\right)}{\partial h}+\frac{\partial\sum_i^{N_i}\sum_s^{N_{si}}2\lambda_{x_i}^s\left(\phi_{3_i}^s\right)}{\partial h}+\frac{\partial\sum_i^{N_i}\sum_s^{N_{si}}2\lambda_{y_i}^s\left(\phi_{4_i}^s\right)}{\partial h}=0 \qquad \text{(A10)}$$

Working out equation (A10), dividing by 2 and rearranging yields the head adjoint equation:

$$A_{gf}(\alpha)\lambda_{h_f}=\frac{\partial M_p(h,\alpha,\mathrm{Ln}(t),\chi)}{\partial h_g}\left[P_v^{-1}\right]_{pn}\left[z_n-M_n(h,\alpha,\mathrm{Ln}(t),\chi)\right]+\sum_i^{N_i}\sum_s^{N_{si}}\lambda_{t_i}^s\frac{\partial\Delta t_i^s\left(\alpha,h,x_i^s,x_i^{s-1},y_i^s,y_i^{s-1}\right)}{\partial h_g}$$
$$+\sum_i^{N_i}\sum_s^{N_{si}}\lambda_{x_i}^s\frac{\partial\Delta x_i^s\left(\alpha,h,y_i^s,y_i^{s-1}\right)}{\partial h_g}+\sum_i^{N_i}\sum_s^{N_{si}}\lambda_{y_i}^s\frac{\partial\Delta y_i^s\left(\alpha,h,x_i^s,x_i^{s-1}\right)}{\partial h_g} \qquad \text{(A11)}$$

A5. Parameter Equation

The conditions for a minimum in the extended objective function (equation (11)) prescribe the variation of (11) with respect to the parameters to be zero. This yields:

$$\frac{\partial J}{\partial \alpha}+\frac{2\lambda_h A(\alpha)h}{\partial \alpha}+\frac{\partial\sum_i^{N_i}\sum_s^{N_{si}}2\lambda_{t_i}^s\left(\phi_{2_i}^s\right)}{\partial \alpha}+\frac{\partial\sum_i^{N_i}\sum_s^{N_{si}}2\lambda_{x_i}^s\left(\phi_{3_i}^s\right)}{\partial \alpha}+\frac{\partial\sum_i^{N_i}\sum_s^{N_{si}}2\lambda_{y_i}^s\left(\phi_{4_i}^s\right)}{\partial \alpha}=0 \qquad \text{(A12)}$$

Working out equation (A12), dividing by 2 and rearranging yields the parameter equation:

$$\alpha_l = \overline{\alpha}_l - P_\alpha \left[h_g \frac{\partial A(\alpha)}{\partial \alpha_k} \lambda_{h_f} - \sum_i^{N_i} \sum_s^{N_{s_i}} \lambda_{t_i}^s \frac{\partial \Delta t_i^s \left(\alpha, h, x_i^s, x_i^{s-1}, y_i^s, y_i^{s-1}\right)}{\partial \alpha_k} \right.$$

$$\left. - \sum_i^{N_i} \sum_s^{N_{s_i}} \lambda_{x_i}^s \frac{\partial \Delta x_i^s \left(\alpha, h, y_i^s, y_i^{s-1}\right)}{\partial \alpha_k} - \sum_i^{N_i} \sum_s^{N_{s_i}} \lambda_{y_i}^s \frac{\partial \Delta y_i^s \left(\alpha, h, x_i^s, x_i^{s-1}\right)}{\partial \alpha_k} \right] \quad \text{(A13)}$$

Appendix B Representer Expansions

In the representer-based inverse algorithm [*Valstar et al.*, 2004], the unknowns in the nonlinear system of Euler-Lagrange equations are expanded in finite series, allowing the equations in the system to be decoupled and solved iteratively. Every measurement adds a term to this finite series, consisting of (1) a basis function or representer, quantifying the influence of the measurement on the estimate of the variable for which the representer is defined, and (2) its coefficient, quantifying the weight given to the representer, which depends on the misfit between measurement value and measurement prediction. The definitions of the representer functions are:

$$\lambda_{t_i} = \sum_{p=1}^{N_p} \Lambda_{ip} b_p \quad \text{(B1)}$$

$$\lambda_{x_i} = \sum_{p=1}^{N_p} \Pi_{ip} b_p \quad \text{(B2)}$$

$$\lambda_{y_i} = \sum_{p=1}^{N_p} \mathrm{H}_{ip} b_p \quad \text{(B3)}$$

$$\lambda_{h_f} = \sum_{p=1}^{N_p} \Gamma_{fp} b_p \quad \text{(B4)}$$

$$\alpha_l = \overline{\alpha}_l + \sum_{p=1}^{N_p} \Psi_{lp} b_p \quad \text{(B5)}$$

$$h_g = h_{F_g} + h_{corr_g} + \sum_{p=1}^{N_p} \Xi_{gp} b_p \quad \text{(B6)}$$

$$x_i = x_{F_i} + x_{corr_i} + \sum_{p=1}^{N_p} \mathrm{X}_{ip} b_p \quad \text{(B7)}$$

$$y_i = y_{F_i} + y_{corr_i} + \sum_{p=1}^{N_p} \mathrm{Y}_{ip} b_p \quad \text{(B8)}$$

$$t_i^\eta = t_{F_i} + t_{corr_i} + \sum_{p=1}^{N_p} t_i^{\eta-1} \Theta_{ip}^* b_p \quad \text{(B9)}$$

where b is the vector of representer coefficients, N_p is the number of measurements, Λ_{ip} is the travel time adjoint representer of measurement p, calculated for particle i, Π_{ip} is the x location adjoint representer of measurement p, calculated for particle i, H_{ip} is the y

location adjoint representer of measurement *p*, calculated for particle *i*, Γ_{fp} is the head adjoint representer of measurement *p*, calculated for the head state variable *f*, Ψ_{lp} is the parameter representer of measurement *p*, calculated for parameter *l*, Ξ_{gp} is the head representer of measurement *p*, calculated for head state variable *g*, X_{ip} and Y_{ip} are respectively the *x* and *y* location representer of measurement *p*, calculated for particle *i*, η is the iteration number and Θ^{*}_{ip} is the Ln(*t*) representer of measurement *p*, calculated for particle *i*. In order to be able to expand the untransformed travel time t_i, Θ^{*}_{pi} is multiplied by the derivative $dt_i / d\ln t_i = t_i$, which is estimated using its value in the previous iteration ($t_i^{\eta-1}$). h_F, x_F, y_F, and t_F are the solutions obtained by solving equations (6-9) with $\alpha = \bar{\alpha}$. h_{corr}, x_{corr}, y_{corr}, and t_{corr} are correction terms. In our first-order design method, the algorithm is terminated after the first iteration, the unknown variables are not actually updated (this would require actual sampling) and therefore the representer coefficients *b* and the correction terms h_{corr}, x_{corr}, y_{corr}, and t_{corr} do not have to be calculated. The algorithm is initiated using $\alpha = \bar{\alpha}$, $h = h_F$, $t_i = t_{i_F}$, $x_i = x_{i_F}$, $y_i = y_{i_F}$, and $\lambda_h = \lambda_{t_i} = \lambda_{x_i} = \lambda_{y_i} = 0$.

Appendix C Representer Derivations

For the sake of readability, the explicit statement of the dependencies of *A*, Δt, Δx and Δy are omitted from now on.

C1. *X* Location Adjoint Representers

Inserting the representer expansions (B1-9) into the *x* location adjoint equations (A4-5) yields:

$$\Pi_{ip}^{s} b_p = \Pi_{ip}^{s+1} b_p + \frac{\partial M_p(h,\alpha,\mathrm{Ln}(t),\chi)}{\partial x_i^s}\left[P_v^{-1}\right]_{pn}(z_n - M_n(\,)) \quad + \Lambda_{ip}^{s+1} b_p \frac{\partial \Delta t_i^{s+1}}{\partial x_i^s} + \mathrm{H}_{ip}^{s+1} b_p \frac{\partial \Delta y_i^{s+1}}{\partial x_i^s}$$

$$\text{for } x_i^s \neq x_{cell\ boundary} \qquad \text{(C1)}$$

$$\Pi_{ip}^{s} b_p = \frac{\partial M_p(h,\alpha,\mathrm{Ln}(t),\chi)}{\partial x_i^s}\left[P_v^{-1}\right]_{pn}(z_n - M_n(\,)) \qquad \text{for } x_i^s = x_{cell\ boundary} \qquad \text{(C2)}$$

where $M_n(\ ) = M_n\left(h_F + h_{corr} + \Xi b, \overline{\alpha}_l + \Psi b, \mathrm{Ln}\left(t_F + t_{corr} + t_F \Theta^* b\right), x_F + x_{corr} + \mathrm{X} b\right)$. The coefficients *b* for all *p* measurements are now chosen as:

$$b_p = \left[P_v^{-1}\right]_{pn}\left(z_n - M_n(\ )\right) \qquad \text{(C3)}$$

Equations (C1-2) can only be fulfilled for nonzero *b* if:

$$\Pi_{ip}^{s} = \Pi_{ip}^{s+1} + \frac{\partial M_p\left(h, \alpha, \mathrm{Ln}(t), \chi\right)}{\partial x_i^s} + \Lambda_{ip}^{s+1}\frac{\partial \Delta t_i^{s+1}}{\partial x_i^s} + \mathrm{H}_{ip}^{s+1}\frac{\partial \Delta y_i^{s+1}}{\partial x_i^s} \qquad \text{for } x_i^s \neq x_{cell\ boundary} \qquad \text{(C4)}$$

$$\Pi_{ip}^{s} = \frac{\partial M_p\left(h, \alpha, \mathrm{Ln}(t), \chi\right)}{\partial x_i^s} = 0 \qquad \text{for } x_i^s = x_{cell\ boundary} \qquad \text{(C5)}$$

with boundary condition $\Pi_{ip}^{N_{s_i}+1} = 0$. The second term on the right hand side of (C4) and the term on the right hand side of (C5) are nonzero only in case of (pseudo) measurements of χ_i (by definition at $s = N_{s_i}$). In that case $\frac{\partial M_p(\chi_i)}{\partial x_i^{N_{s_i}}} = 1$.

C2. Y Location Adjoint Representers

Following the same reasoning as above, it follows for the *y* location adjoint representers:

$$\mathrm{H}_{ip}^{s} = \mathrm{H}_{ip}^{s+1} + \frac{\partial M_p\left(h, \alpha, \mathrm{Ln}(t), \chi\right)}{\partial y_i^s} + \Lambda_{ip}^{s+1}\frac{\partial \Delta t_i^{s+1}}{\partial y_i^s} + \Pi_{ip}^{s+1}\frac{\partial \Delta x_i^{s+1}}{\partial y_i^s} \qquad \text{for } y_i^s \neq y_{cell\ boundary} \qquad \text{(C6)}$$

$$\mathrm{H}_{ip}^{s} = \frac{\partial M_p\left(h, \alpha, \mathrm{Ln}(t), \chi\right)}{\partial y_i^s} = 0 \qquad \text{for } y_i^s = y_{cell\ boundary} \qquad \text{(C7)}$$

with boundary condition $\mathrm{H}_{ip}^{N_{s_i}+1} = 0$. The second term on the right hand side of (C6) and the term on the right hand side of (C7) are always zero. Therefore (C6-7) can be simplified into:

$$\mathrm{H}_{ip}^{s} = \mathrm{H}_{ip}^{s+1} - \Lambda_{ip}^{s+1} \frac{\partial \Delta t_i^{s+1}}{\partial y_i^s} - \Pi_{ip}^{s+1} \frac{\partial \Delta x_i^{s+1}}{\partial y_i^s} \qquad \text{for } y_i^s \neq y_{cell\ boundary} \qquad \text{(C8)}$$

$$\mathrm{H}_{ip}^{s} = 0 \qquad \text{for } y_i^s = y_{cell\ boundary} \qquad \text{(C9)}$$

with boundary condition $\mathrm{H}_{ip}^{N_{s_i}+1} = 0$.

C3. Travel Time Adjoint Representers

Inserting the representer expansions (B1-9) into the travel time adjoint equation (A9) yields:

$$\Lambda_{ip}^{s} b_p = \Lambda_{ip}^{s+1} b_p + \frac{\partial M_p(h, \alpha, \mathrm{Ln}(t), \chi)}{\partial t_i^s} \left[P_v^{-1}\right]_{pn} (z_n - M_n(\ )) \qquad \text{(C10)}$$

After inserting (C3) into (C10), the resulting equation can only be fulfilled for non-zero *b* if:

$$\Lambda_{ip}^{s} = \Lambda_{ip}^{s+1} + \frac{\partial M_p(h, \alpha, \mathrm{Ln}(t), \chi)}{\partial t_i^s} \qquad \text{(C11)}$$

with boundary condition $\Lambda_{ip}^{N_s+1} = 0$. The second term of equation (C11) is nonzero only in case of measurements of Ln(t_i). In that case $\frac{\partial M_p(\mathrm{Ln}(t_i))}{\partial t_i^s} = \frac{1}{t_i^s}$, with t_i^s approximated by its most recent estimate.

C4. Head Adjoint Representers

Inserting the representer definitions (B1-9) into the head adjoint equation (A11) yields:

$$A_{gf}\Gamma_{fp}b_p = \frac{\partial M_p(h,\alpha,\mathrm{Ln}(t),\chi)}{\partial h_g}\left[P_v^{-1}\right]_{pn}(z_n - M_n(\ ))$$
$$+\sum_i^{N_i}\sum_s^{N_{si}}\Lambda_{ip}^s b_p\frac{\partial\Delta t_i^s}{\partial h_g}+\sum_i^{N_i}\sum_s^{N_{si}}\Pi_{ip}^s b_p\frac{\partial\Delta x_i^s}{\partial h_g}+\sum_i^{N_i}\sum_s^{N_{si}}\mathrm{H}_{ip}^s b_p\frac{\partial\Delta y_i^s}{\partial h_g} \qquad \text{(C12)}$$

Equation (C12) can only be fulfilled for nonzero *b* if

$$A_{gf}\Gamma_{fp} = \frac{\partial M_p(h,\alpha,\mathrm{Ln}(t),\chi)}{\partial h_g}+\sum_i^{N_i}\sum_s^{N_{si}}\Lambda_{ip}^s\frac{\partial\Delta t_i^s}{\partial h_g}+\sum_i^{N_i}\sum_s^{N_{si}}\Pi_{ip}^s\frac{\partial\Delta x_i^s}{\partial h_g}+\sum_i^{N_i}\sum_s^{N_{si}}\mathrm{H}_{ip}^s\frac{\partial\Delta y_i^s}{\partial h_g} \qquad \text{(C13)}$$

C5. Parameter Representers

Inserting the representer definitions into the parameter equation (A13) yields:

$$\bar{\alpha}_l + \Psi_{lp}b_p = \bar{\alpha}_l - P_{\alpha_{lk}}\left[h_g\frac{\partial A_{gf}}{\partial\alpha_k}\Gamma_{fp}b_p - \sum_i^{N_i}\sum_s^{N_{si}}\Lambda_{ip}b_p\frac{\partial\Delta t_i^s}{\partial\alpha_k}-\sum_i^{N_i}\sum_s^{N_{si}}\Pi_{ip}b_p\frac{\partial\Delta x_i^s}{\partial\alpha_k}\right.$$
$$\left.-\sum_i^{N_i}\sum_s^{N_{si}}\mathrm{H}_{ip}b_p\frac{\partial\Delta y_i^s}{\partial\alpha_k}\right] \qquad \text{(C14)}$$

Equation (C14) can only be fulfilled for nonzero *b* if:

$$\Psi_{lp} = -P_{\alpha_{lk}}\left[h_g\frac{\partial A_{gf}}{\partial\alpha_k}\Gamma_{fp}-\sum_i^{N_i}\sum_s^{N_{si}}\Lambda_{ip}\frac{\partial\Delta t_i^s}{\partial\alpha_k}-\sum_i^{N_i}\sum_s^{N_{si}}\Pi_{ip}\frac{\partial\Delta x_i^s}{\partial\alpha_k}-\sum_i^{N_i}\sum_s^{N_{si}}\mathrm{H}_{ip}\frac{\partial\Delta y_i^s}{\partial\alpha_k}\right] \qquad \text{(C15)}$$

C6. Head Representers

The head representers should be the exact linearizations of the heads around the head estimates of the previous iteration. For a derivation see Valstar (2001) and Valstar et al. (2004). The result is:

$$A_{fg}\Xi_{gp} = -\frac{\partial A_{fg}}{\partial \alpha_k}\Psi_{kp}h_g \qquad \text{(C16)}$$

C7. *X* Location Representers

For the calculation of the *x* location representer, an exact linearization of the *x* location equation (8) is performed around the most recent estimate of x_i. Since the variation in the parameters induced by the measurements *p* is given by $\Psi_{lp}\partial b_p$ (B5), the variation of the heads by $\Xi_{gp}\partial b_p$ (B6), the variation of the *y* location of particle *i* by $\mathrm{Y}_{ip}\partial b_p$ (B8), and the variation of the travel time of particle *i* by $t_i\,\Theta^*_{ip}\partial b_p$ (B9), a linear relationship between the *x* location of particle *i* on one hand and the parameters, heads, *y* location of particle *i* and travel time of particle *i* on the other implies that the variation in *x* locations of particles, given by $\mathrm{X}_{ip}\partial b_p$ (see equation (B7)), is:

$$\mathrm{X}^s_{ip}\partial b_p = \sum_{s'=1}^{s}\frac{\partial \Delta x_i^{s'}}{\partial \alpha_l}\Psi_{lp}\partial b_p + \sum_{s'=1}^{s}\frac{\partial \Delta x_i^{s'}}{\partial h_g}\Xi_{gp}\partial b_p + \sum_{s'=1}^{s}\frac{\partial \Delta x_i^{s'}}{\partial y_i^{s'}}\mathrm{Y}^{s'}_{ip}\partial b_p + \sum_{s'=1}^{s}\frac{\partial \Delta x_i^{s'}}{\partial y_i^{s'-1}}\mathrm{Y}^{s'-1}_{ip}\partial b_p,$$

$$\text{for } x_i^s \neq x_{cell\ boundary} \qquad \text{(C17)}$$

$$\mathrm{X}^s_{ip}\partial b_p = \sum_{s'=1}^{s-1}\frac{\partial \Delta x_i^{s'}}{\partial \alpha_l}\Psi_{lp}\partial b_p + \sum_{s'=1}^{s-1}\frac{\partial \Delta x_i^{s'}}{\partial h_g}\Xi_{gp}\partial b_p + \sum_{s'=1}^{s-1}\frac{\partial \Delta x_i^{s'}}{\partial y_i^{s'}}\mathrm{Y}^{s'}_{ip}\partial b_p + \sum_{s'=1}^{s-1}\frac{\partial \Delta x_i^{s'}}{\partial y_i^{s'-1}}\mathrm{Y}^{s'-1}_{ip}\partial b_p,$$

$$\text{for } x_i^s = x_{cell\ boundary} \qquad \text{(C18)}$$

with boundary condition $\mathrm{Y}^0_{ip} = 0$. The function of s' is the same as that of *s*. Dividing (C17-18) by ∂b_p and putting it in sequential notation yields the *x* location representer:

$$\mathrm{X}^s_{ip} = \mathrm{X}^{s-1}_{ip} + \frac{\partial \Delta x_i^s}{\partial \alpha_l}\Psi_{lp} + \frac{\partial \Delta x_i^s}{\partial h_g}\Xi_{gp} + \frac{\partial \Delta x_i^s}{\partial y_i^s}\mathrm{Y}^s_{ip} + \frac{\partial \Delta x_i^s}{\partial y_i^{s-1}}\mathrm{Y}^{s-1}_{ip}, \qquad \text{for } x_i^s \neq x_{cell\ boundary} \qquad \text{(C19)}$$

$$\mathrm{X}^s_{ip} = \mathrm{X}^{s-1}_{ip} \qquad \text{for } x_i^s = x_{cell\ boundary} \qquad \text{(C20)}$$

with boundary conditions $\mathrm{X}^0_{ip} = \mathrm{Y}^0_{ip} = 0$.

C8. *Y* Location Representers

The same reasoning holds for the *y* location representers:

$$\mathrm{Y}_{ip}^{s} = \mathrm{Y}_{ip}^{s-1} + \frac{\partial \Delta x_i^s}{\partial \alpha_l}\Psi_{lp} + \frac{\partial \Delta y_i^s}{\partial h_g}\Xi_{gp} + \frac{\partial \Delta y_i^s}{\partial x_i^s}\mathrm{X}_{ip}^{s} + \frac{\partial \Delta y_i^s}{\partial x_i^{s-1}}\mathrm{X}_{ip}^{s-1}, \qquad \text{for } y_i^s \neq y_{cell\ boundary} \tag{C21}$$

$$\mathrm{Y}_{ip}^{s} = \mathrm{Y}_{ip}^{s-1} \qquad \text{for } y_i^s = y_{cell\ boundary} \tag{C22}$$

with boundary conditions $\mathrm{Y}_{ip}^{0} = \mathrm{X}_{ip}^{0} = 0$.

C9. Ln(Travel Time) Representers

For the calculation of the Ln(*t*) representer, an exact linearization of the travel time equation (7) is performed around the most recent estimate of the travel time. Following similar considerations as above, the variation in Ln(t_i) travel time, given by $t_i\,\Theta_{ip}^{*}\partial b_p$ (see equation (B9)), is:

$$\begin{aligned} t_i^s\Theta_{ip}^{*s}\partial b_p = &\sum_{s'=1}^{s}\frac{\partial \Delta t_i^{s'}}{\partial \alpha_l}\Psi_{lp}\partial b_p + \sum_{s'=1}^{s}\frac{\partial \Delta t_i^{s'}}{\partial h_g}\Xi_{gp}\partial b_p + \sum_{s'=1}^{s}\frac{\partial \Delta t_i^{s'}}{\partial x_i^{s'}}\mathrm{X}_{ip}^{s'}\partial b_p \\ &+ \sum_{s'=1}^{s}\frac{\partial \Delta t_i^{s'}}{\partial x_i^{s'-1}}\mathrm{X}_{ip}^{s'-1}\partial b_p + \sum_{s'=1}^{s}\frac{\partial \Delta t_i^{s'}}{\partial y_i^{s'}}\mathrm{Y}_{ip}^{s'}\partial b_p + \sum_{s'=1}^{s}\frac{\partial \Delta t_i^{s'}}{\partial y_i^{s'-1}}\mathrm{Y}_{ip}^{s'-1}\partial b_p \end{aligned} \tag{C23}$$

Dividing (C23) by ∂b_p, rearranging, and putting it in sequential notation yields the Ln(*t*) representer:

$$\Theta_{ip}^{*s} = \frac{1}{t_i^s}\left[\Theta_{ip}^{*s-1} + \frac{\partial \Delta t_i^s}{\partial \alpha_l}\Psi_{lp} + \frac{\partial \Delta t_i^s}{\partial h_g}\Xi_{gp} + \frac{\partial \Delta t_i^s}{\partial x_i^s}\mathrm{X}_{ip}^{s} + \frac{\partial \Delta t_i^s}{\partial x_i^{s-1}}\mathrm{X}_{ip}^{s-1} + \frac{\partial \Delta t_i^s}{\partial y_i^s}\mathrm{Y}_{ip}^{s} + \frac{\partial \Delta t_i^s}{\partial y_i^{s-1}}\mathrm{Y}_{ip}^{s-1}\right] \tag{C24}$$

with boundary conditions $\Theta_{ip}^{*0} = \mathrm{X}_{ip}^{0} = \mathrm{Y}_{ip}^{0} = 0$.

C10. Correction Terms

The correction terms h_{corr}, t_{corr}, x_{corr}, and y_{corr} are chosen in such a way that the forward flow (6), the particle travel time (7), the particle x-location (8), and the particle y-location

equation (9) equation are fulfilled, respectively. For h_{corr}, first the unknown variables in (6) are replaced with the representer expansions (B1-9), and subsequently the head representer equation (C16), multiplied by b_p and summed over all measurements, is inserted. This yields [*Valstar*, 2001; *Valstar et al.*, 2004]:

$$A_{fg}h_{corr_g} = q_f + \frac{\partial A_{fg}}{\partial \alpha_k}(\alpha - \overline{\alpha})h_g - A_{fg}h_{F_g} \tag{C25}$$

For t_{corr}, first the unknown variables in (7) are replaced with the representer expansions (B1-9), and subsequently the Ln(travel time) representer equation (C24), multiplied by b_p and summed over all measurements, is inserted. This yields:

$$t^s_{corr_i} = t^{s-1}_i + \Delta t^s_i - t^s_{F_i} - \Theta^{*s-1}_{ip} b_p - \frac{\partial \Delta t^s_i}{\partial \alpha_l}\Psi_{lp} b_p - \frac{\partial \Delta t^s_i}{\partial h_g}\Xi_{gp} b_p - \frac{\partial \Delta t^s_i}{\partial x^s_i}\mathrm{X}^s_{ip} b_p \tag{C26}$$

$$- \frac{\partial \Delta t^s_i}{\partial x^{s-1}_i}\mathrm{X}^{s-1}_{ip} - \frac{\partial \Delta t^s_i}{\partial y^s_i}\mathrm{Y}^s_{ip} - \frac{\partial \Delta t^s_i}{\partial y^{s-1}_i}\mathrm{Y}^{s-1}_{ip}$$

Since $t^{s-1}_i - \Theta^{*s-1}_{ip} b_p = t^{s-1}_{corr_i} + t^{s-1}_{F_i}$ (see equation B9), we have:

$$t^s_{corr_i} = t^{s-1}_{corr_i} + t^{s-1}_{F_i} - t^s_{F_i} + \Delta t^s_i - \frac{\partial \Delta t^s_i}{\partial \alpha_l}\Psi_{lp} b_p - \frac{\partial \Delta t^s_i}{\partial h_g}\Xi_{gp} b_p - \frac{\partial \Delta t^s_i}{\partial x^s_i}\mathrm{X}^s_{ip} b_p \tag{C27}$$

$$- \frac{\partial \Delta t^s_i}{\partial x^{s-1}_i}\mathrm{X}^{s-1}_{ip} - \frac{\partial \Delta t^s_i}{\partial y^s_i}\mathrm{Y}^s_{ip} - \frac{\partial \Delta t^s_i}{\partial y^{s-1}_i}\mathrm{Y}^{s-1}_{ip}$$

Following similar reasoning, we have for x_{corr}:

$$x^s_{corr_i} = x^{s-1}_{corr_i} + x^{s-1}_{F_i} - x^s_{F_i} + \Delta x^s_i - \frac{\partial \Delta x^s_i}{\partial \alpha_l}\Psi_{lp} b_p - \frac{\partial \Delta x^s_i}{\partial h_g}\Xi_{gp} b_p - \frac{\partial \Delta x^s_i}{\partial y^s_i}\mathrm{Y}^s_{ip} b_p - \frac{\partial \Delta x^s_i}{\partial y^{s-1}_i}\mathrm{Y}^{s-1}_{ip} b_p$$

$$\text{for } x^s_i \neq x_{cell\ boundary} \tag{C28}$$

$$x^s_{corr_i} = -x^s_{F_i} + x_{cell\ boundary} \qquad \text{for } x^s_i \neq x_{cell\ boundary} \tag{C29}$$

And for y_{corr}:

$$y_{corr_i}^s = y_{corr_i}^{s-1} + y_{F_i}^{s-1} - y_{F_i}^s + \Delta y_i^s - \frac{\partial \Delta y_i^s}{\partial \alpha_l} \Psi_{lp} b_p - \frac{\partial \Delta y_i^s}{\partial h_g} \Xi_{gp} b_p - \frac{\partial \Delta y_i^s}{\partial x_i^s} \mathrm{X}_{ip}^s b_p - \frac{\partial \Delta y_i^s}{\partial x_i^{s-1}} \mathrm{X}_{ip}^{s-1} b_p$$

$$\text{for } y_i^s \neq y_{cell\ boundary} \qquad \text{(C30)}$$

$$y_{corr_i}^s = -y_{F_i}^s + y_{cell\ boundary} \qquad \text{for } y_i^s \neq y_{cell\ boundary} \qquad \text{(C31)}$$

During iteration η, $\Psi_{lp} b_p$, $\Xi_{gp} b_p$, $\mathrm{X}_{ip}^s b_p$, $\mathrm{X}_{ip}^{s-1} b_p$, $\mathrm{Y}_{ip}^s b_p$ and $\mathrm{Y}_{ip}^{s-1} b_p$ in equations (C27-31) are not known and replaced by the estimations from the previous iteration: $\left(\alpha_l^{\eta-1} - \overline{\alpha}_l\right)$, $\left(h_g^{\eta-1} - h_{F_g}^{\eta-1} - h_{corr_g}^{\eta-1}\right)$, $\left(x_i^{s^{\eta-1}} - x_{F_i}^{s^{\eta-1}} - x_{corr_i}^{s^{\eta-1}}\right)$, $\left(x_i^{s-1^{\eta-1}} - x_{F_i}^{s-1^{\eta-1}} - x_{corr_i}^{s-1^{\eta-1}}\right)$, $\left(y_i^{s^{\eta-1}} - y_{F_i}^{s^{\eta-1}} - y_{corr_i}^{s^{\eta-1}}\right)$, and $\left(y_i^{s-1^{\eta-1}} - y_{F_i}^{s-1^{\eta-1}} - y_{corr_i}^{s-1^{\eta-1}}\right)$, respectively.

References

Anderman, E. R., and M. C. Hill (2001), MODFLOW-2000, the U.S. Geological Survey modular ground-water model - documentation of the advective-transport observation (ADV2) package, version 2, open-file report 01-54, U.S. Geological Survey, Denver, CO.

Bethke, C. M., and T. M. Johnson (2002), Paradox of groundwater age: correction, *Geology*, 30, 385-388.

Bogardi, I., A. Bardossy, and L. Duckstein (1985), Multicriterion network design using geostatistics, *Water Resources Research*, 21, 199-208.

Castro, M. C., and P. Goblet (2005), Calculation of ground water ages - a comparative analysis, *Ground Water*, 43, 368-380.

Chang, L.-F., N.-Z. Sun, and W. W.-G. Yeh (2005), Optimal observation network design for parameter structure identification in groundwater modeling, *Water Resources Research*, 41, W03002, doi:03010.01029/02004WR003514.

Cirpka, O. A., and P. K. Kitanidis (2000), An advective-dispersive stream tube approach for the transfer of conservative-tracer data to reactive transport, *Water Resources Research*, 36, 1209-1220.

Cirpka, O. A., and P. K. Kitanidis (2001), Sensitivity of temporal moments calculated by the adjoint-state method and joint inversing of head and tracer data, *Advances in Water Resources*, 24, 89-103.

Cvetkovic, V. D., A. M. Shapiro, and G. Dagan (1992), A solute flux approach to transport in heterogeneous formations 2. Uncertainty analysis, *Water Resources Research*, 28, 1377-1388.

Dagan, G. (1989), *Flow and Transport in Porous Formations*, Springer-Verlag, Berlin.

Dettinger, M. D., and J. L. Wilson (1981), First order analysis of uncertainty in numerical methods of groundwater flow 1. Mathematical development, *Water Resources Research*, 17, 149-161.

Dunkle, S. A., L. N. Plummer, E. Busenberg, P. J. Phillips, J. M. Denver, A. Hamilton, R. L. Michel, and T. B. Coplen (1993), Chlorofluorocarbons (CCl3F and CCl2F2) as dating tools and hydrologic tracers in shallow groundwater of the Delmarva Peninsula, Atlantic Coastal plane, *Water Resources Research*, 29, 3837-3860.

Ekwurzel, B., P. Schlosser, W. M. Smethie Jr, L. N. Plummer, E. Busenberg, R. L. Michel, R. Weppernig, and M. Stute (1994), Dating of shallow groundwater: comparison of the transient tracers 3H/3He, chlorofluorocarbons, and 85Kr, *Water Resources Research*, 30, 1693-1708.

Feyen, L., J. J. Gomez-Hernandez, P. J. Ribeiro Jr., K. J. Beven, and F. De Smedt (2003), A Bayesian approach to stochastic capture zone delineation incorporating arrival times, conductivity measurements, and hydraulic head observations, *Water Resources Research*, 39, 1126, doi:1110.1029/2002WR001544.

Feyen, L., and S. M. Gorelick (2005), Framework to evaluate the worth of hydraulic conductivity data for optimal groundwater resources management in ecologically sensitive areas, *Water Resources Research*, 41, W03019, doi:03010.01029/02003WR002901.

Harvey, C. F., and S. M. Gorelick (1995), Mapping hydraulic conductivity: sequential conditioning with measurements of solute arrival time, hydraulic head, and local conductivity, *Water Resources Research*, 31, 1615-1626.

Hendricks Franssen, H. J. W. M. and F. Stauffer (2005), Optimal design of measurement networks for groundwater flow predictions, *Advances in Water Resources*, 28, 451-465.

Herrera, G. S., J. Guarnaccia, and G. F. Pinder (2000), A methodology for the design of space-time groundwater quality sampling networks, in *Proceedings of Computational Methods in Water Resources XIII, Vol. 1*, edited by L. R. Bentley, J. F. Sykes, C. A. Brebbia, W. G. Gray, and G. F. Pinder, pp. 579-585, A.A. Balkema, Rotterdam.

Hughes, J. P., and D. P. Lettenmaier (1981), Data requirements for Kriging: estimation and network design, *Water Resources Research*, 17, 1641-1650.

Izbicki, J. A., C. L. Stamos, and P. Martin (2004), Comparison of ground-water flow model particle tracking results and isotopic data in the Mojave River ground-water basin, southern California, USA, *Journal of Hydrology*, 292, 30-47.

James, B. R., and S. M. Gorelick (1994), When enough is enough: the worth of monitoring data in remediation design, *Water Resources Research*, 30, 3499-3513.

Knopman, D. S., and C. I. Voss (1989), Multiobjective sampling design for parameter estimation and model discrimination in groundwater solute transport, *Water Resources Research*, 25, 2245-2258.

Knopman, D. S., C. I. Voss, and S. P. Garabedian (1991), Sampling design for groundwater solute transport: tests of methods and analysis of Cape Cod tracer test data, *Water Resources Research*, 27, 925-949.

Kovar, K., A. Leijnse, G. J. M. Uffink, M. J. H. Pastoors, J. H. C. Mülschlegel, and W. J. Zaadnoordijk (2005), Reliability of travel times to groundwater abstraction wells: Application of the Netherlands Groundwater Model, LGM, Report 703717013/2005, RIVM, Bilthoven.

Loaiciga, H. O. (1989), An optimization approach for groundwater quality monitoring network design, *Water Resources Research*, 25, 1771-1782.

Maloszewski, P., and A. Zuber (1982), Determining the turnover time of groundwater systems with the aid of environmental tracers 1. Models and their applicability, *Journal of Hydrology*, 57, 207-231.

Manning, A. H., D. K. Solomon, and S. A. Thiros (2005), $^{3}H/^{3}He$ Age data in assessing the susceptibility of wells to contamination, *Ground Water*, 43, 353-367.

Massman, J., and R. A. Freeze (1987a), Groundwater contamination from waste management sites: the interaction between risk-based engineering design and regulatory policy. 1. Methodology, *Water Resources Research*, 23, 351-367.

Massman, J., and R. A. Freeze (1987b), Groundwater contamination from waste management sites: the interaction between risk-based engineering design and regulatory policy. 2. Results, *Water Resources Research*, 23, 368-380.

McDonald, M. G., and A. W. Harbaugh (1984), *A modular three-dimensional finite-difference ground-water flow model*, USGS, Reston.

McKinney, D. C., and D. P. Loucks (1992), Network design for predicting groundwater contamination, *Water Resources Research*, 28, 133-147.

Meyer, P. D., and E. D. Brill (1988), A method for locating wells in a groundwater monitoring network under conditions of uncertainty, *Water Resources Research*, 24, 1277-1282.

Meyer, P. D., A. J. Valocchi, and J. W. Eheart (1994), Monitoring network design to provide initial detection of groundwater contamination, *Water Resources Research*, 30, 2647-2659.

Nunes, L. M., E. Paralta, M. C. Cunha, and L. Ribeiro (2004), Groundwater nitrate monitoring network optimization with missing data, *Water Resources Research*, 40, W02406, doi:02410.01029/02003WR002469.

Pardo-Iguzquiza, E. (1998), Optimal selection of number and location of rainfall gauges for areal rainfall estimation using geostatistics and simulated annealing, *Journal of Hydrology*, 210, 206-220.

Pollock, D. W. (1994), User's Guide for MODPATH/MODPATH-PLOT, Version 3: A particle-tracking post-processing package for MODFLOW, the U.S. Geological Survey finite-difference ground-water flow model, Open-File Report, 94-464, U.S. Geological Survey, Reston.

Portniaguine, O., and D. K. Solomon (1998), Parameter estimation using groundwater age and head data, Cape Cod, Massachusetts, *Water Resources Research*, 34, 637-645.

Reilly, T. E., L. N. Plummer, P. J. Phillips, and E. Busenberg (1994), The use of simulation and multiple environmental tracers to quantify groundwater flow in a shallow aquifer, *Water Resources Research*, 30, 421-433.

Sheets, R. A., E. S. Bair, and G. L. Rowe (1998), Use of $^{3}H/^{3}He$ ages to evaluate and improve groundwater flow models in a complex buried-valley aquifer, *Water Resources Research*, 34, 1077-1089.

Simmons, C. S. (1982), A stochastic transport representation of dispersion in one-dimensional porous media systems, *Water Resources Research*, 18, 1193-1214.

Smethie Jr, W. M., D. K. Solomon, S. L. Schiff, and G. G. Mathieu (1992), Tracing groundwater flow in the Borden aquifer using krypton-85, *Journal of Hydrology*, 130, 279-297.

Solomon, D. K., R. J. Poreda, S. L. Schiff, and J. A. Cherry (1992), Tritium and Helium3 as groundwater age tracers in the Borden aquifer, *Water Resources Research*, 28, 741-755.

Storck, P., J. W. Eheart, and A. J. Valocchi (1997), A method for the optimal location of monitoring wells for detection of groundwater contamination in three-dimensional heterogeneous aquifers, *Water Resources Research*, 33, 2081-2088.

Stute, M., and P. Schlosser (2000), Tritium/^{3}Helium measurements as calibration tools in groundwater transport modelling, in *Tracers and Modelling in Hydrogeology*, edited by A. Dassargues, pp. 33-38, IAHS, Oxford.

Sumner, N. R., P. M. Fleming, and B. C. Bates (1997), Calibration of a modified SFB model for twenty-five Australian catchments using simulated annealing, *Journal of Hydrology*, 197, 166-188.

Szabo, Z., D. E. Rice, L. N. Plummer, E. Busenberg, and S. Drenkard (1996), Age dating of shallow groundwater with chlorofluorocarbons, tritium/helium 3, and flow path analysis, southern New Jersey coastal plane, *Water Resources Research*, 32, 1023-1038.

Tiedeman, C. R., D. M. Ely, M. C. Hill, and G. M. O'Brien (2004), A method for evaluating the importance of system state observations to model predictions, with application to the Death Valley regional groundwater flow system, *Water Resources Research*, 40, W12411, doi:12410.11029/12004WR003313.

Tiedeman, C. R., M. C. Hill, F. A. D'Agnese, and C. C. Faunt (2003), Methods for using groundwater model predictions to guide hydrogeologic data collection, with application to the Death Valley regional groundwater flow system, *Water Resources Research*, 39, 1010, doi:1010.1029/2001WR001255.

Valstar, J. R. (2001), Inverse modeling of groundwater flow and transport, Ph.D. Thesis, Delft University of Technology, Delft.

Valstar, J. R., D. B. McLaughlin, C. B. M. te Stroet, and F. C. van Geer (2004), A representer-based inverse method for groundwater flow and transport applications, *Water Resources Research*, 40, W05116, doi:10.1029/2003WR002922.

Wagner, B. J. (1995), Sampling design methods for groundwater modeling under uncertainty, *Water Resources Research*, 31, 2581-2591.

Wagner, B. J. (1999), Evaluating data worth for ground-water management under uncertainty, *Journal of Water Resources Planning and Management*, 125, 281-288.

Weissmann, G. S., Y. Zhang, and G. E. Fogg (2002), Dispersion of groundwater age in an alluvial aquifer system, *Water Resources Research*, 38, 1198, doi:1110.1029/2001WR000907.

Woodbury, A. D., and Y. Rubin (2000), A full-Bayesian approach to parameter inference from tracer travel moments and investigation of scale effects at the Cape Cod experimental site, *Water Resources Research*, 36, 159-171.

Wu, J., C. Zheng, and C. C. Chien (2005), Cost-effective sampling network design for contaminant plume monitoring under general hydrogeological conditions, *Journal of Contaminant Hydrology*, 77, 41-65.

Zhang, D. (2002), *Stochastic methods for flow in porous media: coping with uncertainties*, Academic Press, San Diego.

CHAPTER

4

Inverse modeling of multimodal spatial parameter distributions

Based on the paper published in *Water Resources Research*, **2006**

[Janssen, G.M.C.M., J.R. Valstar and S.E.A.T.M. van der Zee (2006), Inverse modeling of multimodal conductivity distributions, *Water Resour. Res.*, 42, W03410, doi:10.1029/2005WR004356.]

Presented at *FEM MODFLOW, International Conference on Finite Element Models, MODFLOW, and More: Solving Groundwater Problems*, Karlovy Vary, Czech Republic, **2004**

[Janssen, G.M.C.M., J.R. Valstar, S.E.A.T.M. van der Zee (2004) Inverse modelling of flow and transport through confining layers with multimodal hydraulic conductivity distributions. In: Kovar et al. (eds.), Proc. FEM_MODFLOW, International Conference on Finite Element Models, MODFLOW, and More: Solving Groundwater Problems, Karlovy Vary, September 13-16, 2004, pp. 77-80.]

4.1. Introduction

It is well-known that the subsurface, including the part relevant for groundwater flow and transport, exhibits a complex and heterogeneous architecture [*Bierkens*, 1994]. Consequently, so do many system parameters needed in distributed groundwater flow and transport models. The presence of multiple classes (e.g. lithologies, lithofacies) in the parameter fields of highly discretized groundwater models make that these parameter fields often cannot be well described by assuming a unimodal hydraulic parameter distribution: their probability distribution has a multimodal shape.

Whereas advanced geostatistical methods are available to generate multimodal realizations conditioned on static data (K, porosity etc.), the literature on the integration of state measurements (head, concentrations, travel time etc.) into the conditioning procedure is very limited for the bi- and multimodal cases. In its simplest form, calibration of multimodal spatial parameter fields is performed by regarding the spatial lithology distribution as known and fixed, thus merely calibrating the intra-lithology hydraulic parameters. An example of this method is given by *Hendricks Franssen and Gomez-Hernandez,* [2002], who used sequential self-calibration [*Gomez-Hernandez et al.*, 1998] for the inversion of the hydraulic conductivity distributions within fracture planes, treating each fracture plane as an independent statistical population. Another example is given by *Sun et al.* [1995], who expressed the hydraulic properties (K_H, K_V) belonging to every node in their model as a function of the (known) thickness distribution of the different lithologies identified within this nodes exclusive subdomain, and the (unknown but assumed constant) hydraulic conductivity $\boldsymbol{K}$ associated with these lithologies. Thus, they reduced the number of unknown parameters to the number of lithologies. In both works, however, the assumed geological structure (respectively, the fracture plane distribution and the lithofacies distribution) is conditioned on static data and not further updated using the state measurements.

Another approach is to only invert the lithology field. Methods for the inversion of Gaussian models can then be used, since lithology fields can be constructed using Gaussian methods. Following this line *Hu* [2000] used the Gradual Deformation method in combination with Gaussian Truncated Simulation to invert a binary lithology field. This method updates the lithology field by linearly combining either (in the first iteration) a random initial Gaussian field or (in subsequent iterations) the updated field from the

previous iteration, with a number of new and independent realizations. The contribution of every realization to the new, updated field is determined by an optimization search for the set of contribution coefficients that, after truncation of the Gaussian field, minimizes the objective function. Another application of Truncated Gaussian Simulation for the inversion of binary lithology fields is given by *Wen et al.* [2002], who use Sequential Self-Calibration for the calibration of the Gaussian field, through its relation with the actual conductivity field that is formed after its truncation. *Hu et al.* [2001a] proposed the use of Truncated Pluri-Gaussian Simulation [*Galli et al.*, 1994] for use in the Gradual Deformation approach for the inversion of multi-lithology fields (standard Truncated Gaussian Simulation is not generally suitable for the inversion of lithology fields with more than two soil types, as it can only produce outcrops in which the lithologies/facies are sequentially ranked [*Dowd et al.*, 2003]). *Liu and Oliver* [2004] used the Truncated Pluri-Gaussian Simulation method in a Bayesian scheme for conditioning the lithology distribution to a time series of dynamic data.

In principle, the calibration of the lithology distribution could be followed by filling the posterior lithology distribution with realizations of suitable parameter distributions per lithology, and calibrating these intra-lithology parameter fields while keeping the lithology field fixed. This would indeed yield a calibrated multimodal parameter field. True inversion of multimodally distributed spatial parameter fields would however somehow take the effect of the intra-lithology parameter variation on the residuals to be minimized into account during calibration of the parameter field. This means that we have to calibrate the spatial lithology distribution and the intra-lithology parameter distribution simultaneously. So, we have to treat the multimodal parameter distribution as a continuum, i.e. as one statistical population. This limits our possibilities, because many inverse algorithms fail for non-Gaussian models (like the multimodal problem at hand). For example, many Bayesian algorithms fail, due to the fact that in a model that is not (multi-)Gaussian, the decomposition of the posterior distribution in likelihood and prior, as stated in Bayes' Rule, cannot be performed analytically. Also standard Gradual Deformation fails, because the trick of linearly combining realizations only works for Gaussian models: in general, doing the same with non-Gaussian models will not preserve the non-Gaussian distribution [*Hu*, 2000].

Two important exponents of non- (or better: not necessarily-) Gaussian methods that are applied to high-dimensional spatial inverse problems can be mentioned: a) an extension of the Gradual Deformation Method to realizations generated by sequential simulation (GDSS) [*Hu et al.*, 2001b], and b) the Probability Perturbation (PP) method [*Caers and Hoffman*, 2006; *Caers*, 2007]. Both methods rely on sequential simulation to sample prior and posterior distributions. Sequential simulation requires sampling from local conditional cumulative distribution functions (ccdf's), which do not need to be Gaussian. The extension of the Gradual Deformation method (GDSS) makes a linear combination of two independent realizations of a random Gaussian process used to draw from the (ccdf's) during sequential simulation. The PP method basically optimizes the influence of the state observations on the local ccdf's by performing perturbations of the pre-conditionals (the ccdf's incorporating all but the state observations), performing a sequential simulation using the resulting ccdf's, and evaluating a model run with the result of this sequential simulation against the state observations.

However, when imposing and propagating the perturbations of either the local ccdf's (in PP) or the process of drawing from the ccdf's (in GDSS), it is not possible to preserve both the geostatistical properties of the lithology field as well as those of the intra-lithology parameters. The reason for this is that no spatial propagation model can be defined that captures all spatial dependencies in the multi-population parameter field.

In this Chapter, we will propose a simple methodology as a workaround for the above sketched problem of the inversion of continuous multi-lithology parameter fields. The methodology produces realizations of the multimodal parameter field that are conditioned on all static and state measurements, while the misfits between the calibrated model predictions and the measurements are reduced to the level of predefined measurement errors. Our method preserves the original geostatistics (i.e. those belonging to the indicator field as well as those of the intra-lithology or intra-facies parameter distributions), which in this work are assumed known. Calibration of the parameters of the geostatistical models is out of the scope of this Chapter.

In the following Sections, we first give an explanation of the concepts and mathematics involved in the developed inverse methodology. Then, we apply our ideas to a 2D synthetic example of a confining layer exhibiting a multimodal hydraulic conductivity (K) distribution. Using this synthetic example, we examine the applicability of our inverse

procedure, especially with regard to its ability to reproduce the original geostatistics. Throughout the Chapter the different statistical populations constituting the multimodal parameter distribution are referred to as lithologies. Of course, the reader could exchange this with lithofacies, facies, classes, et cetera.

4.2. Methodology

4.2.1. The key idea

The methodology we will present is a workaround for the difficulties existing inverse methods have with the multimodal distribution. The key idea is that, instead of proposing a completely new inverse algorithm, we transform the multimodal parameter field to the standard normal distribution. This puts existing inverse algorithms back in business. Subsequently, we tackle the problems caused by the transformation. These problems will be explained later.

The stochastic inverse algorithm that we applied is the representer-based inverse algorithm developed recently by *Valstar et al.* [2004], and we present the methodology for the calibration of multimodal parameter fields in conjunction with this inverse algorithm. Some aspects of the presentation of the methodology are therefore specific for the representer method. The general idea is, however, not restricted to any particular (class) of inverse algorithms.

4.2.2. Bayesian Framework: parameterization by representers

For completeness and for a good comprehension of the present study, we will here briefly recall the essence of the representer-based inverse method.

Consider the flow equation:

$$A(\alpha)h - q = 0 \qquad (1)$$

where h = the vector of nodal heads, q = the vector of driving forces, and $A(\alpha)$ = the system matrix depending on the parameters α. The representer method, as described in *Valstar et al.* [2004], searches for the maximum a posteriori estimates of these parameters α given observations of h. For a steady-state system, if all parameters α and

measurement errors *v* are assumed to be Gaussian distributed with known covariances and they are not cross-correlated, the maximum a posteriori estimate can be found by minimizing the following objective function:

$$J = (z - M(h))^T P_v^{-1} (z - M(h)) + (\alpha - \overline{\alpha})^T P_\alpha^{-1} (\alpha - \overline{\alpha}) \quad (2)$$

where J = the objective function value, z = the vector of measurement values, $M(\ )$ = a linear function that interpolates the vector of model predictions at the nodal points to the location of the measurements, α = the vector of parameters, $\overline{\alpha}$ = the prior mean of the parameters (in this study the unknown parameters are the hydraulic conductivities (K) assigned to the grid cells), P_v = the covariance matrix of the measurement errors v, and P_α = the prior covariance of the parameters. Multiplying the flow equation (Eq. (1)) with two times the head adjoint vector λ and adding this to the objective function (Eq. (2)) yields:

$$J = (z - M(h))^T P_v^{-1} (z - M(h)) + (\alpha - \overline{\alpha})^T P_\alpha^{-1} (\alpha - \overline{\alpha}) + 2\lambda^T \left[A(\alpha)h - q\right] \quad (3)$$

The addition of the flow equation to the objective function as a constraint allows for the parameters and heads to be treated independently, which has major computational advantages.

The objective function is minimized if the gradients of the objective function with respect to α, h and λ are zero. Forcing this on Eq. (3) yields a system of three coupled Euler-Lagrange equations (see Appendix). The solution of this system of equations gives the set of parameters α that minimizes the objective function. In order to decouple the Euler-Lagrange equations, the parameter and state variables are expressed as an expansion in a set of basis functions (see Appendix). Every measurement adds a term to this expansion, which consists of (i) a representer, quantifying the influence of the measurement on the estimates of the variable for which the expansion is defined; (ii) a representer coefficient, quantifying the weight given to the representer (which depends on the misfit between measurement value and measurement prediction).

By inserting the representer definitions in the Euler-Lagrange equations, explicit expressions for all representers and their coefficients can be obtained (see Appendix).

The adjoint head representer, the parameter representer and the head representer are calculated, respectively, in an iterative procedure, in which the unknowns in the representer expressions are replaced by their estimates from the previous iteration. Tlast step in each iteration is the calculation of the representer coefficients, which are actually the independent parameters of the inverse model. Since there is one representer coefficient for every measurement, the number of independent unknowns is reduced to the number of measurements.

4.2.3. Data Transformation and Backtransformation

In the unimodal case, the condition of normality of α in the Bayesian framework outlined above is usually obeyed by using the natural logarithm of K (LN(K)) for α, as previous research suggested that K values in the field exhibit a lognormal-like distribution [*Freeze*, 1975; *Hoeksema and Kitanidis*, 1985]. In the multimodal case, the condition of normality can be fulfilled by performing another, more complex transformation, relating the cumulative probability of the parameters to the cumulative probability density function (pdf) of the standard normal distribution.

The multimodal lognormal distribution function of the parameter K is described by:

$$p_K(K) = \sum_{i=1}^{N} \left[\frac{P_i}{K\sqrt{2\pi}\sigma_{LN(K_i)}} \exp\left(-\frac{\left(LN(K) - < LN(K_i) >\right)^2}{2\sigma^2_{LN(K_i)}} \right) \right] \quad , \quad 0<K<\infty \qquad (4)$$

where P_i, $\sigma_{LN(K_i)}$ and $<LN(K_i)>$ are the marginal probability and the standard deviation and mean value of LN(K) belonging to lithology i, respectively. N is the number of lithologies.

The corresponding cumulative distribution function (cdf) is then given by:

$$F_K(K) = \sum_{i=1}^{N}\left[\int_0^K \frac{P_i}{K\sqrt{2\pi}\sigma_{LN(K_i)}} \exp\left(-\frac{(LN(K) - < LN(K_i) >)^2}{2\sigma^2_{LN(K_i)}}\right) dK\right]$$

$$= -\sum_{i=1}^{N}\left[\frac{1}{2} P_i erfc\left(\frac{LN(K) - < LN(K_i) >}{\sigma_{LN(K_i)}\sqrt{2}}\right)\right] + 1 \qquad (5)$$

where *erfc* is the complementary error function. The Gaussian deviate of *K*, denoted α, can then be found by equating the cumulative probability of *K* with the cumulative probability of the cdf of the standard normal distribution:

$$F_\alpha(\alpha) = \frac{1 + erf\left(\frac{\alpha}{\sqrt{2}}\right)}{2} \qquad (6)$$

where *erf* is the error function.

As $F_K(K)$ is known from Eq. (5), α can be calculated using the inverse of the cumulative standard normal distribution function. The transformation procedure is illustrated in Figure 1.

The backtransformation of α can be achieved with a hybrid Newton-Raphson/Bisection root finding algorithm [*Press et al.*, 1986] to look for the value of *K* that equates Eq. (5)

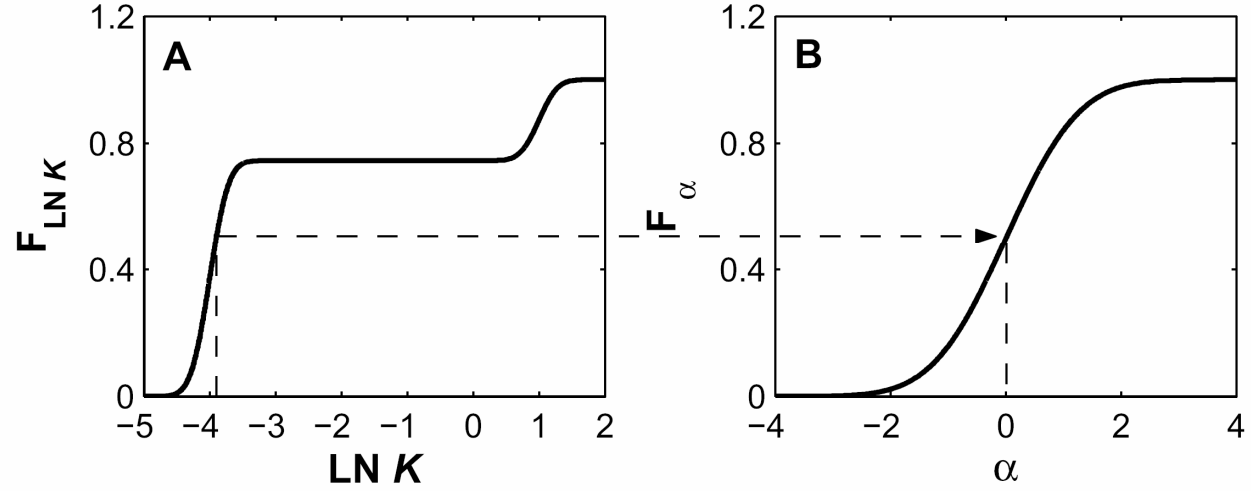

Figure 1. Illustration of the data transformation procedure, from F_{LNK}, the cumulative probability function of LN *K* (a), to F_α, the cumulative probability function of α (b).

with Eq. (6). The derivative of K with respect to α, needed for the Newton-Raphson algorithm and also for the evaluation Eq. (A9), is given by:

$$\frac{dK}{d\alpha} = \frac{p_\alpha(\alpha)}{p_K(K)} \tag{7}$$

The property formalized in Eq. 7 makes that the proposed transformation is easy to implement in existing inverse algorithms.

4.2.4. Prior fields

In this Chapter, two different types of calibration are performed: calibration starting from a homogeneous prior field and Monte Carlo calibration of heterogeneous prior fields. In our case of multimodal conductivity distributions both require a very different approach.

Calibration starting from homogeneous prior fields can serve, for example, as a quick assessment of system response (conditional to the available measurements), the systems posterior covariances of the parameters and states, and its sensitivities [*Valstar*, 2001; *Valstar et al.*, 2004]. Only one realization has to be calibrated, and therefore this approach may enjoy preference over (usually) time-consuming Monte Carlo runs. The representer method allows for the calculation of the posterior parameter and state variances by applying a linearization around the last estimates [*Valstar*, 2001; *Valstar et al.*, 2004], and these posterior variances can be used, for instance, to guide future measurement campaigns.

More challenging than the calibration of initially homogeneous fields, where no reproduction of the reference geostatistics is pursued, is the inverse modeling of heterogeneous multimodal prior fields. This is necessary if, for example, a realistic system representation is needed or if one wants to quantify the inherent uncertainty in model predictions made with a model in which the linearization assumption is not valid. In that case, a Monte Carlo analysis has to be performed, which means that a large number of unconditional realizations that obey the reference statistics are calibrated into equiprobable realizations that still obey the reference statistics but are now also conditional to all measurements.

If, however, a heterogeneous, multimodal realization is calibrated with the procedure described above, the resulting calibrated realization will not obey the reference geostatistics. This is the case because the *α*-variogram is a composite variogram constructed from *N*+1 different covariance functions *C*: C_i, (i = 1,2 …*N*) and C_I (*I* stands for Indicator). Since the variance gain over a certain lag distance can never be the exact representation of the variance gain of more than one variable, information is always lost when variograms are combined. The *N*+1 separate variograms can therefore (after backtransformation) never be reproduced when the *α*-variogram is used for simulation. Furthermore, simulation using the *α*-variogram induces cross-correlation between the intra-lithology *K* distributions that was originally not there.

As a solution. we have designed an iterative posterior conditioning procedure that preserves the original correlation structure of the indicator field. As the method is better explained using a specific numerical example, its details will be discussed in Section 4.3.5.

4.3. Simulation

4.3.1.Conceptual Model

We considered the synthetic example of a 2D complex confining layer of 500 (length) by 20 (depth) m, discretized into 250 × 40 elements. Only the hydraulic conductivies to be assigned to the cells of this confining layer are assumed unknown. Thus, the number of parameters to be estimated is 10^4. On top of the confining layer we assumed a homogeneous sandy layer of anthropogenic origin with a thickness of 3 m (discretized into 250 x 1 elements) and a known hydraulic conductivity of 3.0 m/d, and underneath the confining layer we assumed a sandy aquifer with a thickness of 10 m (discretized into 250 x 1 elements) and a known value for K of 0.6 m/d.

A steady-state head distribution was obtained with MODFLOW [*McDonald and Harbaugh*, 1984] by assigning recharge (250 mm/y) to the top of every top layer grid cell and by imposing constant heads of 0.0 m and 2.0 m in the utmost left and utmost right cell of the aquifer layer, respectively. A schematic representation of the flow model is given in Figure 2.

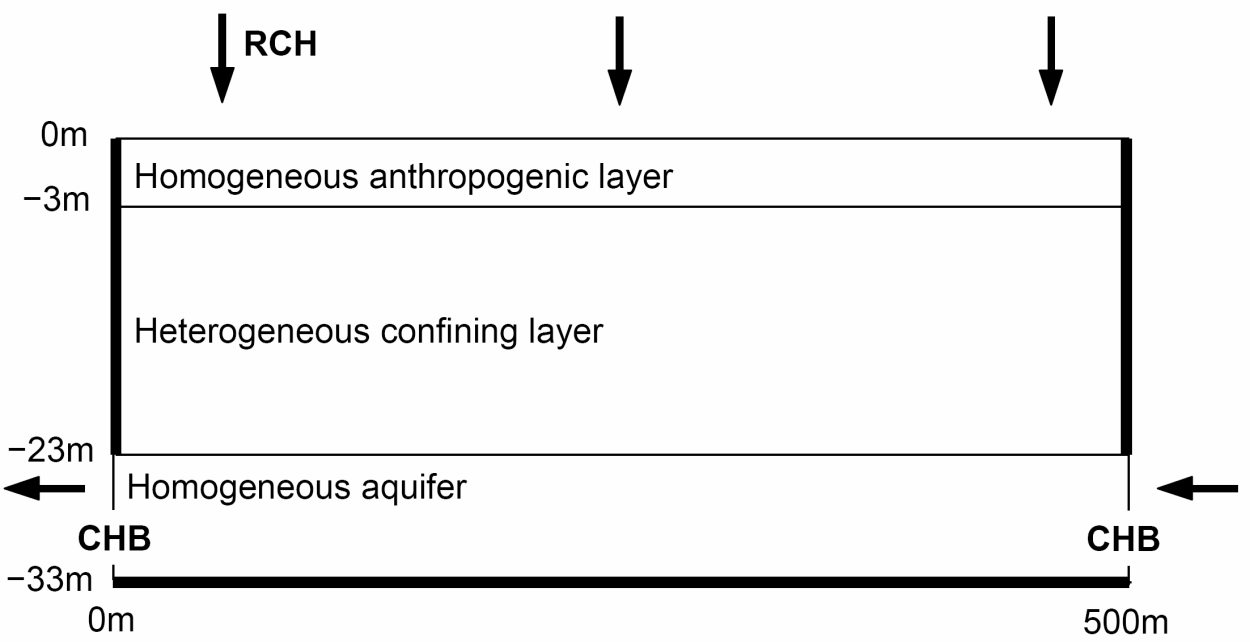

Figure 2. Schematic representation of the flow model. Bold border lines indicate no-flow boundaries. Arrows indicate water sources and sinks. CHB = constant head boundary. RCH = Recharge.

4.3.2. Reference confining layer and reference geostatistics

The measurements with which the calibrations in this study were performed were obtained from a bimodal as well as a trimodal synthetic reference (or "true") field. These reference fields were constructed in two steps: first, an unconditional two-class (or three-class) indicator field $I(\mathbf{x})$ ($\mathbf{x}(x_1,x_2)$ is the vector of Cartesian coordinates, I = 1,2 or 3) was generated with the GSLIB program SISIM [*Deutsch and Journel*, 1998]. Then, using the GSLIB program SGSIM, an intra-lithology hydraulic conductivity distribution was generated for every lithology type ($Y_i(\mathbf{x})$ = LN($K_i(\mathbf{x})$), i = 1, 2 or 3). The intra-lithology K distributions were combined into one continuous bi- or trimodal realization of $K(\mathbf{x})$ according to the indicator field ($K(\mathbf{x}) = K_i(\mathbf{x})$ if $I(\mathbf{x})$ = i). The properties of the indicator fields and the continuous intra-lithology distributions are given in Table 1. The reference indicator fields are shown in Figure 3.

Table 1. Geostatistics of the unconditional indicator fields, continuous fields and the transformed fields. Numerical subscripts indicate lithologies. Subscript H stands for the horizontal direction, subscript Z for the vertical direction. (*) Only given for the bimodal case.

Parameter	Value
Indicator Fields	
P_1 for Bimodal case	0.75
P_2 for Bimodal case	0.25
$P_1 = P_2 = P_3$ for Trimodal case	0.33
$a_{H,1}$ (m) = $a_{H,2}$ = $a_{H,3}$	100.0
$a_{Z,1}$ (m) = $a_{Z,2}$ = $a_{Z,3}$	10.0
Variogram model	Exponential
Continuous Fields	
$<Y_1>$ (LN(m/d))	-4.0
$<Y_2>$ (LN(m/d))	1.0
$<Y_3>$ (LN(m/d))	-2.0
$\sigma^2_{Y_1}$ (-) = $\sigma^2_{Y_2} = \sigma^2_{Y_3}$	0.05
a_{H,K_1} (m)	20.0
a_{Z,K_1} (m)	3.5
a_{H,K_2} (m) = a_{H,K_3}	10.0
a_{Z,K_2} (m) = a_{Z,K_3}	3.0
Variogram model	Exponential
"Equivalent" Unimodal Fields*	
$<Y>$ (LN(m/d))	-2.75
σ^2_Y (-)	4.74
Variogram model	Eq. 9
Transformed Fields	
$<\alpha>$ (-)	0.0
σ^2_α (-)	1.0
$a_{H,\alpha}$(m) Bimodal / Trimodal	78.01 / 84.00
$a_{Z,\alpha}$(m) Bimodal / Trimodal	8.30 / 9.50
$w_{H,\alpha}$ Bimodal / Trimodal	0.67 / 0.83
$w_{Z,\alpha}$ Bimodal / Trimodal	0.73 / 0.78
Variogram model	Eq. 8

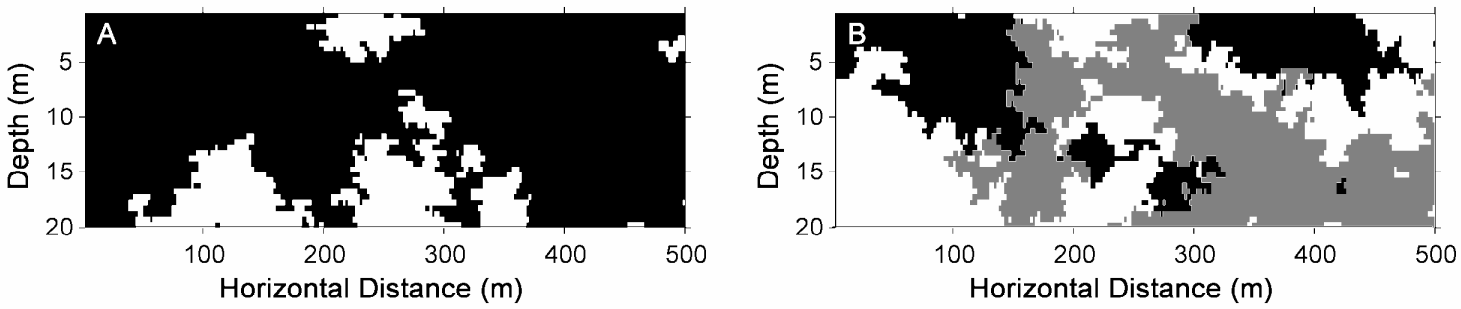

Figure 3. Reference lithology fields for the bimodal (a) and trimodal (b) case.

When transforming a multimodal lognormal hydraulic conductivity field into a standard normally distributed one, its original geostatistical structure will be lost. In the first place, the transformed field, being standard normally distributed, will always have a mean and sill of approximately 0.0 and 1.0, respectively. Furthermore, the horizontal (a_H) and vertical (a_Z) ranges change. Finally, also the type of variogram (the variogram model) that applies for the transformed field differs from the one for the multimodal lognormal field.

To obtain the parameter covariance matrix (P_α in Eq. (2)) of the transformed field, 5000 unconditional, equiprobable realizations of the confining layer with the same geostatistical properties as the reference confining layer were generated. These realizations were then transformed according to the transformation procedure described above. Using a modified version of the GSLIB program GAM [*Deutsch and Journel*, 1998], the average horizontal and vertical variogram of all transformed realizations were calculated, constituting P_α.

Table 1 gives the geostatistical parameters for the transformed fields as they resulted from this multi-realization approach. It appeared that for both the bi- and the trimodal case, the variograms could be described very well with the following model:

$$\gamma(s) = c \cdot \left[1 - \exp\left(-\frac{3s^w}{a^w} \right) \right] , \qquad (8)$$

where γ = the variance, c = the sill, s = the lag distance, w is a constant ($w < 1$), a is the effective range and a^w is the actual range. Note that not only a but also w is different for the two principal directions. *Wingle and Poeter* [1998] presented a kriging method that can handle different variogram models in the different principal directions, and this is the method applied for this study.

Throughout the rest of this chapter, the statistics given in Table 1 for the untransformed fields will be referred to as the "reference geostatistics".

4.3.3. Measurement sets

In the reference field, 36 measurement locations were selected according to a regular grid. Different subsets of these measurement locations were used as input for the calibration procedure: we used subsets of 12, 18, 24 and 36 head measurements and equally sized subsets of *K* measurements. In the following, measurement sets will be referred to with a code consisting of the number of measurements of each type. For example, a measurement set with 18 head and 18 *K* measurements is indicated as the 18H18*K* measurement set. The locations sampled in the various subsets are given in Figure 4. This figure holds for both head and *K* measurements (so a subset of *K* measurements consists of the same measurement locations as the equally sized subset of head measurements).

Gaussian-distributed synthetic measurement errors were added to the head measurement values to account for their uncertainty: a measurement error variance of 0.001 m^2 was assumed. The method of incorporation of *K* measurements in the calibration procedure depended on whether a homogeneous prior field was being calibrated (Section 4.3.4) or a heterogeneous prior field in a Monte Carlo series (Section 4.3.5). In the first case, actual continuous *K* measurements were sampled from the reference field and transformed to α, and a measurement error was added to them. A measurement error standard deviation of 20 and 10 percent of the mean *K* value of the corresponding lithology was assumed for *K* measurements that fell into the low and high conductivity category, respectively. Note that the measurement variance P_{ij} (i = j) that has to be applied to α is dependent on the value of α. In the Monte Carlo series, only the lithology type was extracted from the reference field at the measurement locations, and

this information was incorporated in the calibration procedure by conditioning the prior indicator fields on it. This point is explained further in Section 4.3.5.

The measurement information, together with the reference geostatistics, was assumed to be the only prior information available about the true hydraulic conductivity field.

4.3.4. Calibration of homogeneous prior fields

We performed this type of calibration only for the bimodal case. The absence of prior knowledge about the distribution of the parameter α over the domain was expressed by setting it at its mean value (α = 0.0) everywhere. For the bimodal case, this value of α corresponds to K = 0.06 m/d. The calibration was performed with both the 36H and the 18H18K measurement set.

For illustrative purposes, the calibration calculations were repeated using a unimodal approach, an approach a modeler inadvertently could choose if he fails to recognize the existence of multiple statistical populations of K. The bimodal nature of K is then replaced by the normal distribution with the same overall mean and variance. The covariance function that is now needed to describe the composite geostatistical

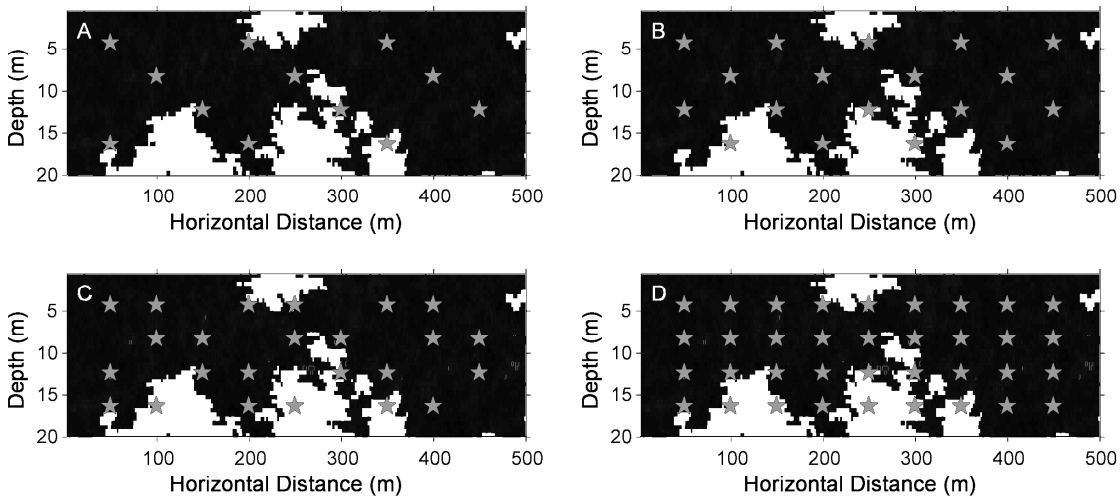

Figure 4. Configuration of the 12H (a), 18H (b), 24H (c) and 36H (d) measurement sets, which are identical to the 12K, 18K, 24K and 36K measurement sets, respectively.

properties (see Table 1) and to fill P_α can be obtained using the analytical result presented by *Rubin* [1995], *Lu and Zhang* [2002] and *Rubin* [2003]:

$$C(s) = \left(P_1^2 + C_I(s)\right)C_1(s) + \left(P_2^2 + C_I(s)\right)C_2(s) + C_I(s)\left(< Y_1 > - < Y_2 >\right)^2 \quad (9)$$

where C_1, C_2, C_I and C are the two intra-lithology covariance functions and the indicator and composite covariance functions, respectively.

4.3.5. Calibration of heterogeneous prior fields

As stated above, the transformation procedure and therefore also the calibration procedure destroy the reference geostatistics. An example of a posterior field calibrated on the 24H measurement set, together with the average horizontal prior, theoretical and posterior indicator variograms averaged over an ensemble of 100 posterior realizations conditioned on the same measurement set, is given in Figure 5. It is clear that the integral scales of the lithology field are severely underestimated. However, the calibrated field *does* give information on where the inverse algorithm wants to decrease the amount of one lithology in favor of another. This information can be used in an iterative posterior conditioning procedure that iteratively results in a conditional realization that

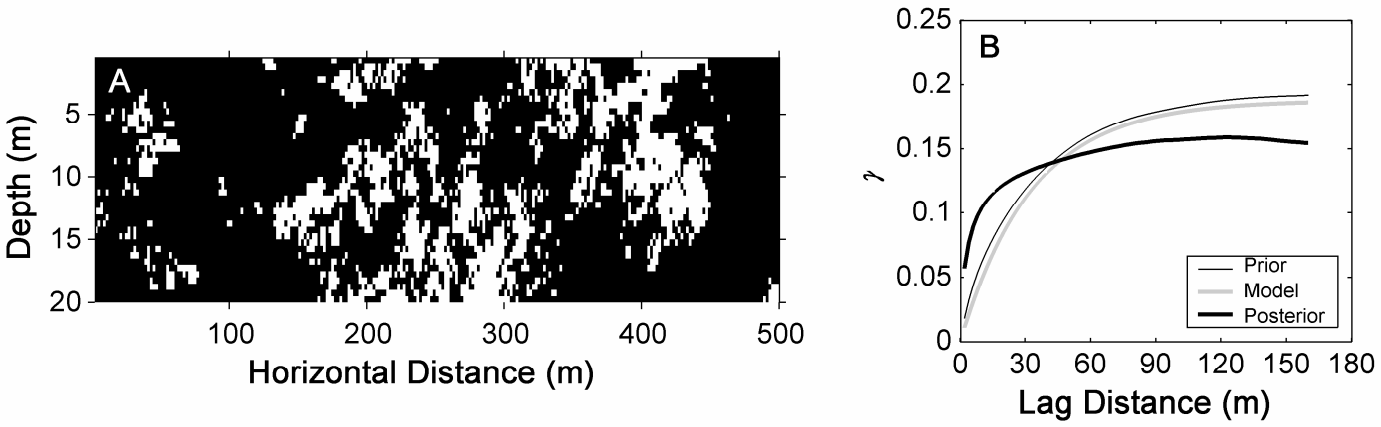

Figure 5. Example of a calibrated lithology field before posterior conditioning (a) and the horizontal prior, theoretical and posterior indicator variograms averaged over 100 posterior realizations (also without posterior conditioning)

obeys the reference geostatistics. Incorporating this posterior conditioning procedure, the complete flow chart of a multimodal prior parameter field calibration consists of the following steps:

1) Generate an indicator field that is conditional to the available hard data (if any) and that obeys the reference geostatistics (with SISIM);

2) Generate (in this study unconditional) K_i (i = 1,2…*N*) fields (with SGSIM) and combine them according to the indicator field;

3) Calculate the objective function (this objective function is discussed below);

4) Calibrate the resulting bimodal realization using the methodology described above (the use of the representer method is however a matter of choice: also other inverse methods can be used). Note: this step results in fields with distorted geostatistics, as the field shown in Figure 5a;

5) Determine which cells in the model have *not* changed lithology during the calibration;

6) Generate (with SISIM, using the reference geostatistics) a new indicator field conditioned on the cells that have *not* changed lithology and on the available *K* measurements (if any);

7) Repeat steps 2-6 until the objective function in step 3 meets a certain convergence criterion (this convergence criterion is discussed below);

8) Combine the resulting lithology field with the initial K_i (i = 1,2…*N*) fields (from the first time that step 2 was executed);

9) Calibrate the intra-lithology hydraulic conductivity distribution.

Steps 5 and 6 constitute the proposed posterior conditioning procedure. Step 7 is referred to as the *outer* iteration loop of the calibration, to distinguish this iteration loop from the iterations performed in the calibration of the transformed field (step 4). These are referred to as *inner* iterations (in this study these are the iterations of the representer method).

The objective function evaluated in step 3 (the objective function for the outer iterations) differs from the objective function used in the representer method for the inner iterations (see Appendix). The evaluation of the objective function used in the representer method requires the calculation of the representer expansions, which can only be done for the transformed field. Instead, we simply used a least-squares objective function in step 3,

summing, over all measurements, the squared differences between the measurement value and the model prediction. The value of the convergence criterion, with which the value of the objective function in step 3 is compared, was calculated as follows:

$$C_{crit} = N_{meas} \cdot V_{\mathrm{H}} + \sum_{\mathrm{m}=1}^{N_{meas}} \sigma_{\mathrm{H,m}}^2 \qquad (10)$$

where N_{meas} is the number of measurements, V_{H} is the head measurement error variance (= constant for all head measurements), and $\sigma_{\mathrm{H,m}}^2$ is the head variance at measurement location m assuming a fully known spatial lithology distribution and a completely unknown intra-lithology K distribution. Thus, the first part of the right-hand side of Eq. (10) accounts for the measurement errors, which allow a certain deviation of the model predictions made with the calibrated realization from the measurement values. The second part of the right-hand side reflects the variance that can be resolved by calibrating the intra-lithology hydraulic conductivity distributions, after an appropriate lithology distribution has been found. So, this variance does not have to be resolved during the calibration of the lithology distribution. An approximate value for $\sigma_{\mathrm{H,m}}^2$ was obtained by calculating the average squared difference between the reference head value at the measurement location and the head value at the same location in 100 realizations having the reference lithology distribution but varying K_{i} (i = 1,2…N) realizations. Needless to say that this convergence criterion only works for a synthetic calibration case.

The maximum number of inner iterations allowed in step 4 (iterations of the representer-based inverse method) was set at 10. Due to the high nonlinearity of the problem, it happened occasionally that convergence was not reached after 10 iterations, or that the calibration got stuck in a local minimum. However, even fields that are not fully calibrated, or fields trapped in a local minimum, contain information about necessary parameter adjustments. Therefore, in such situations, the algorithm was set to proceed as usual to step 5.

In step 5, the lithology distribution has to be regained from the continuous α-distribution. This was done by backtransforming α to K as explained in Section 4.2.3, and then appointing threshold values of K to distinguish between the lithologies. The threshold

between two lithologies was set at the value of K (between the two mean values of the lithologies) with the lowest probability. Considering the small intra-lithology variances and the high contrasts between the mean K values of the lithologies, the probability of assigning the wrong lithology type to a certain value of α was extremely low and did not hamper the calibration (in terms of reproduction of geostatistics).

Advancing in the outer iteration loop, the number of conditioning cells used in step 6 grows, thereby more and more fixing the newly generated indicator field and limiting the variation that induces progression in the convergence. This can cause the convergence to stop preliminarily. Therefore, in runs in which it was found necessary to promote the convergence speed, the new indicator field generated in step 6 was simulated with the Kriging of the unknown cells based on only a very small number of previously simulated nodes (the value of *nodmax* in SISIM was set at 2). This reduces the influence of the conditioning cells on the simulation of the unknown cells, and thus more variation is created in the simulation of these cells. We applied this technique in case both the number of outer iterations was larger than 10 and the objective function was still larger than 50% of its original value.

In step 2, new K_i (i = 1,2…N) fields were generated with a randomly sampled value for the seed in every iteration. This was found necessary for preserving the reference lithology geostatistics, for the following reason. A cell that has not changed lithology during a certain outer iteration, is not likely to change lithology in upcoming outer iterations either if the prior intra-lithology K distribution with which the calibration in step 4 starts remains the same: the influence of the measurements on the parameter value of this cell (quantified in the parameter representer of this cell) will not change much, leave alone that it changes sign. This means that, once a cell has been added to the conditioning file (an input file for SISIM with all conditioning cells) used in step 6, it is unlikely to be removed from this file during following outer iterations. After every outer iteration, cells are added to this conditioning file, and they are there to stay. The set of permanent conditioning cells grows fast, and moreover, as in every outer iteration the prior indicator field they originate from is different, this set does not obey the correct indicator variogram. Thus, the new indicator field generated in step 6 will be increasingly distorted.

If, however, the intra-lithology *K* distributions that enter step 4 is changed in every iteration, only those cells that do not change lithology in step 4 regardless of this intra-lithology *K* distribution, become part of the subset of permanent conditioning cells. Changing the intra-lithology *K* distributions significantly changes the parameter representer field, which can make conditioning cells change lithology again and thus leave the conditioning file. The subset of permanent conditioning cells still does not obey the correct variogram (they still originate from a combination of prior indicator fields), but their number increases much slower. In other words: the spatial density of the new members to the permanent subset of conditioning cells added per outer iteration, is insufficient to adversely affect the spatial indicator correlation in a significant extent. The indicator simulation can incorporate them while honoring the imposed variogram.

The set of remaining (non-permanent) conditioning cells changes from iteration to iteration and therefore its disturbing influence on the variogram of the newly generated indicator field in step 6 will not increase, but instead is corrected during outer subsequent iterations.

The calibration of the intra-lithology *K* distributions (step 9) was performed using the representer method, assuming zero correlation between cells that have a different lithology, and using the appropriate intra-lithology geostatistics to calculate the covariance between cells that have the same lithology.

4.4. Results

4.4.1. Calibration of homogeneous prior fields

Figure 6 shows the reference and the prior head distribution within the confining layer. The prior field shows a regular head fall from the upper right corner of the domain to the lower left corner, where the head was preset at 0.0 m. The reference head field, however, shows considerable deviations from this regular pattern, especially at the locations of the high-conductivity lenses which locally cause the flow to be more horizontally directed than in the prior, homogeneous field.

The head and *K* fields calibrated on the 36H measurement set with the unimodal and the bimodal approach, are given in Figure 7. Although both calibration approaches yielded head distributions that fit the head measurements equally well, the head fields and the calibrated K fields produced by them are clearly very different in nature. In the unimodal approach, posterior parameter variance was much smaller than the input variance (see Figures 7c and 7e): although the input variance $\sigma^2_{\mathrm{LN}(K)}$ of the unimodal approach was 4.74, the posterior value of $\sigma^2_{\mathrm{LN}(K)}$ was only 0.49. This resulted in a head field (Figure 7a) that is still rather smooth compared with the reference head field. In contrast, the bimodal calibration approach yielded a much more "realistic" *K* field (Figures 7d and 7f), with two distinct lithologies just as in the reference field. Both the unimodal and the

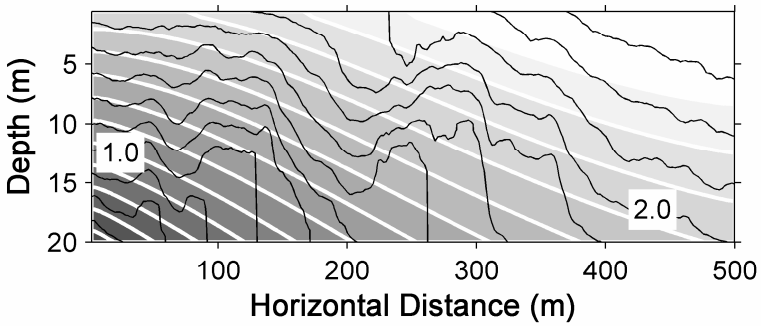

Figure 6. A comparison, for the bimodal case, between the reference head distribution (black lines) and the prior head distribution (white lines and gray scale) calculated from the homogeneous prior field.

bimodal approach predicted the high-conductivity zones at the correct locations (the locations of the sand lenses in the reference field), but only in the bimodally calibrated *K* field the difference between the high and low conductivity zones are as pronounced as in the reference field. Therefore, the posterior head field of the bimodal approach (Figure 7b), although equally close to the measurement values, exhibits an overall pattern that resembles the reference head field much better than the posterior head field of the unimodal approach. Especially the horizontally directed flow at the locations of the high-conductivity lenses is much better predicted. We also obtained the conditioned travel times needed for particles released in the top cell of every column in the numerical

model to reach the lower aquifer, using the particle-tracking software MODPATH [*Pollock*, 1994]. Figure 8 illustrates that the bimodal approach also results in a major improvement of the transport predictions.

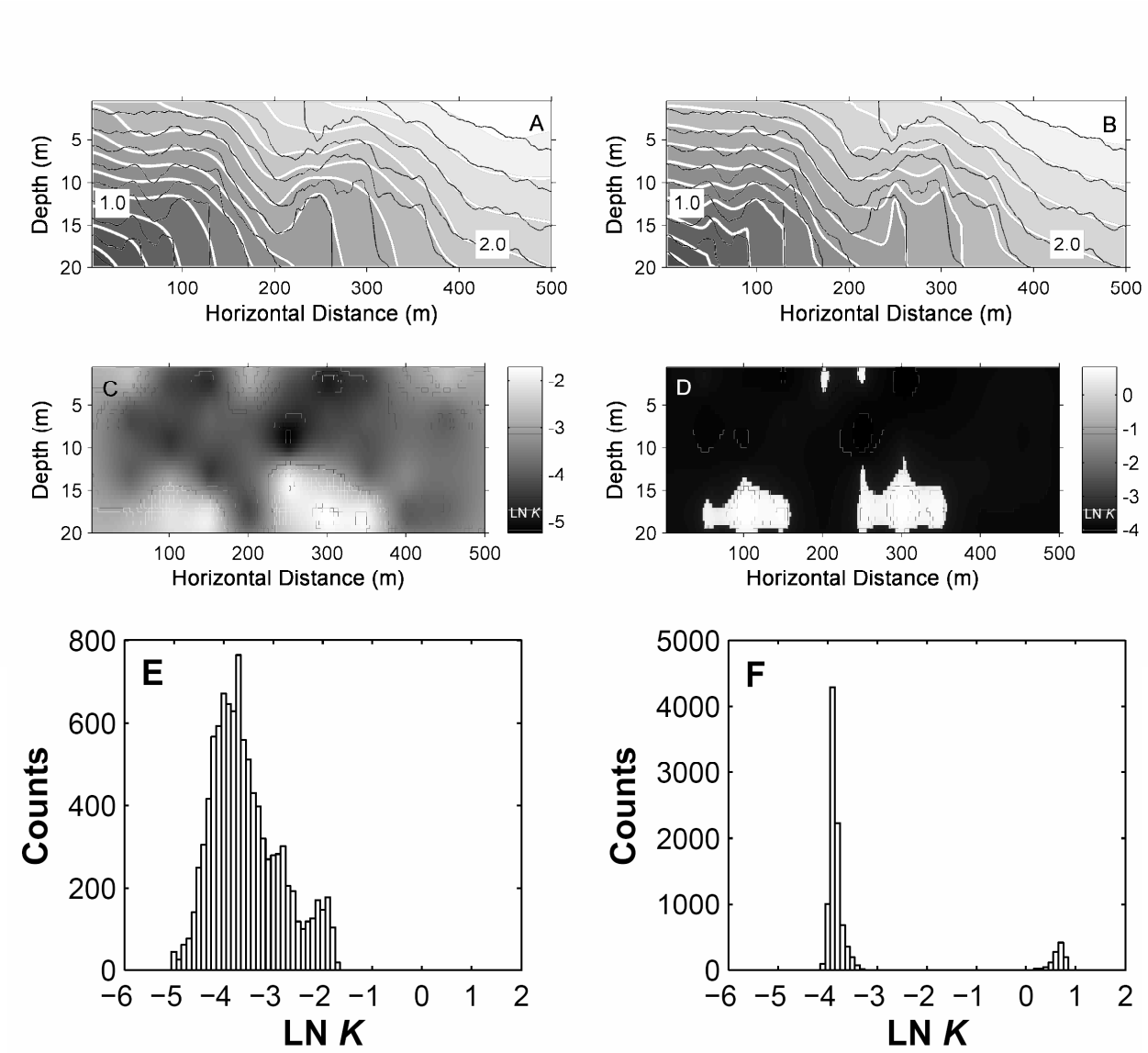

Figure 7. Calibration results obtained with the unimodal (a, c, and e) and the bimodal approach (b, d, and f). Figures 7a and 7b compare the calibrated head fields (white lines and gray scale) with the reference head distribution (black lines). Figures 7c and 7d show the calibrated LN *K* distributions.

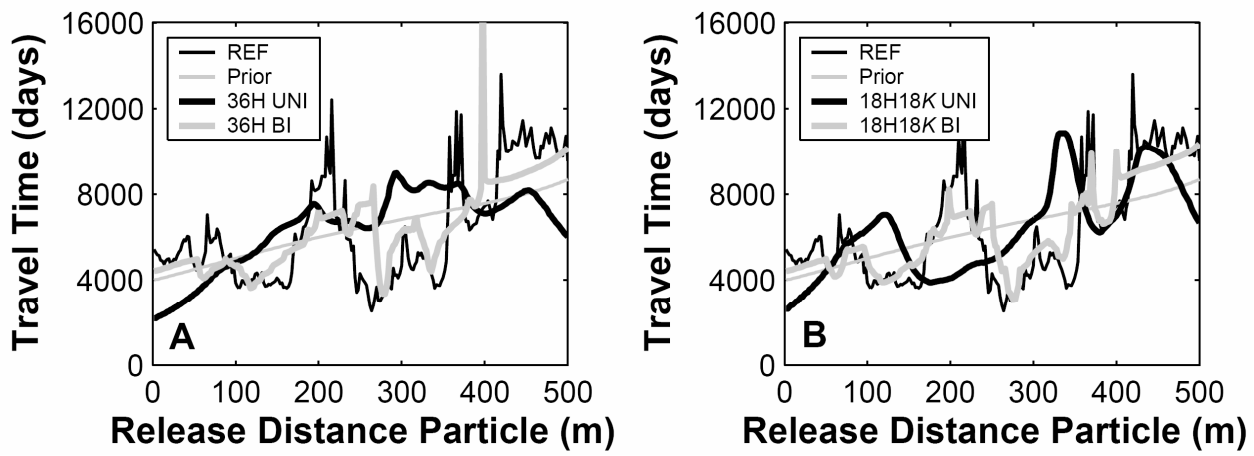

Figure 8. Unconditional ("Prior") and conditional (to the 36H (a) and the 18H18*K* (b) measurement set) travel times needed for particles starting from the top of the anthropogenic layer to reach the groundwater layer, compared with the reference ("REF") travel times. "UNI" = unimodal approach, "BI" = bimodal approach.

4.4.2. Calibration of heterogeneous prior fields

For the calibration procedure outlined in Section 4.3.5 to succeed (that is, to result in equiprobable realizations obeying the reference geostatistics and conditional to all the measurements) it is crucial that during the calibration in step 4 of the calibration flow chart (Section 4.3.5) the properties of α (specifically the shape of its distribution and its variogram) are preserved. Otherwise, a bias will be introduced that will propagate through the iterative posterior conditioning procedure (the outer iterations). Figure 9a shows, for the bimodal case, the α-histogram of 200 Monte Carlo realizations calibrated (without posterior conditioning) with the representer method, starting from random continuous bimodal fields and using the 24H measurement set. This histogram is compared to the theoretical histogram defined by the standard normal distribution. To exclude the influence of the reference field on the posterior histogram (which would result in a systematic bias), every unconditional realization from the Monte Carlo series was calibrated using measurements taken from a different reference field. Whereas the prior distribution of α matched the theoretical distribution almost perfectly (data not shown), the calibration introduces a minor bias of α towards values that are close to the lithology threshold (α = 0.675). It is conceivable that this is due to the extremely high value of the derivative dK/dα at this threshold, which can trick cells into an unjustified

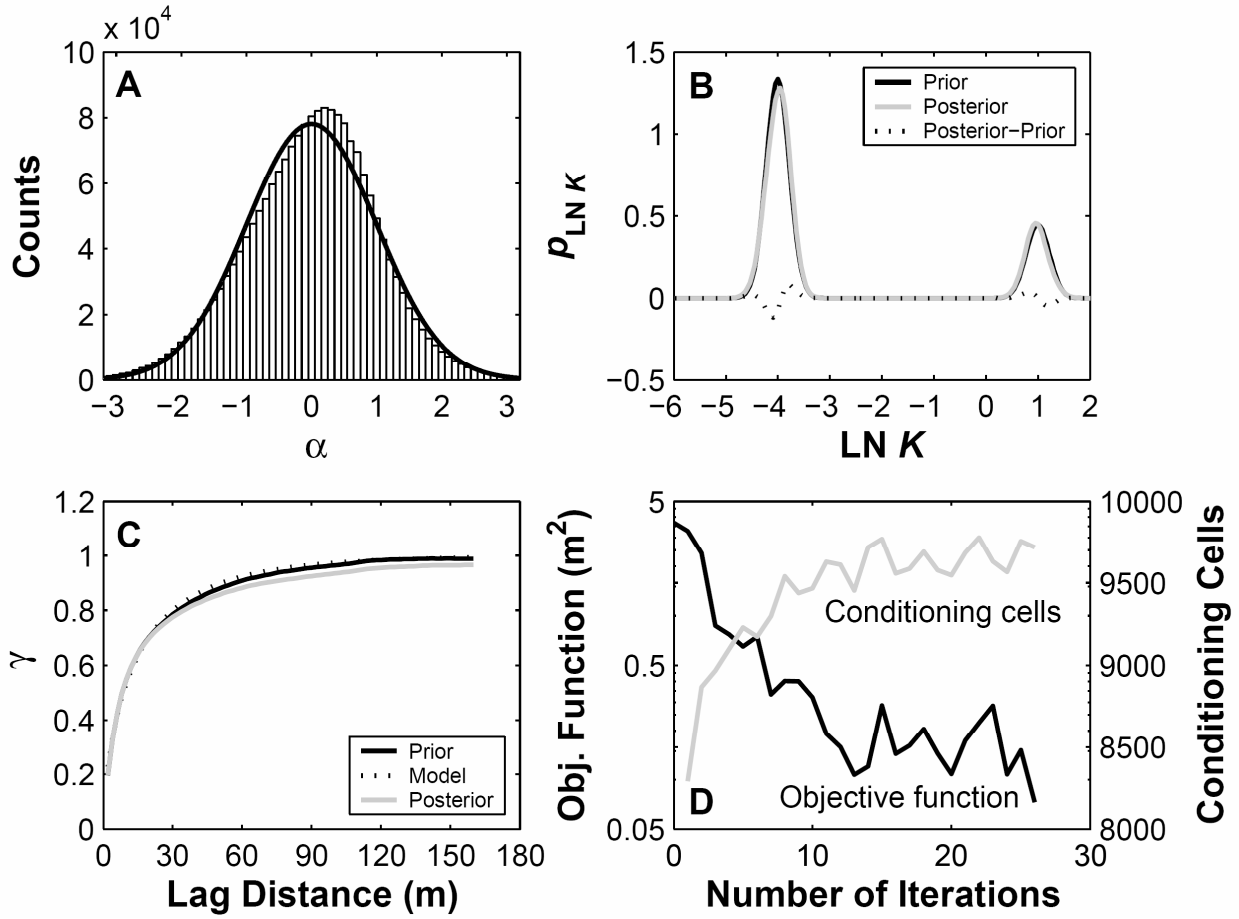

Figure 9. (a) Comparison of the posterior α histogram with the theoretical variogram as given by the standard normal distribution (black line). (b) Comparison between the prior and posterior LN K distributions. The dotted line gives the numerical difference between the two. (c) Comparison of the averaged posterior α variogram with the averaged prior and model variogram. (d) Example of the development of the objective function (logarithmic scale) during the calibration of one specific multimodal field, together with the development of the number of conditioning cells used in step 6 of the calibration flow chart (see Section 4.3.5).

lithology switch. In later iterations, this switch will sometimes not be completely undone anymore, but only partially by moving the α-value of this cell close to the threshold value. However, after backtransformation of the values with which the α-histogram was constructed, this bias appears not to affect the relative proportions of the two lithologies, and it only has an insignificant effect on the shape of the intra-lithology hydraulic conductivity probabilities (see Figure 9b).

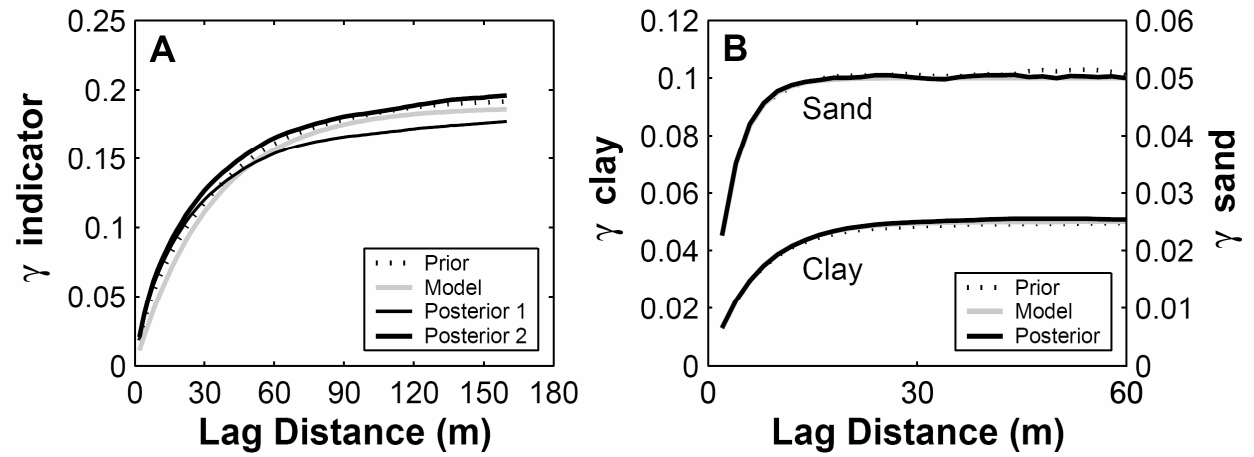

Figure 10. (a) Comparison of the posterior indicator variograms, both averaged over all posterior realizations ("Posterior 1") and averaged over only those realizations, the calibration of which did not require adjustment of *nodmax* ("Posterior 2"), with the averaged prior indicator variogram and the model variogram. (b) Comparison of the averaged posterior intra-lithology variogram with the averaged prior and model variogram.

Except for a minor reduction of the sill variance due to the small bias discussed above, the horizontal α-variogram is preserved well after calibration (see Figure 9c): the range and the model type are unaffected. The reproduction of the vertical α-variogram was equally good. In summary, Figure 9 shows that the representer method is able to handle the calibration of the normal transform of a bimodal variable in a satisfactory manner, despite of the difficulties that were to be expected because of the very high value of $dK/d\alpha$ at the threshold value of α.

Figure 9d shows, for one particular initial realization in this Monte Carlo run, the development of the objective function as evaluated in step 3 of the calibration flow chart, as well as the number of conditioning cells used in step 6 to generate the next lithology field.

Decisive substantiation of the proposed method for the calibration of continuous multimodal fields is achieved if the average statistical properties of a sufficient number of conditional realizations are shown to be close to the reference statistics. To this aim, 100 unconditional random continuous bimodal realizations were calibrated on the 24H measurement set, again using a different reference field for every realization to be calibrated. This number of Monte Carlo calculations appeared to be enough to achieve

convergence of the results (average variograms). Figure 10a shows a comparison between the horizontal indicator variogram modeled using the reference statistics (see Table 1) and the averaged prior and posterior (line "Posterior 1") horizontal indicator variogram. It shows that during calibration, the prior indicator variogram is preserved reasonably well. The small deformation of the variogram is caused by lowering *nodmax* in SISIM in slowly converging realizations (see §3.5): the average posterior variogram of the 51 (out of 100) realizations that did not require lowering *nodmax* in their calibration (line "Posterior 2" in Figure 10a) resembles the prior variogram very well. Equally good results were found for the vertical indicator variogram.

After the convergence criterion for the calibration of the lithology distribution was met, the intra-lithology hydraulic conductivity distributions were calibrated (step 9 in Section 4.3.5). For all 100 Monte Carlo realizations, only one extra iteration was required with the representer method to fulfill the convergence criterion. Figure 10b shows that the match between the average posterior horizontal intra-lithology *K* variogram and the model and average prior variogram is nearly perfect. The fact that the intra-lithology conductivity distributions could be calibrated to the measurements without disturbing the prior geostatistics further illustrates that the calibrated lithology fields agreed with the measurements sufficiently well.

Figure 11 and 12 show a performance test for the proposed calibration procedure, respectively for the bimodal and the trimodal field. From left to right, the number of *K*

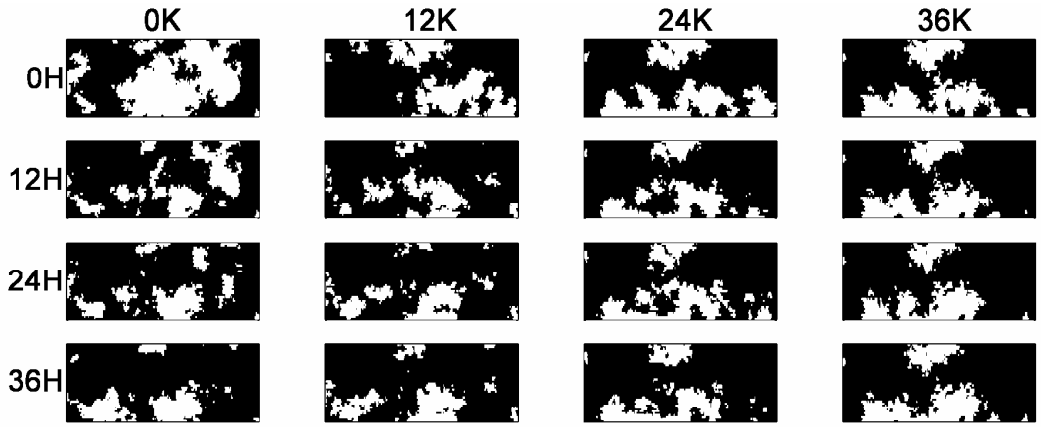

Figure 11. Performance test for the bimodal case. From left to right, the number of *K* measurements increases, and from top to bottom the number of head measurements increases.

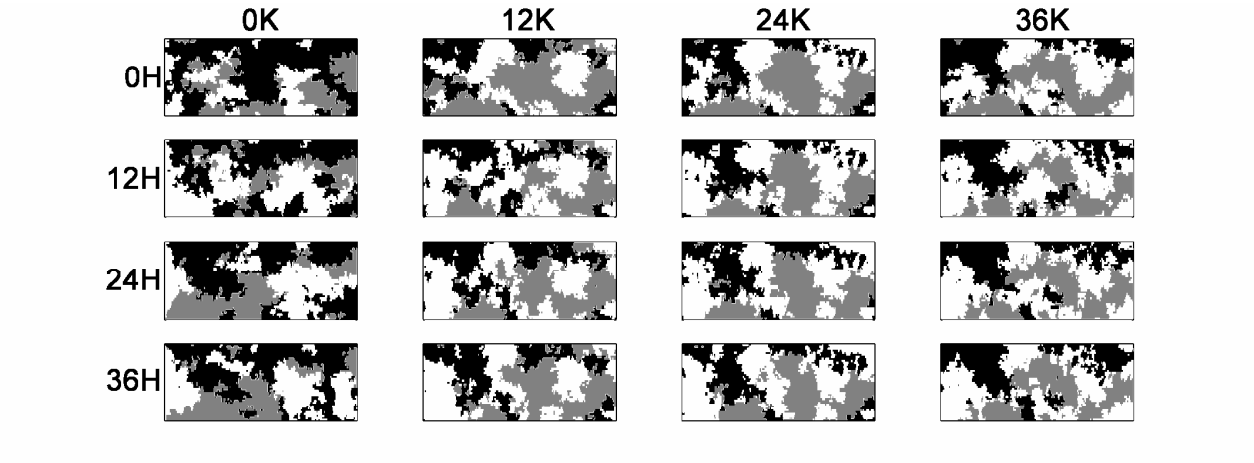

Figure 12. Performance test for the trimodal case.

measurements is increased, and from top to bottom the number of head measurements is increased, both from 0 to 36. Thus, the image in the upper left corner of both figures shows the unconditional realization, while the image in the lower right corner shows the maximally conditioned realization that is possible with the chosen measurement sets.

Figure 11 and Figure 12 further substantiate that data are correctly integrated by the proposed multimodal calibration method, as they show that the more data are used, the better the reference fields are reproduced. Moreover, both figures illustrate that when both types of measurements are used together, they have a complementary effect. A quantification of the improvement of the reference field reproduction is given in Figure 13.

Comparing Figure 13a with 13b reveals that, especially for head measurements, reproducing the reference lithology distribution requires much more sampling effort when the number of lithologies is larger. This can easily be explained from the increased number of possible lithology configurations that produce the same head responses at the measurement locations and still are conditional to the hard data. In the trimodal field (Figure 12), it takes the most extended conditioning set to capture most of the reference field characteristics. The poor resemblance, still, of the right hand quarter of the maximally conditioned field with the reference field is due to the small prior head variance in this area (dictated by the boundary conditions), indicating a small information content of the head measurements in that area.

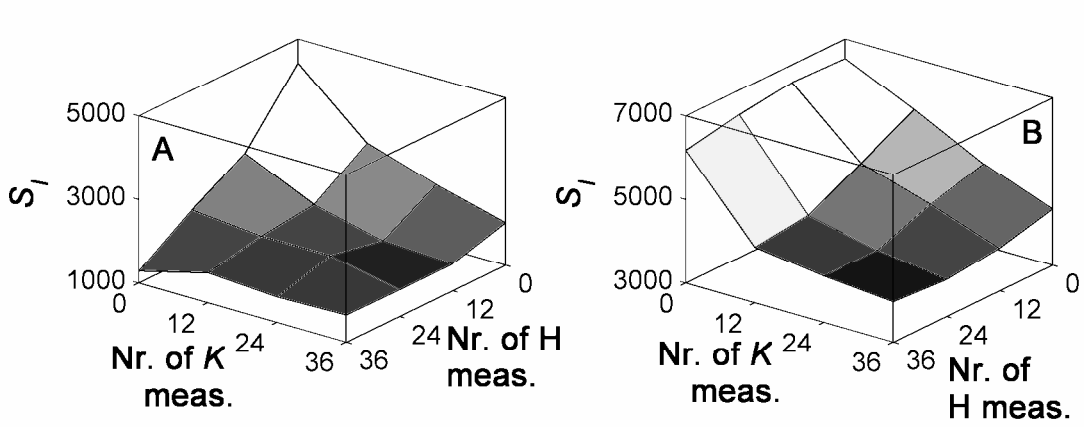

Figure 13. Quantification of the match between the reference field and the fields shown in Figures 11 (Fig. 13a) and 12 (Fig. 13b). S_l = the number of cells with a lithology that is different from the lithology in the corresponding cell of the reference field.

In Figure 13a it can be seen that a better reproduction of the true lithology distribution is achieved when using the 36H measurement set than when additional to this measurement set observations of *K* are incorporated in the calibration. The reason is that *K* measurements, depending on their location, can introduce a bias into the site characterization that is only corrected by H measurements for the part that is important for reproducing the head at the measurement locations. The opposite, a worse lithology reproduction when including more H measurements, can also happen (for instance when going from the 12H24*K* to the 24H24*K* measurement set in Figure 13a). Depending on the location of the additional head measurements, the solution towards reproducing all measurements is not always found in lithology changes towards the reference lithology field. In other words, also head measurements can introduce a bias. Both phenomena make that a monotonically decreasing value of S_l (the number of cells in the posterior field not having the correct lithology) in Figure 13 is not guaranteed.

4.5. Discussion and Conclusions

We proposed a method that can generate realizations of a continuous, multimodal hydraulic conductivity distribution, conditioned on both state measurements and static data.

In the current presentation, the proposed method is used in conjunction with the representer-based inverse method. In this case, the geostatistical parameterization of the method is simple: it only requires prior estimates of the lithology ratios and variograms, prior estimates of the intra-lithology K statistics, and a variogram analysis on (a large number of) transformed fields. The method, when compared to the unimodal application of the representer algorithm, only involves (i) the replacement of the usual logarithmic transformation applied on the hydraulic conductivity data; (ii) recalculation of the parameter covariance matrix for the transformed parameter, and (iii) a backtransformation procedure. For calibration of heterogeneous, multimodal prior fields, we proposed an iterative posterior conditioning procedure that ensures the preservation of the original geostatistics.

In the example calculations, contrasts between the hydraulic conductivities of the various lithologies were large. In this situation, the intra-lithology hydraulic conductivity distributions will only have a very minor influence on the flow and therefore their calibration (step 9 in the calibration flow chart) serves no practical purpose. We chose to use high contrast examples to demonstrate the applicability of our method in combination with the representer-based inverse algorithm, even when the problem is highly nonlinear and the derivative of K to α is locally very large, potentially causing numerical instability from Eq. (7). In our examples, this did not keep the calibration algorithm from finding realistic solutions to the inverse problem. For less contrasting lithologies and for wider intra-lithology K distributions, problems from Eq. (7) are likely to be alleviated, so the method is readily applicable to these cases.

It is emphasized here, however, that the proposed method can be applied in conjunction with any other suitable inverse algorithm besides the representer-based algorithm. Therefore, even if the representer method should run into problems due to instability from Eq. (7), other inverse algorithms could be used that might suffer less from the large derivatives causing this instability.

It should be noted here that our methodology needs modification when applied to significantly overlapping intra-lithology K distributions, as that case asks for a more involved translation procedure from K to lithology.

The required CPU time is the most important disadvantage of the proposed method. In the iterative posterior conditioning procedure, the parameter field has to be calibrated

repeatedly. Using an Intel Pentium 4 2.4 GHz processor with 256 Mb internal memory, it took between 2 and 10 hours to calibrate one realization on 24 head measurements. Of course, the computation time depends mostly on the efficiency of the inverse algorithm applied for the calibration of the transformed, standard normal parameter field (the inner calibration).

Appendix: inference of the parameterization by representers

For easy reference, we provide a condensed derivation of the set of Euler-Lagrange equations and its solution. For a full derivation we refer to *Valstar* [2001] and *Valstar et al.* [2004].

In the minimum of the objective function the variation of the objective function is zero for any variation of the random variables. Forcing this condition on Eq. (3) yields the Euler-Lagrange equations:

$$A_{gf}(\alpha)\lambda_f = \frac{\partial M_p(h)}{\partial h_g}\left[P_v^{-1}\right]_{pn}(z_n - M_n(h)) \tag{A1}$$

$$\alpha_l = \overline{\alpha_l} - P_{\alpha_{lk}}[h_g \frac{\partial A_{gf}(\alpha)}{\partial \alpha_k}\lambda_f] \tag{A2}$$

$$A_{fg}(\alpha)h_g = q_f \tag{A3}$$

where *f* and *g* range from 1 to the number of head state variables; *k* and *l* range from 1 to the number of uncertain parameters; and *n* and *p* range from 1 to the number of measurements. Indices repeated within a single product term are assumed to be summed over appropriate ranges.

The solution of the set of equations given by Eq. (A1), (A2) and (A3) minimizes the objective function. For this solution, an efficient parameterization with representers is applied. The definitions of the representer functions are:

$$\lambda_f = \sum_{p=1}^{N_z} \Gamma_{fp} b_p \tag{A4}$$

$$\alpha_l = \overline{\alpha_l} + \sum_{p=1}^{N_z} \Psi_{lp} b_p \tag{A5}$$

$$h_g = h_{F_g} + h_{corr\,g} + \sum_{p=1}^{N_z} \Xi_{gp} b_p \tag{A6}$$

where b = the vector of representer coefficients, Γ_{fp} = the head adjoint representer for measurement p, calculated for head state variable f, Ψ_{lp} = the parameter representer for measurement p, calculated for uncertain parameter l, h_{F_g} = the prior estimates of the heads, Ξ_{gp} = the head representer for measurement p, calculated for head state variable g, $h_{corr\,g}$ = a head correction term, needed to fulfill the flow equation (as the head expansion is performed around the last estimates, whereas the parameters are expanded around their prior means), N_z = the number of measurements, and $\overline{\alpha_l}$ = the prior estimates of the parameters. Defining b as:

$$b_p = \left[P_v^{-1}\right]_{np} (z_n - M_n(h_F + h_{corr} + \Xi_p)), \tag{A7}$$

and subsequently inserting the representer definitions in the Euler-Lagrange equations and dividing by Eq. (A7) yields explicit expressions for all representers and the correction term. These expressions still depend on the optimal estimates for the parameters and state variables, which are unknown initially and have to be found iteratively. During iteration η, the head adjoint representer Γ_{fp}^{η} is given by:

$$A_{gf}(\hat{\alpha}^{\eta-1})\Gamma_{fp}^{\eta} = \frac{\partial M_p(\hat{h}^{\eta-1})}{\partial h_g} \tag{A8}$$

The expression for the parameter representer Ψ_{lp}^{η} is:

$$\Psi_{lp}^{\eta} = -P_{\alpha_{lk}}\left[\hat{h}_g{}^{\eta-1}\frac{\partial A_{gf}(\hat{\alpha}^{\eta-1})}{\partial \alpha_k}\Gamma_{fp}^{\eta}\right] \tag{A9}$$

The expression for the head representer Ξ_{gp}^{η} is:

$$A_{fg}(\hat{\alpha}^{\eta-1})\Xi_{gp}^{\eta} = -\frac{\partial A_{fg}(\hat{\alpha}^{\eta-1})}{\partial \alpha_k}\Psi_{kp}^{\eta}\hat{h}_g{}^{\eta-1} \tag{A10}$$

The expression for the head correction term $h_{corr\,g}$ is:

$$A_{fg}(\hat{\alpha}^{\eta-1})h_{corr\,g} = q_f + \frac{\partial A_{fg}(\hat{\alpha}^{\eta-1})}{\partial \alpha_k}(\hat{\alpha}_k{}^{\eta-1} - \overline{\alpha_k})\hat{h}_g{}^{\eta-1} - A_{fg}(\hat{\alpha}^{\eta-1})h_{F_g} \tag{A11}$$

And finally, the representer coefficients b_p^{η} can be calculated by a rearrangement of Eq. (A7):

$$([P_v]_{np} + M_n(\Xi_p^{\eta}))b_p^{\eta} = (z_n - M_n(h_F + h_{corr}^{\eta})) \tag{A12}$$

where $M_n(\Xi_p^{\eta})$ is the representer matrix, which consists of all representers at the locations of the measurements.

The algorithm was assumed to have reached convergence when all differences between the measurement predictions from the representer expansion ($h_F + h_{corr} + \Xi b$) and the measurement predictions from the forward model with the updated parameters were smaller than a threshold value. For this research, this threshold value was set at 0.015 m.

References

Bierkens, M. F. P. (1994), Complex confining layers: a stochastic analysis of hydraulic properties at various scales, PhD Thesis, University of Utrecht, Utrecht.

Caers, J. (2007), Comparing the gradual deformation with the probability perturbation method for solving inverse problems, *Mathematical Geology*, 39, 27-51.

Caers, J. and Hoffman, B. T. (2006), The probability perturbation method: a new look at Bayesian inverse modeling, *Mathematical Geology*, 38, 81-100.

Deutsch, C. V., and A. G. Journel (1998), *Geostatistical Software Library and User's Guide*, Applied Geostatistics Series, Oxford University Press, New York.

Dowd, P. A., E. Pardo-Iguzquiza, and C. Xu (2003), Plurigau: a computer program for simulating spatial facies using the truncated plurigaussian method, *Computers & Geosciences*, 29, 123-141.

Freeze, R. A. (1975), A stochastic-conceptual analysis of one-dimensional groundwater flow in non-uniform homogeneous media, *Water Resour. Res.*, 11, 725-741.

Galli, A., H. Beucher, G. Le Lec'h, and B. Doligez (1994), The pros and cons of the truncated Gaussian method, *Geostatistical Simulations*, edited by P. A. Dowd, Kluwer Academic Publishers, Dordrecht, The Netherlands.

Gomez-Hernandez, J. J., A. Sahuquillo, and J. E. Capilla (1998), Stochastic simulation of transmissivity fields conditional to both transmissivity and piezometric data 1. Theory, *Journal of Hydrology*, 203, 162-174.

Hendricks Franssen, H. J. W. M., and J. J. Gomez-Hernandez (2002), 3D inverse modelling of groundwater flow at a fractured site using a stochastic continuum model with multiple statistical populations, *Stochastic Environmental Research and Risk Assessment*, 16, 155-174.

Hoeksema, R. J., and P. K. Kitanidis (1985), Analysis of spatial structure of properties of selected aquifers, *Water Resour. Res.*, 21, 563-572.

Hu, L. Y. (2000), Gradual deformation and iterative calibration of Gaussian-related stochastic models, *Mathematical Geology*, 32, 87-108.

Hu, L. Y., M. Le Ravalec, and G. Blanc (2001a), Gradual deformation and iterative calibration of truncated Gaussian simulations, *Petroleum Geoscience*, 7, S25-S30.

Hu, L. Y., Blanc, G., and Noetinger, B. (2001b), Gradual deformation and iterative calibration of sequential stochastic simulations, *Mathematical Geology*, 33, 475-489.

Liu, N., and D. S. Oliver (2004), Automatic history matching of geologic facies, *SPE Journal*, 429-436.

Lu, Z., and D. Zhang (2002), On stochastic modeling of flow in multimodal heterogeneous formations, *Water Resour. Res.*, 38, 1190, doi:10.1029/2001WR001026.

McDonald, M. G., and A. W. Harbaugh (1984), A modular three-dimensional finite-difference ground-water flow model, USGS, Reston.

Pollock, D. W. (1994), User's Guide for MODPATH/MODPATH-PLOT, Version 3: A particle-tracking post-processing package for MODFLOW, the U.S. Geological Survey finite-difference ground-water flow model, Open-File Report, 94-464, U.S. Geological Survey, Reston.

Press, W. H., B. P. Flannery, S. A. Teukolsky, and W. T. Vettering (1986), *Numerical Recipes: the art of scientific computing*, University of Cambridge, Cambridge.

Rubin, Y. (1995), Flow and transport in bimodal heterogeneous formations, *Water Resour. Res.*, 13, 2461-2468.

Rubin, Y. (2003), *Applied Stochastic Hydrogeology*, Oxford University Press, New York.

Sun, N.-Z., M.-C. Jeng, and W. W.-G. Yeh (1995), A proposed geological parameterization method for parameter identification in three-dimensional groundwater modeling, *Water Resour. Res.*, 31, 89-102.

Valstar, J. R. (2001), Inverse modeling of groundwater flow and transport, Ph.D. Thesis, Delft University of Technology, Delft.

Valstar, J. R., D. B. McLaughlin, C. B. M. Stroet, and F. C. van Geer (2004), A representer-based inverse method for groundwater flow and transport applications, *Water Resour. Res.*, 40, W05116, doi:10.1029/2003WR002922.

Wen, X.-H., T. T. Tran, R. A. Behrens, and J. J. Gomez-Hernandez (2002), Production data integration in sand/shale reservoirs using sequential self-calibration and GeoMorphing: A Comparison, *SPE Reservoir Evaluation and Engineering*, 5, 255-265.

Wingle, W. L. and E. P. Poeter (1998), Directional Semivariograms: Kriging Anisotropy Without Anisotropy Factors, Advances in Geostatistics, 1998 AAPG Annual Meeting, Salt Lake City, Utah.

CHAPTER

5

Simultaneous calibration of a clay layer's presence and conductance: a real world case study

Based on a paper submitted to *Ground Water*

Presented at the *IAHR International Groundwater Symposium*, Istanbul, Turkey, **2008**

[Janssen, G.M.C.M. and J.R. Valstar (2008), Simultaneous calibration of a clay layer's presence and conductance: a real world case study. In: Proc. of the IAHR International Groundwater Symposium, Istanbul, June 18-20, 2008.]

5.1. Introduction

In groundwater model calibration studies, if one of the (spatially distributed) parameters that have to be calibrated contains more than one statistical population, the incidences of these different populations are often predefined, and calibration focuses on the intra-population parameter distribution. In other words, the uncertain spatial distribution of the statistical populations is not allowed to explain deviations between measurements and model predictions during calibration. The model variation necessary to fit the measurements can then be shifted to the intra-population parameters or other parameters that are being calibrated, which can result in exaggerated and unjustified parameter adjustments, potentially rendering unrealistic parameter realizations.

Recently, we presented a method for the Bayesian calibration of multimodal parameter distributions [*Janssen et al.*, 2006 (Chapter 4)]. This method allows for the simultaneous calibration of both the spatial distribution of different statistical populations of a parameter (e.g. classes, lithologies, lithofacies) and the distribution of parameter values *within* the statistical populations (e.g. conductivities, porosities).

The purpose of the work in the present chapter is twofold. First, we demonstrate the applicability of the multimodal calibration method of *Janssen et al.* [2006] to real-world situations. Second, we investigate the added value of the method compared to a conventional approach (i.e. with fixed positions of the statistical populations) for real-world calibration studies. The presumption is, that the added value is established if both approaches lead to significantly different results, and that in such a case the result of the proposed multimodal method deserves more confidence as the uncertainties involved in the model parameterization are treated in a more complete and therefore more fair fashion. To ensure conclusive results with respect to both research questions, a real-world case was chosen for which the positions of the statistical populations significantly affect the sampled variables (i.e., head values in this study).

This study introduces four differences with respect to Chapter 4. First of all, Chapter 4 concerned a hypothetical situation and a synthetic data set (for the sake of method demonstration), whereas the current study displays a real world case. A second difference, which follows directly from the first, is that in the current study the bimodal parameter field is calibrated together with other uncertain parameter fields. To our knowledge, this study is the first to demonstrate this ability, and this statement also

holds in general for the Bayesian co-calibration of multiple spatially correlated parameter fields of which one is non-Gaussian. A third difference is constituted by some improvements made to the original method to expedite convergence. Finally, a relatively minor difference between the previous and the current study is that in the first the method is applied to horizontal transmissivities, whereas here it is applied to the vertical conductance between two (model) layers.

5.2. Method

5.2.1. Theory

The method largely follows *Janssen et al.* [2006] (Chapter 4). For the reader's convenience, it is briefly restated here. The steps to be taken are schematically visualized in Figure 1, to which is referred in the following explanation of the method.

First, using prior information (expert knowledge, hard data etc.), the geostatistical properties of the different statistical populations (e.g. lithologies) and their spatial distribution are estimated, based on which a realization is generated for the occurrence of the statistical populations (Fig. 1-1), and for the intra-population parameter fields (transmissivities, conductances, porosities, etc., see Fig. 1-2 and 1-3). These realizations are combined to one multimodal parameter field as shown in Fig. 1-4. This is the prior estimation of reality that will now be calibrated. In order to take away the fatal properties of this multimodal parameter field for the applicability of existing inverse methods (see Chapter 4), the parameter field in Fig. 1-4 is transformed to the standard normal distribution (Fig. 1-5). In case the field in Figure 1-4 has a bimodal lognormal distribution, the transformation equations of *Janssen et al.* [2006] (Chapter 4) can be used for this purpose.

The inverse algorithm subsequently applied for the calibration of the transformed parameter field (we call this the inner iteration loop), requires the geostatistical properties of the standard normally distributed parameter. This transformed distribution per definition has unit variance, the ranges can be obtained by a Monte Carlo analysis on a large number of transformed fields, and a suitable geostatistical model can be parameterized by a nonlinear regression analysis on the variogram.

After back-transformation, the result of this calibration step is a bimodal parameter field that obeys the measurement information (Fig. 1-6), to the extent determined by the strength of the chosen inverse algorithm and the convergence criterion. However, due to the fact that, by effectively combining the geostatistical properties of both statistical populations and their spatial distribution into one variogram, inevitably geostatistical information gets lost, and the geostatistics of this parameter field are distorted with respect to the original geostatistics used to construct the fields in Fig. 1-1, 1-2 and 1-3. The working hypothesis is, however, that nonetheless this calibrated field contains much information on necessary switches in statistical populations to reduce the objective function. This information is made use of by selecting those cells that have not switched to the other statistical population (see for example the colored areas in Fig 1-7) and by using these cells to condition a new spatial distribution of the statistical populations. In the remaining cells (e.g. the white areas in Fig 1-7) the simulator used for the generation of this spatial distribution has freedom to introduce modifications with respect to the prior spatial distribution. Although not guaranteed, these modifications are likely to result in objective function reduction (compared to the prior field), since during the inner calibration they were introduced too. The spatial distribution of the statistical populations, newly generated in this way, is combined again with new realizations of the intra-population parameter distribution and it is evaluated whether the new bimodal parameter field results in a sufficient match between model results and state observations (see Section 5.2.3. for the criterion used). If negative, the steps sketched above are repeated until it does (we call this the outer iteration loop, and this process of conditioning new "prior" multimodal fields on the cells that have not changed lithology during the inner calibration is referred to as iterative posterior conditioning in Chapter 4). If affirmative, the spatial distribution of the statistical populations is accepted, and a final run, here called a "postrun", is performed (Fig. 1-8). This postrun consists of a "conventional" calibration, by which we mean here that the positions of the statistical populations are fixed at their calibrated positions and only the intra-population parameter fields (set back at their prior means) are calibrated. This postrun is necessary, because the parameter values assigned to these populations in Fig. 1-4 are still uncalibrated at the point where the convergence criterion for the outer calibration loop is evaluated. Note, however, that their uncertainty is taken into account while calibrating the indicator field via the outer ite-

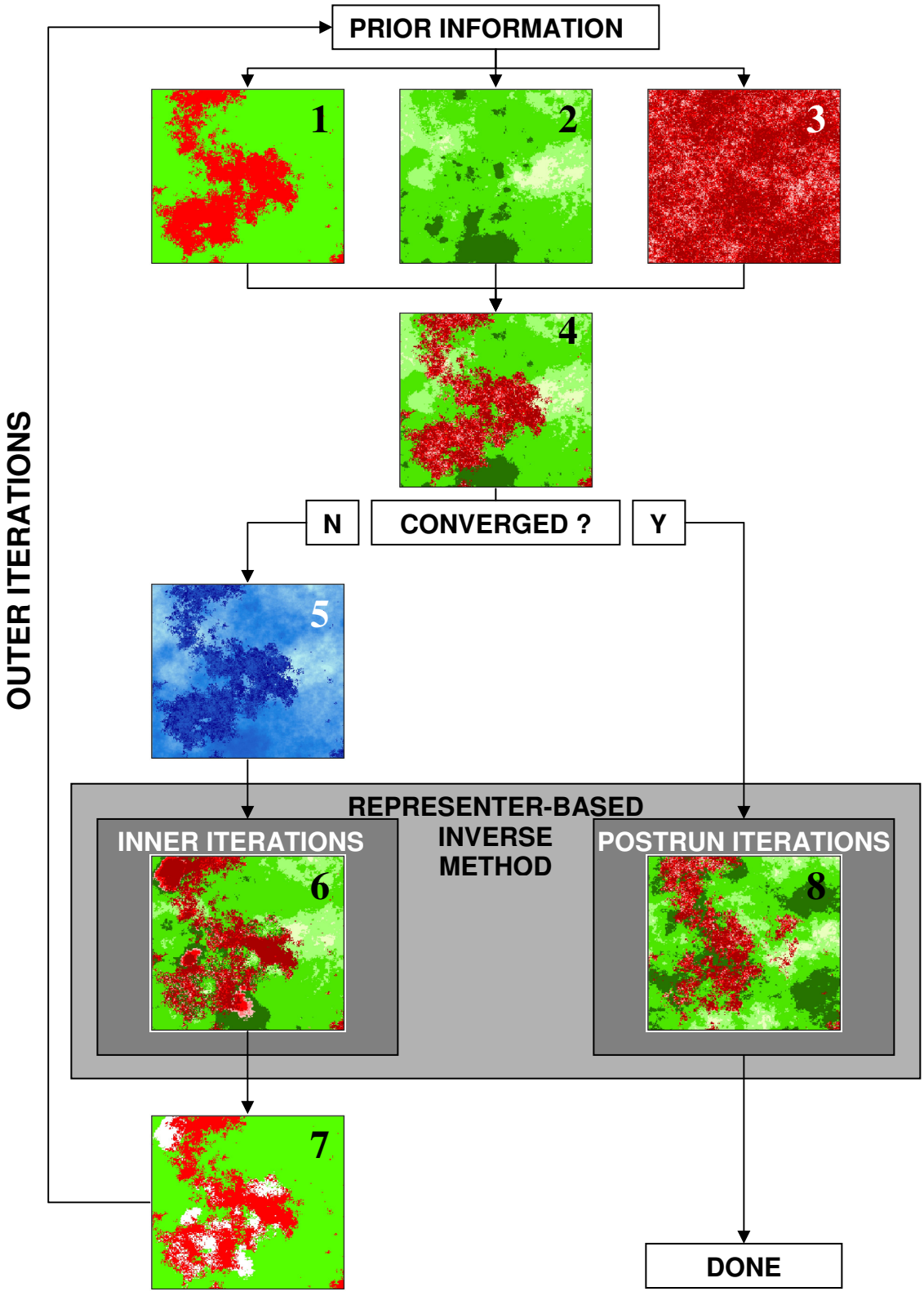

Figure 1. Schematic overview of the multimodal calibration method. For explanation see text.

-rations, as they are co-estimated when calibrating the transformed field (inner iterations).

5.2.2. Toolbox

For the simulation of the spatial distributions of the statistical populations we used the sequential indicator simulator SISIM [*Deutsch and Journel*, 1992]. The sequential Gaussian simulator SGSIM [*Deutsch and Journel*, 1992] was used to generate the continuous parameter fields for every statistical population.

For the inner iteration loop and the postrun, the Bayesian, representer-based inverse method [*Valstar*, 2001; *Valstar et al.* 2004] was used. Major advantage of this inverse method is the fact that the method is "optimal" with respect to the amount of information extracted from the observations in the Bayesian context. Other inverse methods can, however, be used also.

5.2.3. Adjustments and extension of the original method

For the current study, a number of adjustments were made with respect to the original presentation of the methodology in *Janssen et al.* [2006]. The most important adjustment is that in the current case study the calibration will not be limited to the multimodally distributed parameter, but simultaneously also other stochastic fields are calibrated. These fields are all assumed to be lognormally distributed and geostatistics have been derived for their Gaussian distributed, lognormal transform. This means that the calibrated values of these parameters, resulting from an inner iteration loop, can be adopted in the new model created at the start of the subsequent outer iteration or in the postrun, as their spatial correlation is not disrupted by an additional transformation procedure. Their mean (expected) values, however, are kept constant at the prior estimates during the entire calibration (outer iterations and postrun), to prevent the parameters to continuously drift away from the expected values, as that can result in unrealistic parameter values.

Second, at the start of an outer iteration, not one but ten new bimodal parameter realizations (Fig. 1-4) are generated, and the best realization (the one with the lowest

objective function value) is chosen to enter the next inner calibration loop. In preliminary calculations, this was found to dramatically expedite convergence and might even alleviate the convergence problems mentioned in *Janssen et al.* [2006], although this latter suggestion was not verified.

Finally, whereas the convergence of the outer calibration loop was tied to a certain value of the objective function in *Janssen et al.* [2006], here we simply consider the outer calibration to be converged if the objective function value has not significantly been reduced during a number of successive outer iterations (evaluated by visual inspection of the objective function value development). The reason for this other approach is that the convergence criterion applied to the synthetic case in *Janssen et al.* [2006] requires a fully known "true" spatial distribution of the statistical populations, a requirement that of course can not be fulfilled when dealing with a real-world case study.

5.3. Model area

The area chosen for the real-world case study is located in the east of the Netherlands (see Figure 1a). This area was chosen because of the availability of a large dataset and a state-of-the-art groundwater model (see next Section), and the presence of a highly discontinuous and heterogeneous clay layer at a depth of about 10 meters below the soil surface. Besides the heterogeneous clay layer, the model area is characterized by:

- the presence of large groundwater abstraction clusters for drinking water production (see Fig. 2b).
- the presence of two moraines (one in the western part of the domain and one in the center part, see Fig. 2c), formed during the last glacial period. At the locations of these moraines the surface elevation is higher and the unsaturated zone thicker;
- the Regge river, draining the area between the moraines (see Fig. 2b);
- intensive drainage in the north-eastern part of the area by a dense surface water system (see Fig. 2b).

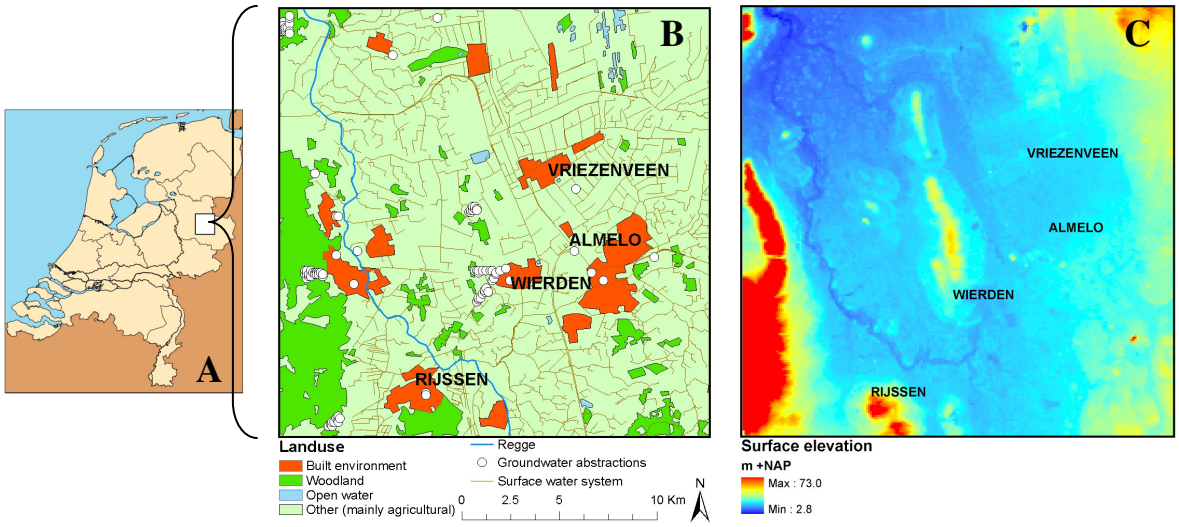

Figure 2. The model area. A) Geographical position in The Netherlands. B) Landuse, surface waters and groundwater abstractions. C) Surface elevation (NAP = the dutch elevation datum (= "sea level").

For illustration, Figure 3 shows a 2D schematic east-west cross-section of the model area (through approximately the center of the domain) highlighting the position of the clay layer in the subsurface. The clay layer acts as a discontinuous confining layer between the upper aquifers and the "production aquifer" that contains all water abstractions. In previous model studies (mentioned in the next Section), head values were found to be quite sensitive to the conductance of this clay layer, which makes it ideal for the current study. Its schematization in a groundwater model greatly influences the calculated capture zones of the abstraction clusters, as shown by *Van Leeuwen et al.* [1999].

5.4. Model description

Mainly because of the presence of the drinking water abstractions and the resulting complex issues with catchment area delineation and protection and effects on groundwater levels, this area has been the subject of several previous groundwater modeling studies [*Hoogendoorn and Te Stroet*, 1994; *Te Stroet*, 1995; *Van Leeuwen et al.*, 1999]. Furthermore, the current model area was covered by a MODFLOW model

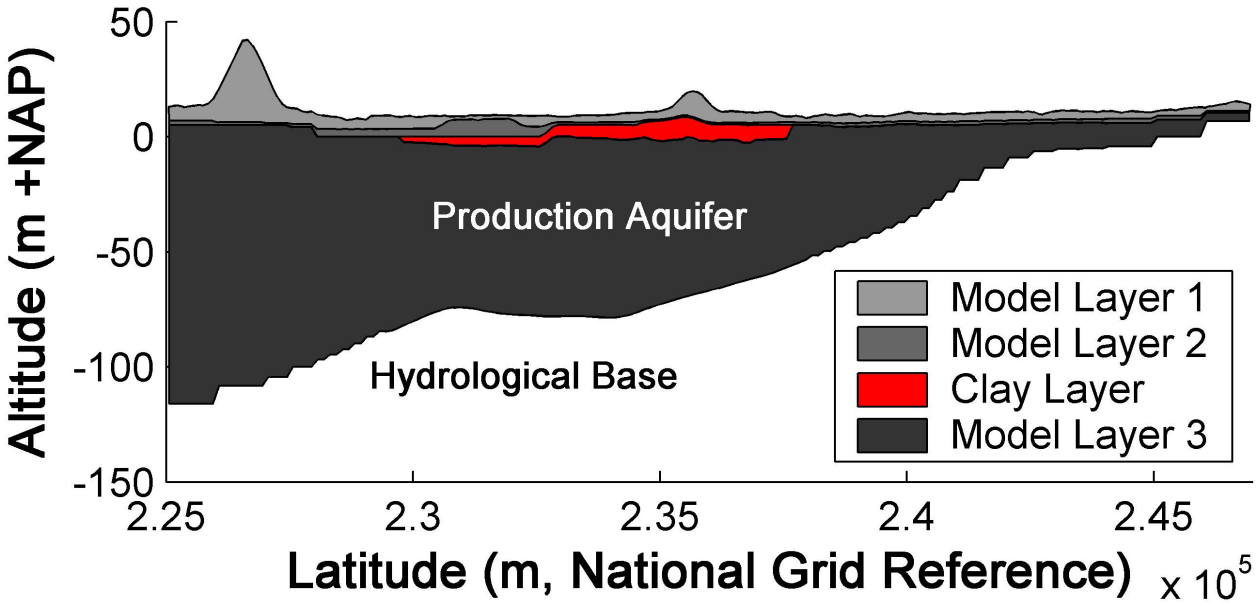

Figure 3. Conceptual east-west cross-section trough approximately the center of the model area. The layers in this cross-section correspond with the groundwater model layers.

developed for a larger area by *Snepvangers et al.* [2004] and later by *Snepvangers et al.* [2007]. Due to the regional character of the latter two models, the clay layer was not calibrated explicitly in these studies. *Van Leeuwen et al*. [1999] treated the clay layer as a stochastic random field, but only conditioned it on borehole information. In *Hoogendoorn and Te Stroet* [1994] and *Te Stroet* [1995], the clay layer was calibrated using a zonation approach, not allowing the position of the clay layer to be altered during the calibration.

For the current study, the area of interest was cut from the regional model built by *Snepvangers et al.* [2004] using MODTMR [*Leake and Claar*, 1999]. The resulting model has a discretization level of 100x100 meters in the horizontal plane, and consists 220 columns, 220 rows, and 3 layers that represent the 2 upper aquifers and the production aquifer as shown in Fig. 3. At the model's vertical borders, fixed head boundary conditions were imposed everywhere, the head values for which were adopted from a steady state run with the larger parent model. Boundary conditions in the top model layer include rivers, drains, recharge and evapotranspiration. A no-flow boundary

condition was imposed at the bottom of layer 3 (the hydrological base, see Fig. 3). The current study only uses the model in steady state.

The clay layer was accounted for in the vertical conductance between model layer 2 and 3 (abbreviated as Vcont in the remainder of this chapter). At locations where the clay layer is present, Vcont was taken as the quotient of the estimated or measured clay thickness D, and the estimated vertical conductivity K_v of the clay (assumed much less variable than the clay layer's thickness and therefore constant, K_v = 0.005 m^2/d). So, Vcont = K_v/D. The geostatistics of Vcont are therefore directly related to the geostatistics of the thickness of the clay layer. For the area outside the clay layer, the geostatistics of Vcont were derived from the parent model. The combination of the geostatistical population of Vcont values within the clay layer with that of the Vcont values outside the clay layer constitutes a bimodal distribution of Vcont.

For the estimation of the geostatistical properties of the clay layer's presence and thickness the same dataset was used as discussed by *Van Leeuwen et al.* [1999]. Figure 4a ("Full Set") shows the locations of the 546 borehole drillings used to obtain this dataset. *Van Leeuwen et al.* [1999] showed that the observations of the clay layer's thickness exhibit a lognormal distribution. Also for the vertical conductance at locations where the clay layer is absent a lognormal distribution was assumed. Thus, Vcont can

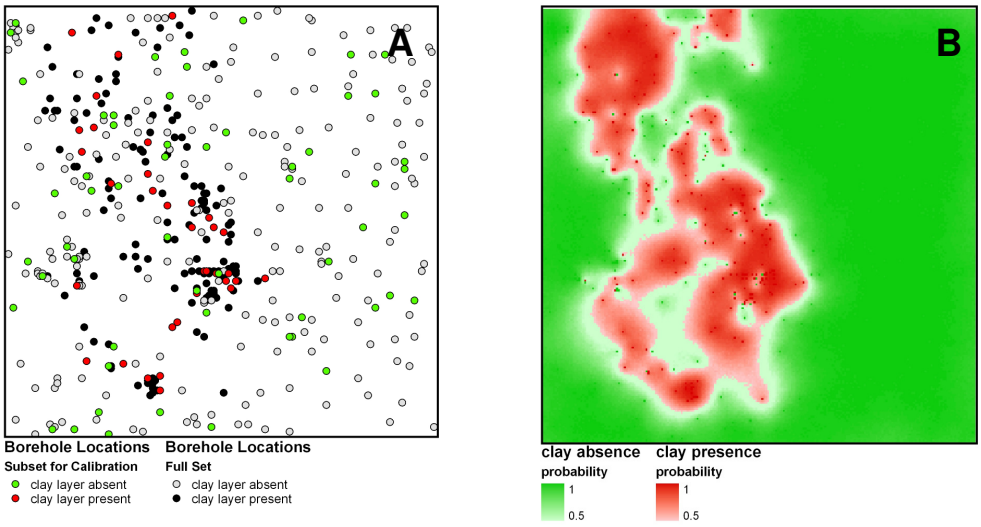

Figure 4. A) Borehole locations in the model area. B) Probability field for clay absence and clay presence, derived from 1000 realizations of the indicator field.

be modeled as a bimodal lognormal distribution. Transformation to the standard normal distribution can therefore be achieved by applying the same transformation equations as used in *Janssen et al.* [2006]. Table 1 presents all derived geostatistics involved in modeling Vcont, as well as those of the standard normal transform of Vcont (acquired by Monte Carlo analysis on a large number of transformed Vcont realizations).

Figure 4b shows the clay occurrence probability field calculated from 1000 Monte Carlo realizations of the spatial statistical population distribution, all conditioned on all abovementioned boreholes and using the derived geostatistics. In this figure, locations where the clay incidence probability is greater than the clay absence probability are designated as belonging to the clay layer (and vice versa). The thus created "average"

Table 1. Geostatistics of the calibrated parameters. γ = semi-variance, s = lag distance, LN = lognormal transform, Vcont = vertical conductance between model layer 2 and 3. For the definitions of the groundwater model parameters, we refer to *McDonald and Harbaugh* [1988]. For the definitions of the geostatistical parameters, we refer to *Webster and Oliver* [2001].

Parameter	Value	Parameter	Value
Indicator Field		**LN(Vcont) clay**	
P1 (marginal probability for "no clay")	0.8	μ (mean)	-7.0 LN(m/d)
		a (isotropic range)	7000 m
P2 (marginal probability for "clay")	0.2	n (nugget)	0.55
a (isotropic range)	5400 m	c (sill)	0.8
n (nugget)	0.05	Variogram model	Exponential
c (sill)	0.24	**Standard Normal Transform of Vcont**	
Variogram model	Exponential	μ (mean)	0.0
LN(Vcont) no clay		a (isotropic actual range)	1171 m
μ (mean)	-3.0 LN(m/d)	n (nugget)	0.0
a (isotropic range)	5000 m	c (sill)	1.0
n (nugget)	0.0	Variogram model	$\gamma(s) = c \cdot [1-\exp(-3s^{0.82}/a)]$
c (sill)	0.28		
Variogram model	Exponential		

Table 1. (*Continued*)

Parameter	Value	Parameter	Value
LN(Transmissivity Layer 1)		**LN(River Conductance) Class "Canals"**	
a (isotropic range)	7000 m	a (isotropic range)	∞ m
n (nugget)	0.0	n (nugget)	0.0
c (sill)	0.10	c (sill)	0.70
Variogram model	Exponential	Variogram model	Exponential
LN(Transmissivity Layer 3)		**LN(River Conductance) Class "Other"**	
a (isotropic range)	7000 m	a (isotropic range)	∞ m
n (nugget)	0.0	n (nugget)	0.0
c (sill)	0.15	c (sill)	0.20
Variogram model	Exponential	Variogram model	Exponential

idea of the clay layer's extent is considered the best available estimation of its true shape, and will be used as such later when evaluating calibration results.

Besides Vcont, also the spatially distributed transmissivities of model layers 1 and 3, and the river conductances are calibrated. Their geostatistical properties, which are input for the inverse model, are all adopted from the parent model and given in Table 1. From sensitivity analyses performed on both the parent model (results given in *Snepvangers et al.*, [2004]) and the current model (results not shown) it was concluded that the transmissivities of layers 1 and 3, and the river conductances, are the only parameters that have a significant influence on head values at the observation locations within the parameters' uncertainty ranges (given in Table 1). Other parameters were therefore not calibrated.

5.5. Outline of the performed calculations

The calibrations in this study were performed using both borehole information (clay presence/absence and clay thickness) and head values. The borehole information was used to condition the spatial lithology distributions (Fig 1-1) and the continuous vertical conductance field for the clay layer (Fig 1-3). Because borehole drilling density in The

Netherlands is not representative for data availability generally encountered in other parts of the world, only a fifth of the “Full Set” in Figure 4a was used for conditioning of the prior fields and conditioning during calibration. This “Subset for Calibration” is also shown in Figure 4a (colored dots). An advantage that comes with this selection is that we were able to use the remaining drillings for validation purposes. Values of Vcont outside the clay layer were, apart from the indicator class (or mode) designation and inference of geostatistics, never conditioned on borehole data in this study.

All calibration runs in this study were performed on the same set of 125 groundwater head measurements (Figure 5). Only those available head measurements were used that are more than 2 km (20 model cells) away from the outer model boundaries, to minimize boundary effects in the residuals.

All calibration runs performed, both the synthetic ones and the real world calibrations, started with the same prior model. The simulated realization of Vcont in this prior model (conditioned on the “Subset” of boreholes) is shown in Figure 6a. Compared with the “average” field (Fig. 4b), the prior clay layer extends much further into the east, has much more (continuous) clay in the south and generally underestimates the presence of clay in the northwest quarter of the domain. The prior fields of the calibrated parameters other than Vcont were identical to the calibrated fields of the parent model. So, in contrast to Vcont, these fields were not simulated prior to calibration. The prior fields of these parameters are shown in the Appendix (Fig A1a, A2a and A3a).

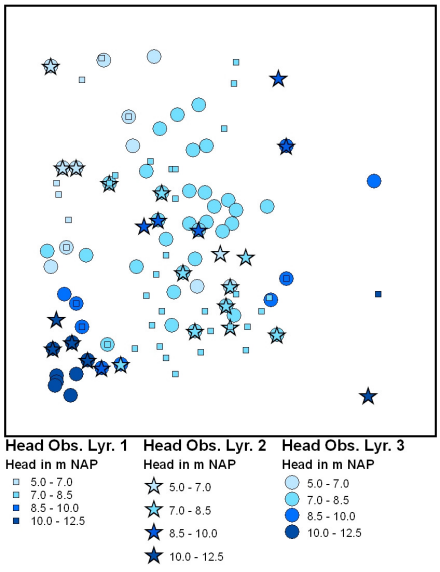

Figure 5. Head observations observations in the model area, per model layer.

The performed calculations consisted of two sets of synthetic calibration runs and one set of full-blown, real-world calibrations. A set consisted of an A and a B calibration run, the first performed with the proposed multimodal method and the latter with the conventional approach (not allowing the clay layer to change shape).

In the synthetic sets, measurement values at the measurement locations shown in Figure 5 were generated using a reference model that is considered to be the "truth". The prior model and the reference model only differed in the bimodal parameter field (Vcont) realization. The reference realization of Vcont, conditioned on the "Full Set" of boreholes, is shown in Figure 6b.

In the first synthetic set (runs 1A and 1B) only Vcont was calibrated. The head observations were assumed virtually error free. The most important purpose of these calibration runs was to check the algorithm and its implementation, and to demonstrate its power. Because the observations were assumed virtually error free, and all residuals could be explained by Vcont, the reference field is expected to be largely found back. This is not necessarily the case if other parameters are calibrated and measurement errors are involved.

In the second synthetic set (runs 2A and 2B), also the other parameters (the

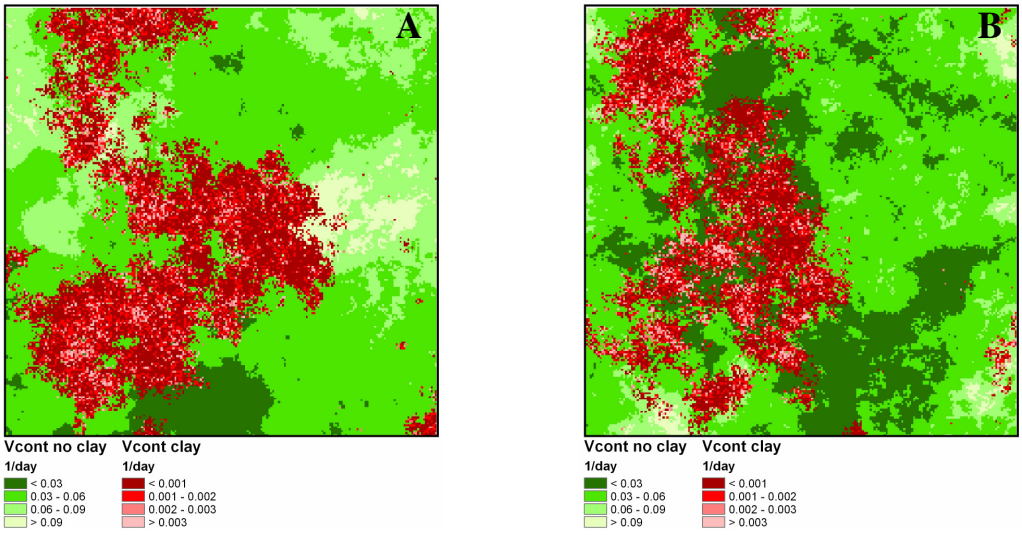

Figure 6. A) Prior realization of Vcont, conditioned on information from the Calibration Set of boreholes (Fig. 2a). B) Reference realization of Vcont, conditioned on information from the Full Set of boreholes (Fig. 2a).

transmissivities of layers 1 and 3, and the river conductances) were calibrated. Furthermore, realistic measurement error variances were assigned to the head observations (based on the true, real world data set). The purpose of runs 2A and 2B was to check whether the case shows enough sensitivity of the head values to Vcont to constitute an interesting real-world case, and to find out whether the measurement errors and other parameters could together obscure adverse effects of neglecting the uncertainty involved in delineating the clay layer, by fully absorbing the need to reshape the clay layer.

The actual real-world calibration exercise is constituted by model runs 3A and 3B. Runs 3A and 3B were identical to runs 2A and 2B, the only difference being that now true head observations were used. Thus, the similarity between the synthetic and real-world runs was maximized, facilitating the use of the synthetic results to help understand the results of the real-world calibration runs 3A and 3B.

5.6. Results

5.6.1. Run 1 (Synthetic)

The results of run 1A and 1B (synthetic calibration of only the vertical conductance between the second and the third model layer) are shown in Figure 7a-d. Figures 7a and b compare the Vcont field obtained with respectively the proposed multimodal method and the conventional method. In the multimodal calibration, clay occurrence diminished substantially in the southern and eastern part of the domain compared to the initial field (Fig. 6a). In fact, the multimodal method resulted in a calibrated spatial position of the clay layer that much resembles that of reference field (Fig. 6b).

In the calibrated field that resulted from the conventional approach, on the other hand (Fig. 7b, note that the color scale definition is identical to Fig. 7a), a strong bias to higher conductance values within the clay layer is evident, as well as a bias towards lower conductance values outside it.

To understand the results, we first need to take a look at the maximum a posteriori estimator employed in the representer approach [*Schweppe*, 1973; *Valstar et al.*, 2004]. This estimator penalizes observation misfits, as well as the adjustments of parameters (with respect to their prior estimates). In the conventional calibration approach, the

positions of the statistical deviations are not allowed to explain (part of) the residuals. This makes that the intra-population parameter adjustments, necessary to get a good observation reproduction, inevitably are bigger than they need to be if the residuals were to be reduced first by optimizing the positions of the statistical populations. In the current example, the parameter adjustments in conventional calibration run 1B are so big that even the overall parameter distribution as a whole becomes biased. Since in the initial field the clay occurrence in most areas is overestimated rather than underestimated, the conventional calibration yields a heavy bias towards high conductance values in the posterior Vcont distribution for clay. This is also shown in Fig. 7c, in which the posterior Vcont distributions for clay are compared with the initial Vcont distribution, indicated by the green line. From the posterior Vcont distribution resulting from the conventional calibration run (red histogram), it is clear that the calibration caused a large shift in the parameter distribution. In Fig. 7c this histogram is cut off, but it extends well into the range of values that belong to the "no clay" mode of the bimodal distribution. Using the multimodal approach, on the other hand, the shape of the Vcont distribution (white histogram) was virtually unaffected, i.e. it remained virtually identical to the Vcont distribution taken as the "truth" in this synthetic calibration example.

Undoubtedly partly due to the same (though inverted) mechanism, also the Vcont values *outside* the clay layer show a bias, as can be observed from the extended dark green areas in Fig. 7b (a simple histogram comparison between the prior and posterior distribution would however not be fair: because of the long correlation ranges of Vcont outside the clay layer, the initial and calibrated realizations of Vcont outside the clay layer are far from ergodic).

In the maximum a posteriori estimator, the need for larger parameter adjustments automatically leads to poorer observation reproduction, as the balance between parameter adjustment and observation misfits, as searched for in the solution of the inverse problem, will shift towards the residuals if parameter adjustments get larger. This effect can be observed in Fig. 7d, which shows the development of the objective function (sum of squared residuals) during both calibration runs. By letting the clay layer change shape, not only the prior distribution of Vcont is preserved, but also a better observation reproduction is achieved than when it is fixed at its prior position: the postrun of the multimodal calibration resulted in a sum of squared residuals (J) of 0.028 m^2, whereas

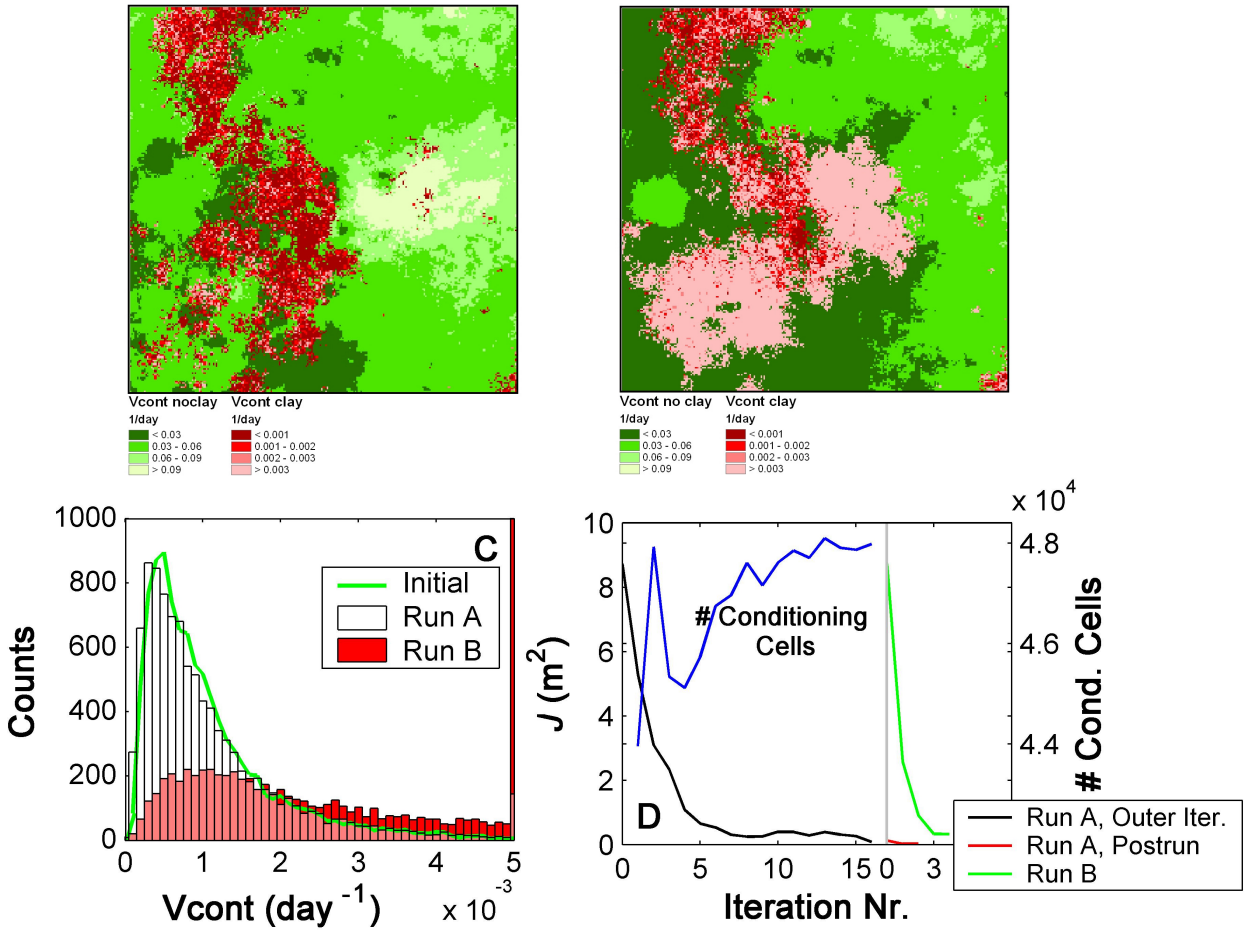

Fig. 7A) Calibration result for Vcont achieved with the multimodal method (run A). B) Calibration result for Vcont achieved with the conventional approach (run B). C) Comparison between, on one hand, the prior histogram of Vcont, and the posterior histograms obtained with Run A and B on the other. D) Development of the sum of squared residuals during the various calibration runs. J = sum of squared residuals.

the B-run (conventional approach) converged at J = 0.32 m^2. Although also the latter J value still implies good observation reproduction, it is more than 11 times the first, and observations were therefore approximated considerably better in the multimodal calibration run. Moreover, as stated above, in the conventional approach the good observation reproduction could only be achieved at the cost of a realistic posterior parameter distribution.

5.6.2. Run 2 (Synthetic)

Whereas in run 1 only the vertical conductance between the second and third model layer was calibrated, and this calibration was performed on synthetic observations which were assumed virtually error-free, in run 2 also other parameter fields were calibrated, and realistic measurement errors were assigned to the (still synthetic) observation values.

Fig. 8a-d shows the results of both calibration run 2A and 2B. These runs behaved in a manner that is comparable to the 1A and 1B runs: again, the multimodal calibration run resulted in an adjustment of the prior clay layer towards a realization that more resembles the reference field than the prior realization, without introducing a bias in the Vcont values (see Fig. 8a). However, the changes made to the shape of the clay layer are less pronounced, which is due to the increased number of parameters involved in the calibration (presenting the calibration algorithm with more freedom to resolve the residuals) and the realistic observation errors that were now assigned to the head measurement values (decreasing the need for residual reduction altogether).

The calibration result of conventional run 2B (Fig. 8b and Fig. 8c, red histogram) again exhibits a bias in the Vcont distribution towards higher values of the reference distribution, as was observed in the result of run 1B (Fig. 7b). Although the bias is less severe than for run 1B, which can be explained by the same reasons as given above for the less pronounced adjustment of the clay layer's position in Fig. 8A compared to Fig. 7A., the bias is still dramatic. Moreover, the price paid for the reduced bias is a much higher value of the objective function after convergence (Fig. 8d) compared to run 1B, suggesting that not so much the other parameters are taking over some of the explanation of the residuals, as is the calibration algorithm gratefully utilizing the relaxation offered by the measurement errors. In run 2A, the algorithm does much less so: by bringing the clay layer's shape in line with the observations, there is much less the need to exploit the noise around the measurements, and the residuals are still reduced to a very low level.

The fact that the clay layer's position was significantly altered in run 2A, and a bias was realized when this position change was not allowed in run 2B, confirms that 1) the groundwater model shows enough sensitivity to Vcont for it to constitute an interesting real-world test case for the multimodal calibration method, and 2) variation of the other

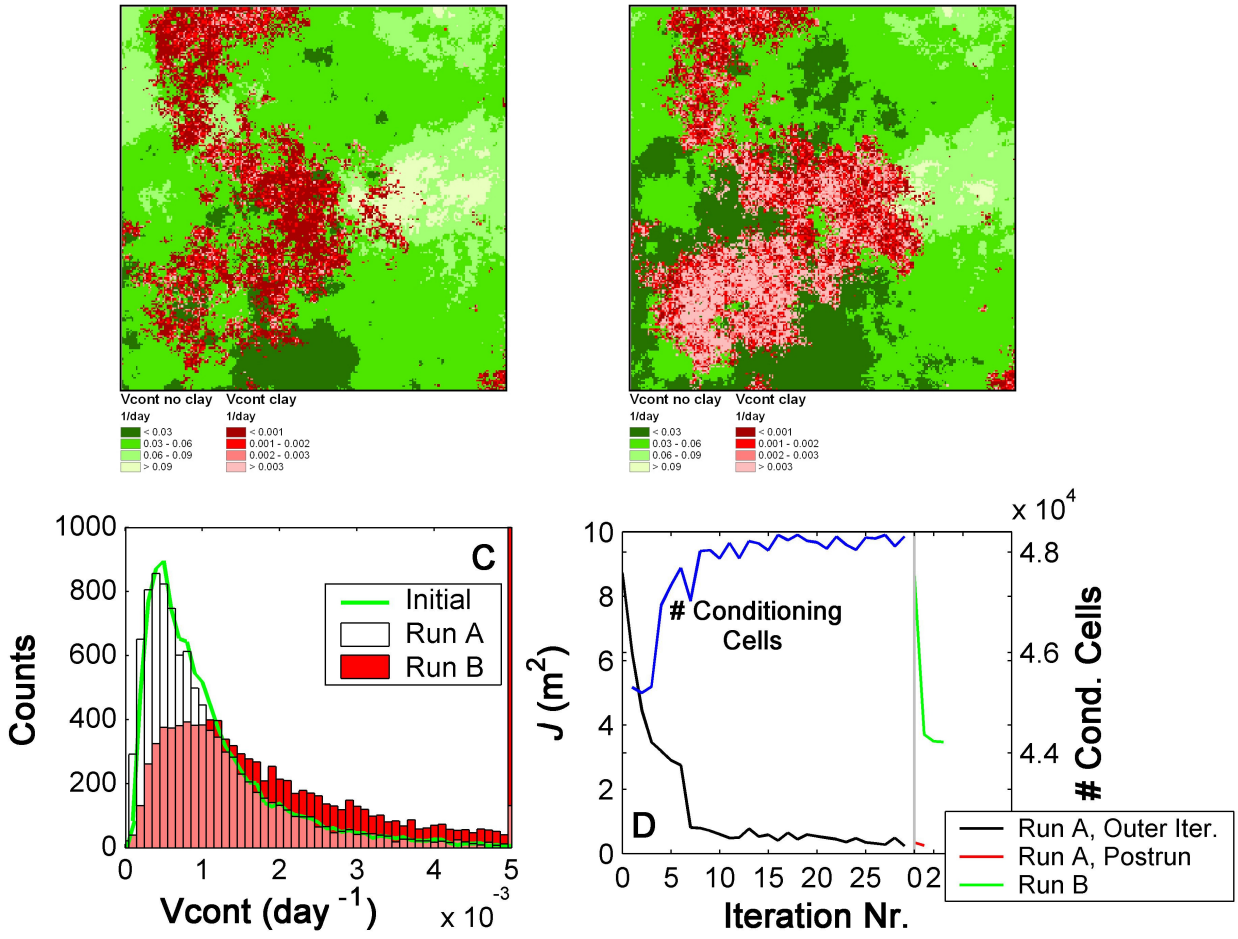

Fig. 8A) Calibration result for Vcont achieved with the multimodal method (run A). B) Calibration result for Vcont achieved with the conventional approach (run B). C) Comparison between, on one hand, the prior histogram of Vcont, and the posterior histograms obtained with Run A and B on the other. D) Development of the sum of squared residuals during the various calibration runs. J = sum of squared residuals.

calibrated parameters cannot decrease the residuals to the extent that adverse effects of the conventional calibration method are masked. This means that if the model is good enough, it should be possible to observe the same adverse effects of the conventional calibration approach in the real-world case.

5.6.3. Run 3 (Real-world)

The calibration results for Vcont of the full-blown real-world runs 3A and 3B are given in Figures 9a and 9b, respectively. In Figure 9a it can be seen that in the A-run significant modifications were made to the spatial distribution of the clay layer. For easy comparison, the change in clay occurrence is visualized in Figure 10. From this figure it becomes clear that adjustments largely were made at those locations where, based on the differences described above between the probability field (Fig. 4b) and the prior field, they were to be expected the most. For example, the calibration clearly reduced the occurrence of clay in the south and east part of the domain, whereas the amount of clay in the northwest quarter of the area was increased substantially.

In the result of the conventional approach (Fig. 9b and 9c, red histogram), again a significant bias can be observed in the Vcont distribution for clay towards higher values. Assuming that all important aspects of the groundwater system other than the clay layer's position were modeled sufficiently well, the same explanations can be attributed to this bias as was done in the synthetic cases. Interestingly enough, also the result of the multimodal calibration shows a bias now, but in the opposite direction. A simple but conceivable explanation for this reduction of the mean conductance of the clay layer could be that the prior mean of the vertical conductivity of the clay was overestimated. This hint did not present itself during the conventional calibration run. In fact, from that run the modeler could conclude that perhaps the vertical conductivity was underestimated (considering the bias towards higher conductance values in the calibration result). The result would be very different conclusions about well capture zones and the protective capacities of the clay layer.

The adjustments made to the co-calibrated parameter fields (the transmissivities of model layer 1, the transmissivities of model layer 3, and the river conductances) are illustrated in the Appendix, in Figures A1b-c, A2b-c, and Tabel A1, respectively. From these figures and table the general pictures arises that adjustments to the prior fields of these parameters were generally much smaller in run 3A than in run 3B, the only exception being the river conductances, see Table A1. These results therefore illustrate the projection of parameter variation, necessary to fit the measurements, from Vcont to the other parameter fields, in case of the conventional calibration approach.

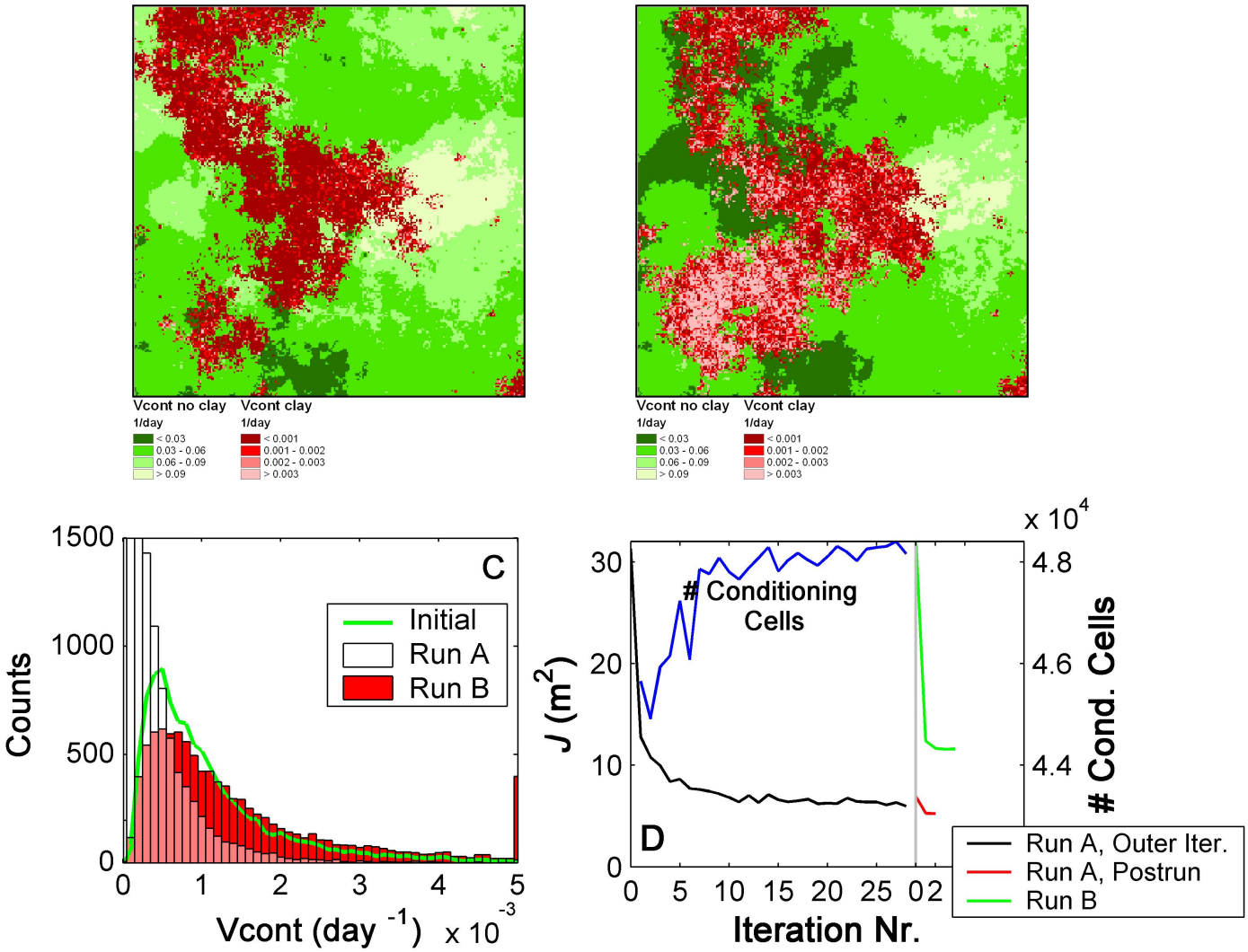

Fig. 9A) Calibration result for Vcont achieved with the multimodal method (run A). B) Calibration result for Vcont achieved with the conventional approach (run B). C) Comparison between, on one hand, the prior histogram of Vcont, and the posterior histograms obtained with Run A and B on the other. D) Development of the sum of squared residuals during the various calibration runs. *J* = sum of squared residuals.

Figure 9d shows the development of the sum of squared residuals during the iterative calibration runs. The conventional run (green line) was converged after three iterations, after which the sum of squared residuals was reduced from 31.3 m^2 to 11.59 m^2. The outer iteration loop of the multimodal calibration run was considered converged after iteration 22, when the sum of squared residuals was reduced from 31.3 m^2 to 5.97 m^2. The subsequent postrun converged in three inner iterations, during which the sum of

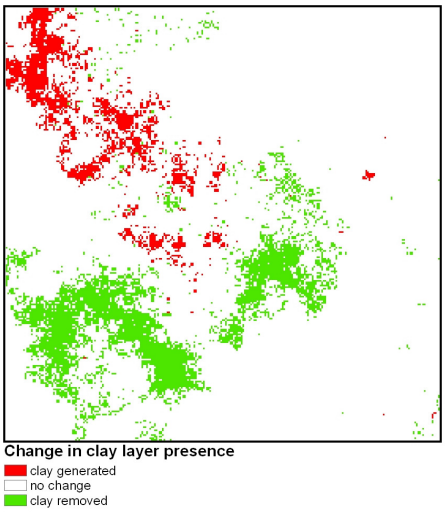

Figure 10. Illustration of the changes made to the spatial distribution of the prior clay layer during calibration run 3A.

squared residuals was reduced from 6.92 m^2 to 5.24 m^2. So, the bimodal calibration resulted in a sum of squared residuals that was more than 50% less than achieved with the conventional approach. This difference is not surprising: improvement in the final objective function value was to be expected as the calibration algorithm is presented with an extra degree of freedom by allowing switches between statistical populations.

The question that remains is whether the result produced with the proposed multimodal calibration approach is indeed more realistic. This is a difficult issue since the reality is not known. However, by not using all available boreholes for the conditioning of the clay layer during calibration, a couple of tests can be performed to at least get some quantitative scores on plausibility of the calibration results obtained with both approaches:

- Direct point-level comparison of clay layer presence between the calibration results and the borehole information. This comes down to counting the number of boreholes that was incorrectly modeled with respect to the presence of clay in both calibration results. We call this score N ;
- Calculation of a plausibility score by cell-by-cell summation of the probability of encountering the modeled statistical population at that cell. The probabilities were obtained from the probability field shown in Fig. 4b. In mathematical notation:

$$PR = \frac{N - \sum_{i=1}^{N} p(I_i)}{N} \qquad (1)$$

in which *PR* stands for what we call here the probability residual, which we define as the difference beween the probability of a perfect model of a completely known reality (which is 1), and the probability of the actual model. Furthermore, *N* is the dimension of the indicator array (in this case 220 x 220 = 48400), I_i represents the indicator (in this case either clay or "no clay") at location *i*, and $p(I_i)$ the probability of encountering that indicator at location *i*.

The idea of using *PR* next to N^- is that it gives some indication on the general improvement of clay layer's position, which might not always be revealed by point-level comparison due to the highly discontinuous nature of the clayer and the amount of scatter produced by the indicator simulator SISIM.

Table 2. Plausibility scores for the prior realization of the clay layer and the posterior realization resulting from the multimodal calibration run.

Score	Prior	Posterior	Improvement
N^-	107	96	10 %
PR	0.242	0.218	10 %

Per definition, the conventional approach yields no improvement on both scores, as the clay layer's position is fixed. The prior and posterior scores for the multimodal approach are given in Table 2, together with the relative improvement due to calibration.

Both plausibility scores show, by coincidence, an improvement of 10 % by calibration with the multimodal approach.

5.7. Conclusions and Discussion

We showed that the multimodal calibration method presented by *Janssen et al.* [2006] is applicable to a real world case. Moreover, the calibration of the multimodal, spatially correlated parameter field was successfully combined with the calibration of additional parameter fields (other than the multimodal one). This ability of Bayesian co-calibration

of a spatially correlated non-Gaussian parameter field (as is the multimodal parameter field of this study) with other spatially correlated parameter fields has, to our knowledge, not been reported elsewhere in the hydrological literature.

As not only the intra-population distributions are uncertain, but the positions of the statistical populations of a multimodal field are uncertain as well, the multimodal calibration method constitutes a more fair approach to deal with the model's inherent parameter uncertainty. The calculations show that not incorporating the uncertainty of the clay layer's position in the calibration (called the conventional approach in the current Chapter) can lead to biases is the calibrated parameter values. The bias can be so strong that parameter values become unrealistic for the statistical population they belong to. The conventional approach can also lead to different and even opposite conclusions about the conductive and protective capacities of the clay layer compared to a calibration run in which the clay layer is allowed to change shape.

If we compare the results obtained using the multimodal calibration method with those of the conventional approach, we can conclude that co-calibrating the position of the clay layer, as enabled by the approach advocated in this Chapter, is an improvement on several aspects. In the synthetic calibration runs, the prior shape of the parameter distributions were relatively unaffected, the co-calibrated parameter fields stayed closer to their prior means, and lower objective function values were achieved when using the multimodal method. Furthermore, also in the real-world case a lower objective function value was achieved, most parameter fields stayed closer to their prior means, and, on top of that, the number of incorrectly modeled boreholes decreased by 10%, and the probability of the indicator field improved as well. If these improvements are considered together with the fact that the inverse problem is better formulated by including more of the relevant uncertainty, the multimodal calibration approach renders a more reliable posterior model than the conventional approach.

The multimodal approach presents the calibration algorithm with an additional degree of freedom compared to the conventional one, and therefore with an extra possibility to explain residuals that are in fact caused by model errors. This is not different from adding an uncertain parameter to any other calibration effort, but the effects of model error masking on model predictions might be stronger if the masking manifests itself through unjustified lithology changes. For example, adjustment of the prior model by

enlarging the extent of the clay layer in a certain region of the model domain, in order to reduce residuals that are in fact caused by model errors, can result in a large overestimation of the travel times of contaminants towards nearby groundwater abstractions below the clay layer. One way to cope with this risk of masking model errors would be to explicitly account for model error in the calibration algorithm (the representer-based algorithm is equipped for this, see for example *Valstar et al.*, [2004]). Another way would be to make use of complementary data types, providing "second opinions" on lithology change as a means for better observation reproduction. Travel time / groundwater age determinations and concentration measurements come to mind as data types that have particularly high potential with this respect. The theoretical framework for implementing groundwater age or travel time information in the representer-based inverse algorithm was presented by *Janssen et al.* [2008]. For concentration data, this was done in *Valstar* [2001] and *Valstar et al*. [2004].

Appendix

This Appendix presents the prior fields and the calibration results of the co-calibrated parameters: the transmissivities of model layer 1 (Fig. A1), the transmissivities of model layer 3 (Fig. A2), and the river conductances (Fig. A3 and Table A1).

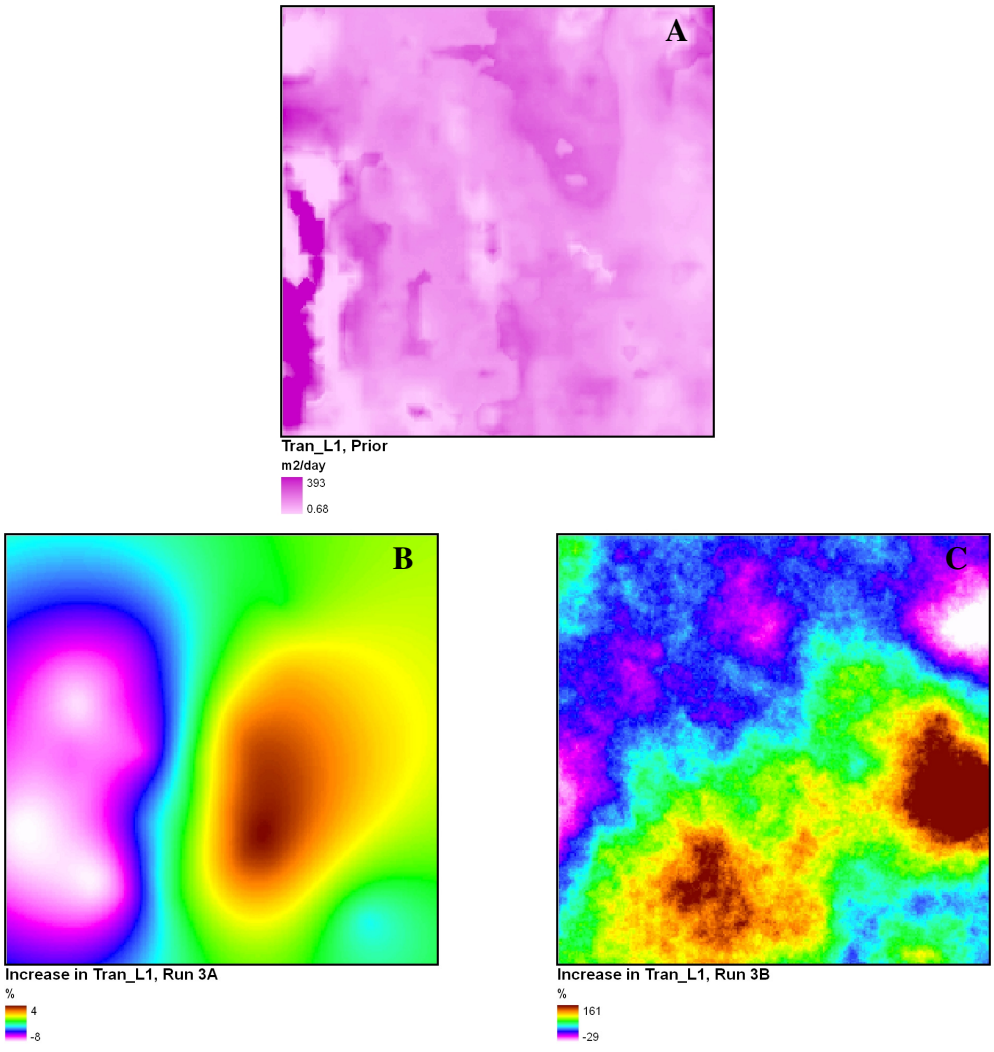

Figure A1. (A) Prior field of the transmissivities of model layer 1, (B) adjustment of this prior field during calibration run 3A (in % of the prior values), (C) adjustment of this prior field during calibration run 3B (in % of the prior values).

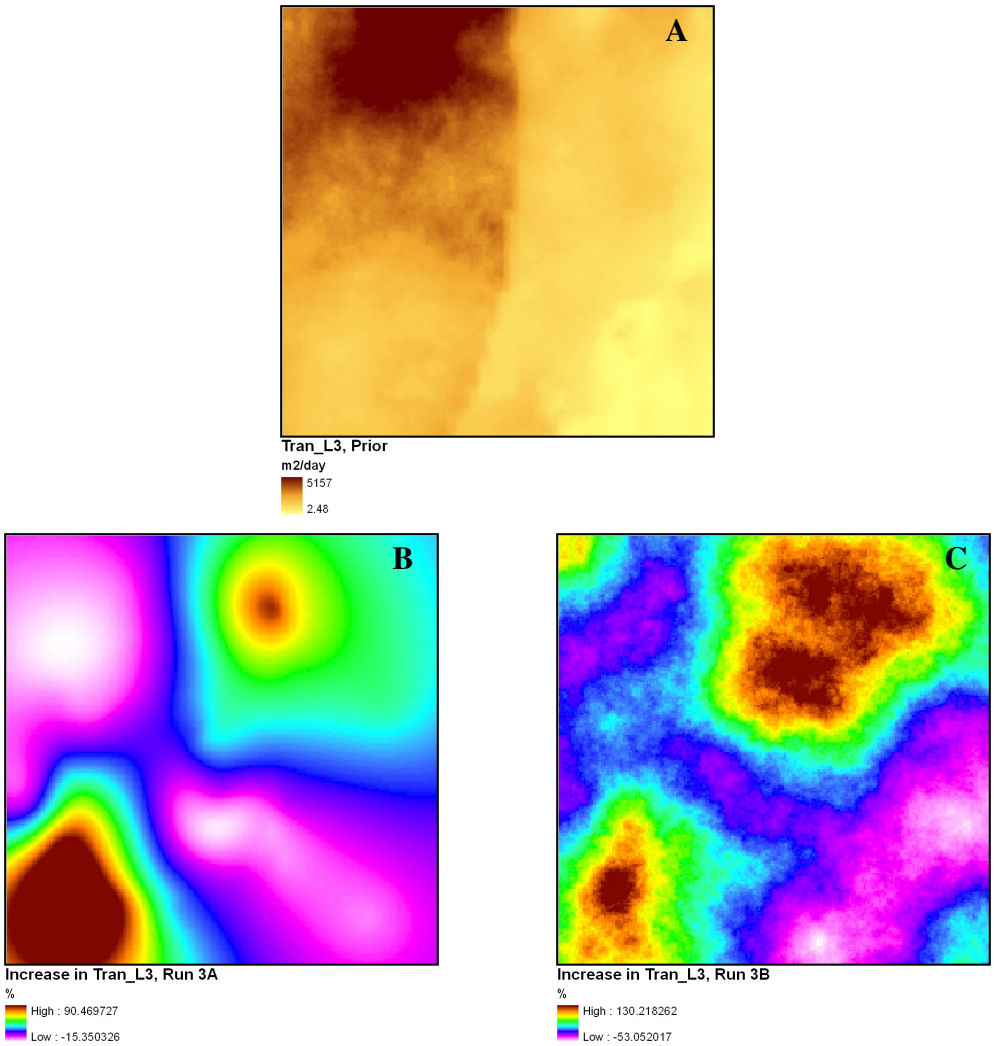

Figure A2. (A) Prior field of the transmissivities of model layer 3, (B) adjustment of this prior field during calibration run 3A (in % of the prior values), (C) adjustment of this prior field during calibration run 3B (in % of the prior values).

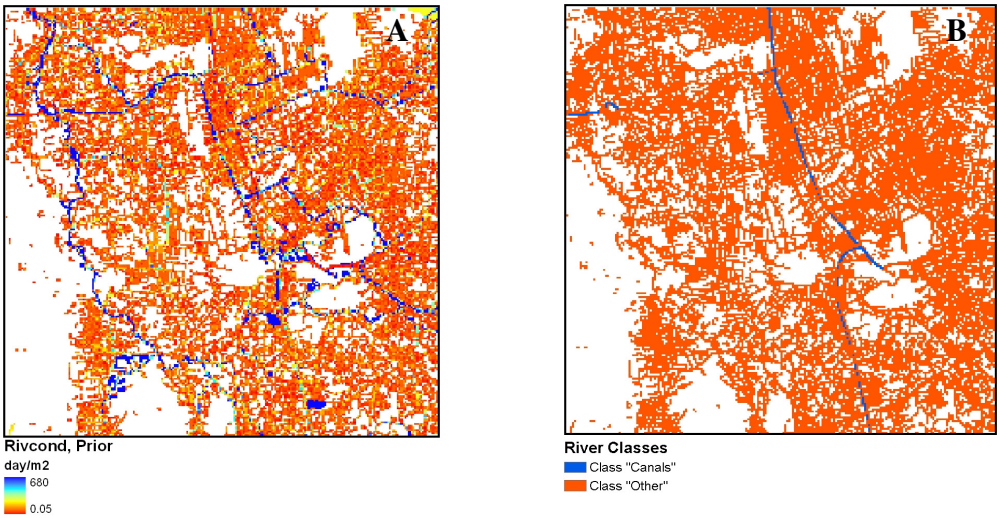

Figure A3. (A) Prior field of the river conductances, (B) subdivision of the streams in classes "Canals" and "Other" (as applied by *Snepvangers and Minnema* [2004]) both having their own statistical properties (see Table 1).

Table A1. Adjustments, with respect to the prior field, applied to the river conductances during calibration runs 3A and 3B.

	Adjustment	
Run	*"Canals"*	*"Other"*
3A (Multimodal)	479 %	360 %
3B (Conventional)	360 %	310 %

References

Deutsch, C. V., and A. G. Journel (1992), *Geostatistical Software Library and User's Guide, Appl. Geostat. Ser.*. Oxford University Press. Oxford.

Hoogendoorn, J. H., and C. B. M. te Stroet (1994), Optimalisatie Waterbeheer Wierden/Wierdense Veld. *TNO report OS 94-14 B (in Dutch)*.

Janssen, G. M. C. M., J. R. Valstar, and S. E. A. T. M. van der Zee (2006), Inverse modeling of multimodal conductivity distributions. *Wat. Resour. Res.* 42, W03410, doi:10.1029/2005WR004356.

Janssen, G. M. C. M., J. R. Valstar, and S. E. A. T. M. van der Zee (2008) Measurement network design including travel time determinations to minimize model prediction uncertainty. *Wat. Resour. Res.* 44, W02405, doi:10.1029/2006WR00546.

Leake, S. A., and D. V. Claar, (1999), Procedures and computer programs for telescopic mesh refinement using MODFLOW. *U.S. Geol. Surv. Open-File Rep 99-238*.

McDonald, M. G., and A. W. Harbaugh, (1988), A modular three-dimensional finite-difference ground-water flow model. *U.S. Geol. Surv. Open-File Rep. 97-571.*

Schweppe, F.C. (1973), *Uncertain Dynamic Systems*, Prentice Hall, Old Tappan, N. J.

Snepvangers, J. J. J. M., and B. Minnema, (2004), Waterschap Regge en Dinkel grondwatermodel en IR database ter ondersteuning van waterbeheer in Twente. *TNO report NITG 04-020-B (in Dutch)*.

Snepvangers, J. J. J. M. and W. Berendrecht (2007), Methodiekontwikkeling interactieve planvorming ten behoeve van het waterbeheer (MIPWA). *TNO report NITG 06-020-B (in Dutch)*.

Te Stroet, C. B. M. (1995), Calibration of Stochastic groundwater flow models. PhD Thesis. Delft University of Technology. Delft.

Valstar, J. R., D. B. McLaughlin, C. B. M. te Stroet, and F. C. van Geer (2004), A representer-based inverse method for groundwater flow and transport applications. *Wat. Resour. Res*. 40, W05116, doi:10.1029/2003WR002922

Valstar, J. R. (2001), Inverse modeling of groundwater flow and transport. PhD Thesis. Delft University of Technology. Delft.

Van Leeuwen, M., A. P. Butler, C. B. M. te Stroet, and J. A. Tompkins, (1999) Stochastic determination of the Wierden (Netherlands) capture zones. *Ground Water* 37(1), 8-17.

Webster, R., and M. Oliver (2001), *Geostatistics for environmental scientists*, John Wiley and Sons, Chichester, UK.

CHAPTER

6

Implications

The general objective of the present thesis was to increase our capabilities to fully, fairly and efficiently account for heterogeneity in groundwater models, and to effectively manage the uncertainty that inevitably results from this heterogeneity. This chapter discusses to what extent this objective has been reached, what the proposed methods and obtained results (can) mean for the current practice of groundwater modeling, and what improvements are still necessary and/or possible. This chapter does so separately for each main chapter of the thesis (Chapters 2-5).

Chapter 2

Chapter 2 presented theory and methodology to account for the effect of heterogeneity on local-scale dispersion and mixing in the context of nonlinear bioreactive transport. Chapter 2 clearly established that for nonlinear bioreactive transport, asymptotic behavior reveals a special regime in the sense that it is neither Fickian nor does it lead to the formation of traveling waves. Fickian and traveling wave behavior were shown to be extreme regimes. An either Fickian or traveling wave-like asymptotic regime would greatly simplify the upscaling of nonlinear reactive transport to typical grid sizes employed in real-world groundwater models. Fickian asymptotic behavior would imply that upscaling could be achieved by applying the regular convection-dispersion equation with an adapted, effective dispersion coefficient. Traveling wave behavior, on the other hand, would actually justify the commonly applied upscaling of nonlinear bioreactive transport in many commercial and scientific codes: applying the regular convection-dispersion equation with nonlinear reaction terms. The fact that, for the chosen, realistic parameters values used in Chapter 2, traveling wave behavior does not occur, means that the upscaling inherently performed in these codes probably does not reflect the correct large-scale behavior of the reaction and transport process, and may induce errors in the model results.

The results of Chapter 2 (especially Figures 5 and 6) have shown that, although the asymptotic transport behavior never really reached either Fickian or traveling wave

behavior for the chosen parameter values, at least these regimes are increasingly approximated with increasing distance (especially Fickian for high Peclet values, and traveling wave for low Peclet values). For certain combinations of Peclet values and bioreaction parameters, other than the ones applied in Chapter 2, the mentioned regimes might be approximated quicker. With the ever-increasing availability of computer power, however, the level of model grid discretization will tend to increase, meaning that grid cells become smaller. In that case, the combinations of bioreaction parameters and Peclet numbers, with which either a Fickian or a Traveling Wave regime can be assumed to be reached within grid cell dimensions, will probably become more extreme and unrealistic.

To efficiently test the behavior of the nonlinear bioreactive transport process with other parameter sets (for example, to test the assumption put forward in the previous paragraph, or to gain insight in the performance of bioremediation strategies in heterogeneous environments, along the lines of *Keijzer* [2001]), the availability of (semi-) analytical tools is crucial. Chapter 2 established the advective-dispersive stream tube approach in combination with the traveling wave approach as an accurate semi-analytical model that can be used for this purpose.

Although Chapter 2 has demonstrated that the current practice of upscaling nonlinear bioreactive transport probably does not reflect the actual reactive transport regime occurring at typical grid cell scales well, the question how to perform the upscaling instead was out of the scope of this study. The fact that the bioreactive transport process does not reach well-defined regimes at the scale of typically sized model grid cells, makes that the upscaling problem for nonlinear bioreactive transport is a current research frontier and thus needs further attention. In the meantime, the current practice is likely to continue to be the norm. In research aimed at cracking the upscaling problem, the stochastic-analytical developments presented in Chapter 2 can be very valuable.

Chapter 3

Chapter 3 presented a means to increase our capabilities with respect to subsurface characterization by proposing a method for including travel time information (groundwater age, tracer arrival times, etc.) into observation network design. The used

representer-based inverse method is very effective for measurement network design, as by directly and efficiently calculating linearized covariances between parameters and states, the calculation of the posterior parameter covariance matrix for every proposed measurement network, as well as time-consuming Monte Carlo analyses, are avoided. In Chapter 3, the representer method was extended to allow integration of this new data type, and thus a method for measurement network design including this data type was obtained. This new method now allows us to optimally profit from the potentially very high informative value of a new data collection effort that includes sampling for travel time determinations.

In Chapter 3, the tracers were assumed to undergo strictly advective transport. This is a rather limiting (probably the most limiting) assumption. Dispersion will, in natural systems, always play a role, increasing with distance and the amount of heterogeneity encountered along the way (see also Chapter 2). Therefore, dispersion adds much uncertainty to the travel times derived from tracer concentrations. In Chapter 3, dispersion was accounted for indirectly by recognizing the added uncertainty and applying large error variances to the travel time determinations. For the purpose of Chapter 3, which was mainly method development and demonstration, there was no need for obtaining actual estimates for the uncertainty, not in the least because the study was synthetic. For implementation of the method in a real-world case, however, the issue of incorporating the effect of dispersion into the uncertainty estimates should be tackled first.

A number of approaches can potentially assist in this, which include Monte Carlo analysis using direct simulation of groundwater age (age-mass approach, *Goode* [2000]) on a large number of equiprobable model realizations calibrated on tracer concentrations, or comparison of ages determined using different tracers (as different tracers are affected differently by dispersion (e.g. *Ekwurzel et al.* [1994]). None of these approaches have been applied in the literature with the specific aim of arriving at quantified age uncertainty estimates for individual determinations. It therefore deserves recommendation to further explore them in future research efforts, and to give more attention to this research aspect in general.

Chapter 4

Chapter 4 extended the applicability of inverse modeling to multimodal spatial parameter distributions. The most important implication of this new capability is that now, during the calibration process, the spatial distribution of different statistical populations existing in a parameter field can be treated stochastically as well. This is an important improvement of the treatment of the existing heterogeneity in the field: the spatial distribution of these statistical populations will have a larger influence on state measurements than the parameter distributions within these populations, at least if the probability distributions of the statistical populations are largely non-overlapping.

At the same time this means that if a parameter field is considered important enough to be calibrated during the inverse process (read: the state observations show enough sensitivity to the parameter field), and the parameter field consists of contrasting statistical populations, then treating the positions of the statistical populations deterministically is technically wrong and renders the calibration result questionable. The proposed multimodal calibration method is the first to offer a solution to this problem.

The question has often been asked to what extent the method would be applicable to highly contrasting media. Here the example of karstic aquifers comes to mind. In response to this, it is important to keep in mind that the method in principle targets situations in which intra-lithology parameter distributions actually influence state predictions. In case of highly contrasting media, this will often not be the case. In that case there is, in principle, no need to treat the parameter distribution as a multimodal continuum, and perhaps other calibration methods, aimed at the inversion of discrete lithology fields, are available to the modeler too (e.g. the Gradual Deformation Method and the Probability Perturbation Method, see the introduction of Chapter 4). Nevertheless, the question of the method's limitations in the context of highly contrasting media is interesting, not in the least because it is unclear how the methods for the calibration of discrete lithology fields perform in real-world hydrological settings. Substantiation of good performance of the concerned methods in real-world cases is very scarce in both hydrological- and petroleum engineering (the field from which these methods generally originate) literature.

For the performance of the proposed multimodal calibration method for highly-contrasting media, everything depends on the performance of the inverse algorithm

used for the calibration of the transformed field; the more contrasting the different statistical populations, the more severe the discontinuities in the derivative of the transformed parameter to the multimodally distributed parameter. In Chapter 4, the contrast between the two lithologies was considerable: still the representer-based inverse algorithm managed to find solutions. However, even though modifications to the line search could further increase the power of the representer algorithm with respect to the large discontinuities, surely at some point a limit is expected to be reached at which the representer method does not perform satisfactorily anymore.

Then again, any suitable inverse algorithm can be used for the calibration of the transformed field. Other inverse algorithms might be better in dealing with the heavy discontinuities then the representer-based inverse method. Particularly, inverse algorithms that do not calculate the abovementioned derivative could turn out powerful in this respect.

Definitely the most important drawback of the proposed multimodal calibration method is its computational demand. The method places inverse algorithms, usually quite computationally expensive themselves, in an iterative loop. Further research should therefore be directed at accelerating the method.

With respect to the applicability of the method outside geohydrology, it can be mentioned that the method could be useful in any situation in which multimodal spatially correlated parameter distributions have to be calibrated. An obvious example is petroleum engineering, as it has already been mentioned above that practically all research targeted at the inversion of lithology fields originates from this field of research.

Chapter 5

In Chapter 5, the multimodal calibration method was tested in a real-world case. Pronounced differences were found between the calibration result obtained with the multimodal method, and the result of a calibration effort in which the position of the clay layer was treated deterministically. Although in the end, of course, a modeler should not so much be interested in a single calibrated realization but in a sufficiently large ensemble of realizations to be able to deduce uncertainties of the model output, it is unlikely that both methods would result in a similar ensemble, as the biases observed in

the calibration result of the conventional approach were very likely to be due to the "model error" induced by the deterministic treatment of the position of the clay layer.

Both calibration approaches would therefore result in very different states predictions and uncertainty estimates. Considering the real-world case of Chapter 5, both approaches would yield very different conclusions about the shape and extent of a well protection zone to be installed to safeguard continuity of the groundwater production in the modeled area.

The calibration of the real-world case performed in Chapter 5 would greatly benefit from a more realistic simulator for generating clay layer realizations. The SISIM simulator used here produced unrealistic scatter in the indicator field: the discontuity of the clay layer was very likely overestimated, as the produced level of discontuity cannot be explained by geological formation processes. A genetic modeling approach, as suggested by *deMarsily et al.* [2005], would be highly recommendable. Unfortunately, for the clay formation treated in Chapter 5, such a model is currently not available.

It is stressed here that the calibration exercises performed in Chapter 5 were only performed on head observations, which are generally relatively insensitive to conductances compared to other data types such as travel times and concentrations. Although observed differences between the results of the multimodal and conventional calibration approach in the real-world case already were more pronounced than we initially anticipated, much more can be expected from other types of observations. For example, a well-designed grid of reliable travel time or groundwater age observations in the production aquifer would be of great value, as they would be highly sensitive to the position and conductance of the clay layer. The theoretical framework for implementing groundwater age or travel time information in the representer-based inverse algorithm was presented in Chapter 3.

References

De Marsily, Gh., F. Delay, J. Gonçalvès, Ph. Renard, V. Teles, S. Violette (2005), Dealing with spatial heterogeneity, *Hydrogeology Journal*, *13*, 161-183.

Ekwurzel, B., P. Schlosser, W. M. Smethie Jr, L. N. Plummer, E. Busenberg, R. L. Michel, R. Weppernig, and M. Stute (1994), Dating of shallow groundwater: comparison of the transient tracers 3H/3He, chlorofluorocarbons, and 85Kr, *Wat. Resour. Res.*, 30, 1693-1708.

Keijzer, H., (2001), Transport of nonlinearly biodegradable contaminants in aquifers, Ph.D. Thesis Wageningen University, Wageningen.

Goode, D. J., (1996), Direct simulation of groundwater age, *Wat. Resour. Res.*, 32, 289-296.

SUMMARY

Summary

Few groundwater systems have escaped the consequences of the ever-expanding human influence on the natural environment. Globally, groundwater systems are heavily stressed, the most important reasons being overexploitation, contamination, and straitjacketing.

For tackling these issues, knowledge of the groundwater system and how it responds to new influences is crucial. Groundwater models are popular and essential tools to formalize and administrate the existing knowledge of groundwater systems and utilize this knowledge to produce areally distributed state descriptions and predictions based on the best available information. It is clear that the more sound the description of processes and system properties, the more accurate the model outcome. Unfortunately, "knowing" the system, and therefore describing and modeling it, is greatly complicated by spatiotemporal heterogeneity. Methods are needed to allow modelers to accurately, fairly and efficiently account for all relevant heterogeneity, and to manage it effectively.

The main chapters of the thesis, though quite diverse, all share one common, ultimate purpose: improved modeling of flow and transport processes in heterogeneous subsurface environments. Specifically, the current thesis offers contributions to a better incorporation of heterogeneity in physically-based, fully distributed numerical groundwater models. It does so in both forward and inverse frameworks. In the thesis a number of major issues with respect to handling heterogeneity and uncertainty in different situations are tackled, and thus the ability to correctly, fairly and/or effectively deal with and manage heterogeneity is extended to these particular situations.

Chapter 2 contributes to the upscaling of bioreactive transport in heterogeneous environments. It does so by investigating the interplay between heterogeneity in the hydraulic properties of the medium, local-scale dispersion and nonlinear biodegradation of a sorbing contaminant moving through the medium, in a synthetic small-scale system in which biodegradation is stimulated by injecting oxygen-rich groundwater. The ultimate purpose of this (type of) investigation is to study long-term asymptotic behavior of solute

fronts, in order to derive (the validity of) process descriptions for nonlinear bioreactive transport applicable to the larger scale.

In Chapter 2, the coupled effects of nonlinear biodegradation and heterogeneity are analyzed by combining recent advances in analytical one-dimensional modeling of bioreactive transport with stochastic concepts of dispersive mixing in heterogeneous domains. The transport process in the heterogeneous environment is modeled by applying the so-called stochastic-convective and the advective-dispersive stream tube approaches, in which a semi-analytical traveling wave solution for one-dimensional reactive transport is used. The results of numerical simulations validate the traveling wave solution as an efficient and accurate way to evaluate the development of intra-stream tube concentration distributions, as well as the advective-dispersive stream tube approach as a suitable approach to describe nonlinear bioreactive transport in systems controlled by local-scale dispersion. In contrast to conservative transport, the mean contaminant flux is shown to be significantly influenced by transverse dispersion, even for realistic Peclet values. Furthermore, asymptotic front shapes are shown to be neither Fickian nor constant (traveling wave behavior), which raises questions about the current practice of upscaling bioreactive transport. The error caused by neglecting local dispersion was found to increase with time and to remain significant even for large retardation differences between electron acceptor and contaminant. This implies that, even if reaction rates are dominated by chromatographic mixing, the dispersive mixing process cannot be disregarded when predicting bioreactive transport.

In Chapter 3, managing heterogeneity, in terms of reduction of model output uncertainties, is enhanced by extending inverse theory to determinations of travel time. Travel time determinations have found increasing application in the characterization of groundwater systems. No algorithms are available, however, to optimally design sampling strategies including this information type. Chapter 3 proposes a first-order methodology to include groundwater age or tracer arrival time determinations in measurement network design and applies the methodology in an illustrative example in which the network design is directed at contaminant breakthrough uncertainty minimization. Linearized (cross) covariances are calculated between potential measurements and the goal variables of which we want to reduce the uncertainty. These

goal variables are the groundwater age at the control plane and the breakthrough locations of the contaminant. The travel time is assumed to be lognormally distributed and therefore we logtransform the age determinations in compliance with the adopted Bayesian framework. Accordingly, expressions are derived for the linearized covariances between the transformed age determinations and the parameters and states. In a synthetic numerical example, the derived expressions are shown to provide good first-order predictions of the variance of the natural logarithm of groundwater age if the variance of the natural logarithm of the conductivity is less than 3. The calculated covariances can be used to predict, at first order, the posterior breakthrough variance belonging to a candidate network before samples are actually taken. A Genetic Algorithm is used to efficiently search, among all candidate networks, for a near-optimal one. It is shown that, in our numerical example, an age estimation network outperforms (in terms of breakthrough uncertainty reduction) equally sized head measurement networks and conductivity measurement networks, even if the age estimations are highly uncertain.

Chapter 4 extends the applicability of inverse methods to a challenging but ubiquitous type of parameter distributions: multimodal distributions. Multimodal distributions arise when within one parameter field multiple statistical populations exist, each having different means and/or variances of the parameter of concern.

Multimodal distributions cannot be handled well by existing inverse algorithms. Chapter 4 proposes a method that resolves the difficulties the multimodal distributions pose to the existing inverse algorithms, so that they can be used again. The method is applied to a synthetic model of a confining layer with a bi- and trimodal hydraulic conductivity distribution.

The basis of the technique is the transformation of the original multimodal conductivity distribution to the standard normal distribution, thus fulfilling the condition of normality that is required by the used inverse algorithm (in this case the representer method). Using this transformation, a calibration that starts from a homogeneous prior field is shown to radically improve the estimation of the protective properties of the confining layer compared to a unimodal approach of the calibration. The method is also used for the calibration of multimodal heterogeneous prior fields. The inevitable distortion of the

original parameter ranges in the posterior fields that results from the transformation process, is absorbed by an iterative post-conditioning procedure, in which lithology information obtained from the distorted calibrated fields is used to condition the generation of a new multimodal field that complies again with the original geostatistics. After transformation, this new field can be calibrated again, and this process is repeated until the newly generated field agrees with the measurement information sufficiently well. Then, the lithology distribution of this new field is fixed and the intra-lithology conductivity distributions are calibrated. This approach is shown to preserve the original geostatistics, both of the lithology field and the intra-lithology hydraulic conductivity distributions.

Chapter 5 applies the method developed in Chapter 4 to a real-world case. The multimodality in the parameter field is now caused by the presence of a highly heterogeneous and discontinuous clay layer, which is modeled through the vertical conductance between the second and the third model layer. At locations where this clay layer is present, the vertical conductance is on average much smaller than at the locations where it is absent. As the proposed method allows for the calibration of the continuous parameter field, and vertical conductance is the quotient of conductivity (assumed constant) over layer thickness, simultaneously the presence of the clay layer and its thickness are calibrated.
In Chapter 5, not only the multimodally distributed parameters, but also other parameter fields are calibrated. This ability of co-calibrating a spatially correlated non-Gaussian parameter field (as is the multimodal parameter field of this study) with other spatially correlated parameter fields has, to our knowledge, not been reported elsewhere in the hydrological literature. Furthermore, some improvements to the method as presented in Chapter 4 are proposed, to stimulate algorithm convergence.
Besides method demonstration, emphasis is given to the performance of the proposed multimodal calibration method when compared to a “conventional” approach in which the different statistical populations are not allowed to change position (read: the position of the clay layer is not allowed to change). Pronounced differences are found in the calibration result. The conventional calibration seems to suffer severely from the restriction imposed by the predefined position of the clay layer, causing projection of

necessary changes to this position on the parameters that *are* calibrated. Several performance criteria are investigated to quantify the differences in calibration result between the two approaches. Scores on these criteria all favor the result of the multimodal method as the more likely solution of the inverse problem.

SAMENVATTING

Samenvatting

Maar weinig grondwatersystem ontsnappen aan de gevolgen van de immer uitbreidende menselijke invloed op de natuurlijke omgeving. Wereldwijd staan grondwatersystemen onder druk door met name uitputting, verontreiniging en beheersing.
Om deze problemen het hoofd te kunnen bieden is kennis van het grondwatersysteem en van hoe dit systeem reageert op nieuwe invloeden cruciaal. In veel grondwaterstudies worden mathematische modellen gebruikt om de bestaande kennis te formaliseren en te bundelen, en om met de beste beschikbare informatie uitspraken te kunnen doen over de toestand van het systeem, ruimtelijk gedistribueerd, nu en in de toekomst. Hoe beter de proces- en systeembeschrijvingen, hoe accurater de modeluitkomsten (i.e.: meer in overeenstemming met de werkelijkheid). Het “kennen” van het systeem wordt echter sterk bemoeilijkt door ruimtelijke en temporele heterogeniteit. Er is een behoefte aan methoden die de grondwatermodelleur helpen om alle relevante heterogeniteit in het systeem op een accurate, eerlijke en efficiënte manier in de gebruikte modellen te verwerken en vervolgens op een effectieve manier te beheersen.
De inhoudelijke hoofdstukken van dit proefschrift zijn vrij divers, maar hebben één gemeenschappelijk doel: verbeterde stromings- en transportmodellering door verbetering van de verwerking van de heterogeniteit in de ondergrond in volledig gedistribueerde, numerieke grondwatermodellen. Aandacht wordt hierbij gegeven aan zowel het voorwaartse als het inverse geval.
In het proefschrift worden belangrijke problemen behandeld met betrekking tot het omgaan met heterogeniteit en onzekerheid in verschillende situaties en wordt op deze manier de mogelijkheid correct, eerlijk en/of effectief om te gaan met heterogeniteit en deze te beheersen, uitgebreid naar deze specifieke situaties.

Hoofdstuk 2 levert een bijdrage aan het opschalen van bioreactief transport in een heterogene ondergrond. Het hoofdstuk doet dit door het samenspel te bestuderen tussen heterogeniteit in de doorlatende eigenschappen van het medium, de lokale dispersie die door deze heterogeneit versterkt wordt, en niet-lineaire biodegradatie van

een sorberende verontreiniging, welke door een kleinschalig, synthetisch systeem beweegt waarin biodegradatie wordt gestimuleerd door de injectie van zuurstofrijk grondwater. Het uiteindelijke doel van dit (type) onderzoek is het bestuderen van het lange-termijngedrag van het transportproces, om zo (de geldigheid van) procesbeschrijvingen voor niet-lineair bioreactief transport op een hoger schaalniveau (lees: gridcellen van een toegepast grondwatermodel) af te leiden.

In Hoofdstuk 2 worden de gekoppelde effecten van niet-lineaire biodegradatie en heterogeniteit geanalyseerd door recente ontwikkelingen in analytische 1D-modellering van bioreactief transport te combineren met stochastische concepten van dispersieve menging in heterogene media. Het transportproces in de heterogene omgeving wordt gemodelleerd door toepassing van de zogenaamde stochastisch-convectieve en advectief-dispersieve stroombaanbenaderingen, waarbij een semi-analytische “lopende-golf” oplossing wordt gebruikt voor het 1D reactief transport. Numerieke simulaties valideren de lopende-golf oplossing als een efficiënte en accurate manier om de ontwikkeling van de concentratieverdeling binnen een stroombaan te berekenen, en de advectieve-dispersieve stroombaanbenadering als een bruikbare aanpak om niet-lineair bioreactief transport te beschrijven in systemen waarin lokale dispersie een belangrijke rol speelt.

De gemiddelde massaflux van de verontreining blijkt, in tegenstelling tot het conservatieve geval, significant beïnvloed te worden door lokale dispersie, zelfs voor realistische Pecletwaarden. Verder wordt aangetoond dat de asympotische frontvormen noch “Fickian”, noch constant (lopende-golf gedrag) zijn. Dit roept vragen op over de huidige praktijk van het opschalen van niet-lineair bioreactief transport. De fout die veroorzaakt wordt indien lokale dispersie wordt genegeerd neemt toe met de tijd en blijft zelfs significant bij grote verschillen in de mate van retardatie tussen de electronenacceptor en de verontreiniging. Dit impliceert dat, zelfs als de reactiesnelheden gedomineerd worden door chromatografisch mixen, het proces van dispersieve menging niet kan worden verwaarloosd voor het geval van niet-lineair bioreactief transport.

In Hoofdstuk 3 worden de mogelijkheden voor het beheersen van de heterogeniteit in de ondergrond vergroot door het uitbreiden van inverse theorie naar bepalingen van de

ouderdom van het grondwater en reistijden. Deze bepalingen worden meer en meer toegepast bij het karakteriseren van grondwatersystemen. Er zijn echter nog geen methoden beschikbaar die het ontwerp van meetnetten voor dit datatype kunnen optimaliseren. Hoofdstuk 3 stelt daarom een eerste-orde methode voor om ouderdoms- en reistijdenbepalingen mee te kunnen nemen in het ontwerp van meetnetten, en past de methode toe in een illustratief, synthetisch voorbeeld waarin het meetnetontwerp is gericht op het minimaliseren van de onzekerheid in doorbraaktijd van een conservatieve verontreiniging.

De methode berekent gelineariseerde covarianties tussen de potentiële metingen en de doelvariabelen waarvan we de onzekerheid willen minimaliseren. Deze doelvariabelen zijn de ouderdom van het grondwater in het doorbraakvlak en de doorbraaklocaties van de verontreiniging. Er wordt aangenomen dat de reistijden/ouderdommen lognormaal verdeeld zijn en daarom worden de reistijdmetingen getransformeerd naar hun natuurlijke logaritmen zodat voldaan wordt aan het Bayesiaanse raamwerk van deze studie. In het verlengde hiervan worden uitdrukkingen afgeleid voor de gelineariseerde covarianties tussen de getransformeerde leeftijdsbepalingen en de parameters en toestandsvariabelen. In een synthetisch, numeriek voorbeeld, blijken de afgeleide uitdrukkingen goede eerste-orde voorspellingen te geven van de variantie van de natuurlijke logaritme van de grondwaterleeftijd als de variantie van de natuurlijke logaritme van de doorlatendheid kleiner is dan 3. De berekende covarianties kunnen gebruikt worden om, in eerste orde, de a posteriori doorbraaktijdvariantie te berekenen van een meetnetwerk voordat de metingen daadwerkelijk genomen worden. Een Genetisch Algoritme wordt gebruikt om, op een effectieve manier, tussen alle mogelijke meetnetten, te zoeken naar de meetnetconfiguratie die optimaal of vrijwel optimaal presteert.

Er wordt aangetoond dat, in het numerieke voorbeeld van dit hoofdstuk, een netwerk bestaande uit leeftijdsmetingen beter presteert (wat betreft de afname van de onzekerheid in doorbraaktijd) dan stijghoogtemeetnetten en doorlatendheidsmeetnetten van gelijke grootte (aantal metingen), zelfs als de leeftijdsmetingen zelf zeer onzeker zijn.

Hoofdstuk 4 breidt de kunst van het inverse modelleren uit naar een lastig, maar veelvuldig voorkomend type parameterverdelingen: multimodale verdelingen. Multimodale verdelingen ontstaan wanneer binnen één parameterveld meerdere statistische populaties bestaan, elke met een ander gemiddelde en/of variantie van de betreffende parameter.
Bestaande inverse algoritmen kunnen niet goed overweg met deze multimodale, ruimtelijk gecorreleerde parameterverdelingen. Hoofdstuk 4 presenteert een methode die de problemen wegneemt, die bestaande inverse algoritmen met dit type verdelingen hebben, zodat deze weer gebruikt kunnen worden. De methode wordt toegepast op een synthetisch model van een deklaag met een bi- en trimodale hydraulische doorlatendheidsverdeling.
De basis van de voorgestelde techniek wordt gevormd door een transformatie van de originele multimodale verdeling naar de standaard normale verdeling, waarmee voldaan wordt aan de voorwaarde van normaliteit die gesteld wordt door het gebruikte inverse algoritme (in dit geval de representermethode). Met deze transformatie levert een calibratie startend met een homogeen initieel parameterveld een sterk verbeterde voorspelling op van de beschermende eigenschappen van de deklaag. De methode wordt ook ingezet voor de calibratie van heterogene initiële parametervelden (initiële parametervelden die aan de originele multimodale geostatistieken voldoen). De onvermijdelijke verstoring van de originele geostatistieken in de gecalibreerde velden, welke het gevolg is van de transformatie, wordt geabsorbeerd door een iteratieve post-conditioneringsprocedure, waarin de lithologische informatie afkomstig van de verstoorde gecalibreerde velden gebruikt wordt om een nieuw initieel veld te genereren dat weer voldoet aan de originele geostatistieken. Na transformatie kan dit veld weer gecalibreerd worden, en dit proces wordt herhaald totdat een nieuw gegenereerd initieel veld in voldoende mate voldoet aan de meetinformatie. Vervolgens wordt het lithologieveld vastgezet, en worden de parameterverdelingen daarbinnen gecalibreerd. Er wordt aangetoond dat deze aanpak de originele geostatistieken, zowel van het lithologieveld als van de parameterverdelingen daarbinnen, in stand houdt.

In Hoofdstuk 5 wordt de in Hoofdstuk 4 ontwikkelde methode toegepast op een grondwatermodel van een werkelijk gebied. De multimodaliteit in het parameterveld

wordt nu veroorzaakt door de aanwezigheid van een zeer heterogene en discontinue kleilaag, welke gemodelleerd wordt via de verticale conductance tussen de 2^{e} en 3^{e} modellaag: daar waar de kleilaag aanwezig is, is de verticale conductance gemiddeld veel kleiner dan waar de kleilaag afwezig is. Aangezien de voorgestelde methode de calibratie van het continue parameterveld mogelijk maakt, en de verticale conductance het quotiënt is van de (constant geachte) doorlatendheid en de laagdikte, worden de aanwezigheid en dikte van de kleilaag tegelijkertijd gecalibreerd.

In Hoofdstuk 5 worden niet alleen de multimodaal verdeelde parameters, maar tegelijkertijd ook andere velden gecalibreerd. Voor zover bekend is deze mogelijkheid tot co-calibratie van een ruimtelijk gecorreleerd niet-Gaussisch parameterveld (zoals het multimodale veld in deze studie) met andere ruimtelijk gecorreleerde parametervelden, niet eerder beschreven in de hydrologische literatuur. Verder worden ook enkele verbeteringen van de methode voorgesteld ten opzichte van Hoofdstuk 4, ter versnelling van de convergentie.

Naast demonstratie van de voorgestelde multimodale calibratiemethode wordt nadruk gelegd op de prestatie van de methode ten opzichte van een “conventionele” aanpak waarin de verschillende statistische populaties niet van positie kunnen veranderen, i.c. de positie van de kleilaag vastgelegd wordt. Er worden uitgesproken verschillen gevonden in het calibratieresultaat. De conventionele calibratie lijkt te lijden onder de restricties die het gevolg zijn van het vastleggen van de positie van de kleilaag, waardoor noodzakelijke aanpassingen aan deze positie geprojecteerd worden op parameters die *wel* gecalibreerd worden. Verschillende prestatiecriteria worden onderzocht om de verschillen in het calibratieresultaat tussen de twee benaderingen te kwantificeren. De scores op deze criteria zijn alle beter voor het resultaat van de multimodale methode, waardoor dit resultaat waarschijnlijker lijkt.

DANKWOORD

Acknowledgements

Dankwoord

Dit proefschrift was nooit tot stand gekomen zonder de begeleiding, hulp en ondersteuning van een aantal mensen, dat ik hier graag wil bedanken.

Allereerst gaat mijn dank uit naar mijn promotor en mijn copromotor, respectievelijk Sjoerd van der Zee en Johan Valstar.
Johan, ik beschouw jou als degene die mij het vak van geohydroloog heeft bijgebracht. Mijn achtergrond in deze discipline was bij aanvang behoorlijk zwak te noemen en ik kan me niet voorstellen dat je in het begin geen twijfels hebt gehad of ik wel zo'n geschikte kandidaat was om het onderwerp van dit proefschrift op te pakken en daar ook binnen afzienbare tijd significante vooruitgang in te boeken. Ik hoop dat je tevreden bent over het eindresultaat. Ik wil je bedanken voor het grote vertrouwen dat je in mij gesteld hebt en ook voor de grote vrijheid die je me daaruit voortvloeiend hebt gegeven om de promotie in te vullen. Dat vond ik erg prettig werken. Ik heb onze inhoudelijke discussies altijd erg gewaardeerd en was altijd onder de indruk van je expertise. Het was heel geruststellend om iemand met zoveel vakkennis en inzicht als jij "achter de hand" te hebben. Ik heb erg veel van je geleerd en hoop in de toekomst nog veel met je samen te werken in onze nieuwe Groundwater Quality groep bij Deltares/TNO.

Sjoerd, jou moet ik natuurlijk allereerst bedanken voor de kans die je me hebt gegeven middels de aanstelling als AIO. Ook van jou ging een enorm vertrouwen uit, waardoor ik altijd fijn gewerkt heb. Omdat je wat expertise betreft wat verder van de inverse materie af stond dan Johan ben je bij dat gedeelte wat minder betrokken geweest, maar ik heb je aandacht voor de grote lijn en ook het commentaar op de stukken wel erg gewaardeerd. En we hebben prettig samengewerkt voor het eerste stuk, wat weer vooral in jouw straatje lag. Daarin kwamen we diverse grote problemen tegen, waar ik achteraf gezien erg veel van geleerd heb en waar we ons samen met Olaf Cirpka goed doorheen geslagen hebben.

This brings me to the next person I would like to express my gratitude to. Olaf, we called for your help at a moment we got completely stuck doing the calculations for Chapter 2. Having read many of your impressive papers, I knew you could be the one to get us going again. I was absolutely amazed by the enthusiasm and thoroughness with which you helped us. I remember that you usually replied e-mails within a day! And they were always extensive and complete, so I was never left with questions. You really saved Chapter 2 and made my first paper in WRR possible.

Een woord van dank is ook op zijn plaats voor richting Erwin Temminghoff. Erwin, hoewel je niet betrokken was bij dit onderzoek, ben jij toch degene die mij enthousiast gemaakt heeft voor onderzoek en wetenschap in het algemeen. Dat is natuurlijk gebeurd tijdens het afstudeervak dat ik bij jou gedaan heb. Je was toen zelfs de eerste die mij polste voor een AIO-plaats, al vond ik dat idee toen nog ronduit belachelijk. Kortom, Erwin, bedankt!
Gelieve me echter nooit meer *en plain publique* een Limburger te noemen (sorry Sjoerd).

Komen we nu bij de personen die vooral op het sociale vlak voor een geslaagde AIO-tijd hebben gezorgd. Erwin, Bert, Walter, Debbie, Franciska, Odair, Esther, Winnie, Thom, Ellis, Romulo, Gerwin, Anke, Thomas, Petra, Laura, Ram, Paul, Renske, Elena, Michaela, Ron, Jaap, Willem, Simon, Tamas: bedankt voor de discussies, voor de geboden hulp met van alles en nog wat, voor de illegale software, voor de goeie grappen, maar vooral voor de goede sfeer en de gezelligheid!

In het bijzonder wil ik me natuurlijk even tot Ellen richten, met wie ik vanaf het begin tot mijn vertrek naar TNO de kamer heb gedeeld. Ellen, zoals ik al eens eerder heb gezegd vond ik het buitengewoon plezierig om jou als kamergenoot te hebben. Bedankt voor alle goede gesprekken, over zin en onzin en lief en leed, en bedankt ook voor je grenzeloze behulpzaamheid en je attenties, bijvoorbeeld op de laatste dag van mijn laatste volledige werkweek op de vakgroep. Ik hoop dat we goede vrienden blijven.

Last but certainly not least, wil ik natuurlijk graag Monika bedanken. Monika, sorry dat ik het afgelopen jaar zoveel tijd die we veel beter samen hadden kunnen besteden nog in het proefschrift heb moeten stoppen, maar nu gaan we echt van het leven genieten. We hebben nu allebei een Ph.D. van Wageningen Universiteit, dus als we nu niet stinkend rijk worden, dan weet ik het niet meer.

Gijs

This research was partly funded by TNO

ABOUT THE AUTHOR

About the Author

Gijs Marinus Catharina Maria Janssen was born on September 1, 1977 in Veldhoven, The Netherlands. In 1995 he obtained a VWO- ("preparatory scientific education") diploma from the Anton van Duinkerkencollege in Veldhoven. In the summer of 1995 he moved to Wageningen to pursue an M.Sc. in the Environmental Sciences from Wageningen University. For his M.Sc. he specialized in Soil Quality and Soil Pollution, and wrote a thesis on in-situ zinc precipitation by means of biological sulfide reduction in an aquifer with highly unsuitable initial conditions for the necessary bacteria. This research was published in *Environmental Science and Technology* (Janssen and Temminghoff, 2004). For his training period, Gijs moved to Newark, Delaware to work at the Department of Civil and Environmental Engineering of the University of Delaware, where he was employed in the group of Prof. H.E. Allen from June to December 2001.
The M.Sc. degree was obtained in January 2002. Subsequently, Gijs decided to further develop his interests in subsurface processes in the discipline of geohydrological modeling. He was offered a Ph.D. position at the Department of Soil Quality of Wageningen University, where he worked on the current thesis from February 2002 to April 2006. In May 2006, Gijs accepted a position as Junior Researcher Geohydrology at the division of Soil and Groundwater Systems of TNO / Deltares. In this position, Gijs is mainly involved in regional modeling of groundwater quality. In addition, Gijs recently joined the board of the Netherlands Hydrological Society.

Netherlands Research School for the
Socio-Economic and Natural Sciences of the Environment

CERTIFICATE

The Netherlands Research School for the
Socio-Economic and Natural Sciences of the Environment
(SENSE), declares that

Gijs Marinus Catharina Maria Janssen

Born on: *1 September 1977* at: *Veldhoven, The Netherlands*

has successfully fulfilled all requirements of the
Educational Programme of SENSE.

Place: *Wageningen* Date: *19 November 2008*

the Chairman of the
SENSE board

Prof. dr. R. Leemans

the SENSE Director
of Education

Dr. A. van Dommelen

The SENSE Research School declares that Mr. Gijs Marinus Catharina Maria Janssen has successfully fulfilled all requirements of the Educational PhD Programme of SENSE with a work load of 36 ECTS, including the following activities:

SENSE PhD courses:

- **Environmental Research in Context**
- **Research Context Activity: Organizing Committee SENSE Symposium "Kyoto and Beyond" (De Reehorst, Ede - 23 June 2005)**
- **Uncertainty Analysis**

Other Phd courses:

- **Introduction to Numerical Modeling of Flow and Transport Problems**
- **Upscaling from Pore to Core**
- **Stochastic Modelling and Geostatistics for Flow and Transport in Porous Media**
- **Scientific Writing**

Research and Management Skills:

- **Self-study Programming in Fortran 90/95**

Oral Presentations:

- **SENSE Summer Symposium 17 June 2004, Utrecht, The Netherlands**
- **FEM_MODFLOW, 13 – 16 September 2004, Karlovy Vary, Czech Republic**
- **XVI International Conference on Computational Methods in Water Resources 19 – 22 June 2006, Copenhagen, Denmark**
- **IAHR International Groundwater Symposium, 18-20 June 2008, Istanbul, Turkey**

Mr. J. Feenstra
SENSE Coordinator PhD Education and Research